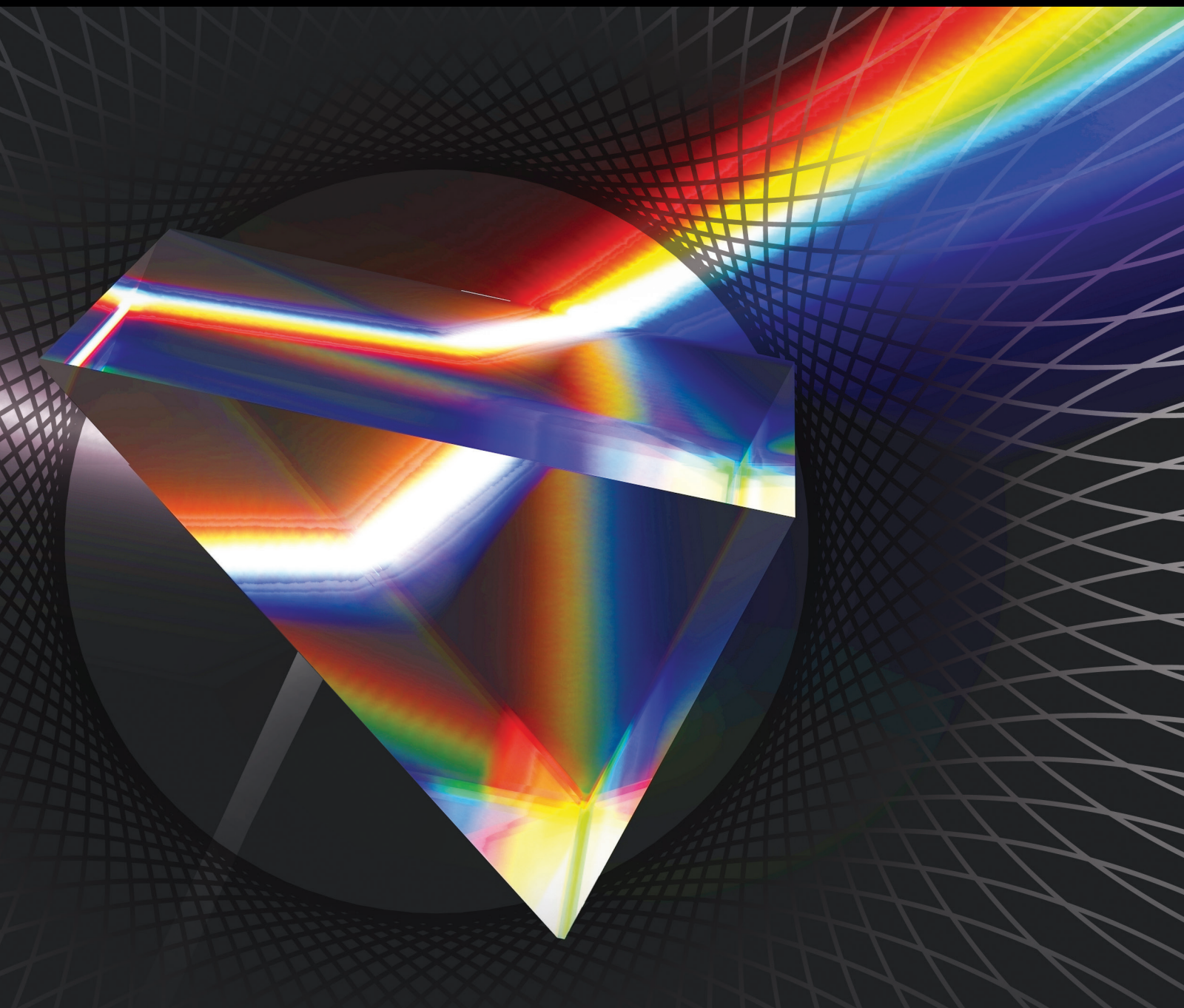


# Advances in Optical 3D Imaging Technology

Lead Guest Editor: Xiaowei Li

Guest Editors: Wei Liu and Seok-Tae Kim



# Advances in Optical 3D Imaging Technology



International Journal of Optics

---

## **Advances in Optical 3D Imaging Technology**

Lead Guest Editor: Xiaowei Li

Guest Editors: Wei Liu and Seok-Tae Kim



Copyright © 2018 Hindawi. All rights reserved.

This is a special issue published in "International Journal of Optics." All articles are open access articles distributed under the Creative Commons Attribution License, which permits unrestricted use, distribution, and reproduction in any medium, provided the original work is properly cited.

## **Editorial Board**

Fortunato Tito Arecchi, Italy  
Gaetano Assanto, Italy  
Augusto Beléndez, Spain  
E. Bernabeu, Spain  
Wojtek J. Bock, Canada  
Neil Broderick, New Zealand  
A. Cartaxo, Portugal  
Giulio Cerullo, Italy  
David Coutts, Australia  
Mahmoud Fallahi, USA  
Sulaiman W. Harun, Malaysia

Nicușor Iftimia, USA  
Wonho Jhe, Republic of Korea  
Mark A. Kahan, USA  
Wiesław Krolikowski, Australia  
Rainer Leitgeb, Austria  
Gong-Ru Lin, Taiwan  
Dragomir Neshev, Australia  
Takahige Omatsu, Japan  
Gang-Ding Peng, Australia  
Adrian Podoleanu, UK  
Chenggen Quan, Singapore

Giancarlo C. Righini, Italy  
Paramasivam Senthilkumaran, India  
John T. Sheridan, Ireland  
Mustapha Tlidi, Belgium  
Stefano Trillo, Italy  
Carmen Vazquez, Spain  
Stefan Wabnitz, Italy  
Leonid P. Yaroslavsky, Israel  
Qin Zhou, China

## Contents

### **Depth Analysis of Greyscale Integral Images Using Continuous Multiview Wavelet Transform**

Vladimir Saveljev  and Irina Palchikova

Research Article (8 pages), Article ID 3151209, Volume 2018 (2018)

### **Study on Quantitative Phase Imaging by Dual-Wavelength Digital Holography Microscopy**

Lin Hu, Yunxiu Shui, Yaohui Dai, Haiyu Wu, Gang Zhu, and Yan Yang 

Research Article (8 pages), Article ID 2312137, Volume 2018 (2018)

### **A Structured Light RGB-D Camera System for Accurate Depth Measurement**

Van Luan Tran  and Huei-Yung Lin

Research Article (7 pages), Article ID 8659847, Volume 2018 (2018)

### **Measuring the Phase of an Optical Field from Two Intensity Measurements: Analysis of a Simple Theoretical Model**

Damien P. Kelly 

Research Article (10 pages), Article ID 9560401, Volume 2018 (2018)

### **Multirotor UAV-Based Photogrammetric Mapping for Road Design**

Muhammad Akmal Zulkipli and Khairul Nizam Tahar 

Research Article (7 pages), Article ID 1871058, Volume 2018 (2018)

### **Two-Step Phase Retrieval Algorithm Using Single-Intensity Measurement**

Cheng Zhang , Meiqin Wang , Qianwen Chen, Dong Wang, and Sui Wei

Research Article (7 pages), Article ID 8643819, Volume 2018 (2018)

## Research Article

# Depth Analysis of Greyscale Integral Images Using Continuous Multiview Wavelet Transform

Vladimir Saveljev  <sup>1</sup> and Irina Palchikova <sup>2,3</sup>

<sup>1</sup>NEMO Lab., Department of Physics, Myongji University, Yongin-si, Gyeonggi-do, 17058, Republic of Korea

<sup>2</sup>Technological Design Institute of Scientific Instrument Engineering, Siberian Branch of the Russian Academy of Sciences (TDISIE SB RAS), ul. Russkaya, 41, Novosibirsk, 630058, Russia

<sup>3</sup>Department of Physics, Novosibirsk State University (NSU), ul. Pirogova, 2, Novosibirsk, 630090, Russia

Correspondence should be addressed to Vladimir Saveljev; saveljev.vv@gmail.com

Received 10 October 2018; Accepted 28 October 2018; Published 2 December 2018

Guest Editor: Xiaowei Li

Copyright © 2018 Vladimir Saveljev and Irina Palchikova. This is an open access article distributed under the Creative Commons Attribution License, which permits unrestricted use, distribution, and reproduction in any medium, provided the original work is properly cited.

The wavelet analysis of the integral images can be used in extraction of the depth of the photographed/synthesized 3D objects. The result of the analysis, however, depends on the colour/textured of the object and thus can be ambiguous. In this paper, we propose to normalize the image before processing in order to avoid such an ambiguity, and to extract the depth without regard to the colour/textured. The proposed technique is verified in multiple integral/plenoptic images and can be applied to multiview and light-field displays as well.

## 1. Introduction

There are many 3D technologies [1–3] in 3D imaging. Particularly, the wavelets are used in 3D imaging, for instance, in multiview video compression [4], in image coding [5], in image fusion [6], as a quality metric [7], etc. The disparity of stereoscopic images can be estimated [8], the shape of the photographed/synthesized objects can be analysed, and the depth can be extracted using the wavelet analysis of the integral images [9–11]. In this paper, we propose the technique to eliminate the texture effect. Based on the similarity between the 3D images, where a 3D content is represented in a single image plane consisting of the logical image cells [12], our results can be applied to integral [13–15], multiview [16–18], plenoptic images, and light-field displays [19–21].

The result of the wavelet analysis of 3D images, however, depends on the colour/textured of the surface of the object. This effect was noticed before, and the most images in [9–11] were binary BW images and most results were presented in a qualitative visual form. This unexpected undesirable effect must be reduced, but a solution has been unknown yet.

The intensity in any point of the image in the image plane is proportional to the brightness of the point of the object in that point. The intensity of all separated parts of voxel pattern [22] is equal to the brightness of the corresponding point of the object. The voxel patterns precede the wavelets; thus, this important property is kept in wavelets. Therefore, the wavelet coefficients depend on the colour; and the result of the wavelet analysis of a multiview image is proportional to the brightness of voxels (or pieces of surface in a texture model).

Define the central view (CV) of an integral image as an image, where the central pixels of all image cells of the integral image are assembled in accordance with the location of the cells; i.e., the centre pixel of the left top cell goes to the left top corner of the CV, the centre pixel of the right top cell goes to the right top corner of the CV, etc.; such image can be seen by a hypothetic (nonexistent) camera located at the centre of the lens array.

The CV can be calculated by applying the known interlacing technique (see, e.g., [23]) along both dimensions of the integral image. The CV can be calculated for binary, greyscale, or colour images; see Figure 3. In our paper, the CV is solely

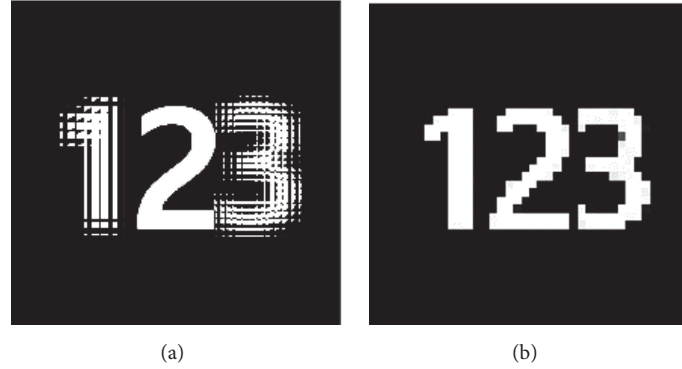


FIGURE 1: (a) Binary BW integral image of digits 800 x 800 pixels (credits for the original colour image to Prof. B. Lee, SNU); (b) the central view (CV) of this image (as seen through the camera located behind the central microlens of the lens array) 40 x 40 pixels.

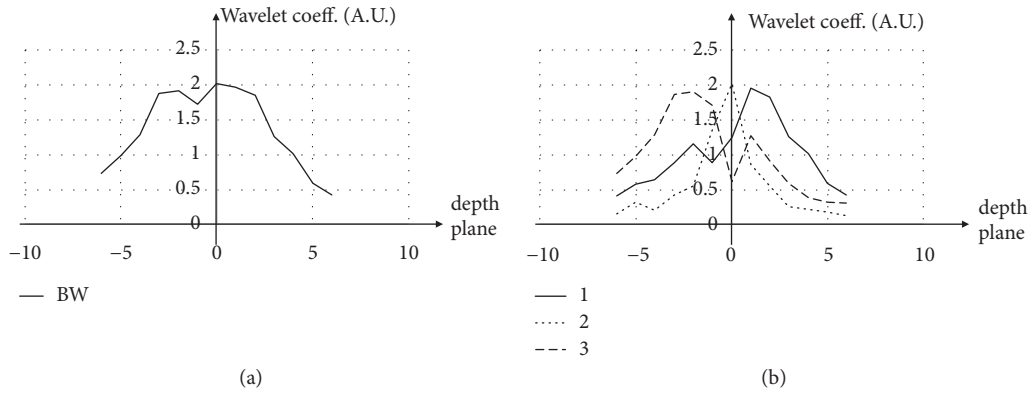


FIGURE 2: Wavelet coefficients of binary BW image Figure 1: (a) whole image, (b) each digit separately. (The depth plane is an integer number.)

used as a simple graphical picture of all objects of a 3D image, because in the original integral image, the objects may look unclear (nonsharp, or out-of-focus, or blurred, etc.); compare Figures 1(a) and 1(b).

What is important is that it is unnecessary to calculate the CV for the wavelet transform, and therefore not a one operation with the wavelets needs the CV. In this context, the central view is nothing but a descriptive illustration for the journal paper.

Later in this paper we will name an integral/plenoptic image by its CV (as “in Figure 1(b)”), but actually such a referencing will mean the integral image (i.e., “Figure 1(a)”) which corresponds to the named CV.

Previously, the colour dependence remained behind the scene, and the depth was mixed with colours. In this paper, as soon as we know an answer, we tried to open a door, slightly. To restore the depth more correctly, we propose to use the normalized image. Firstly, we would like to illustrate the dependence on colours in the wavelet analysis of the integral images.

## 2. Dependence of Wavelet Coefficients on Colours

Consider colours of three digits in the 123-image. If all colours are identical (as in the BW image in Figure 1), then the wavelet

coefficients are the same for every digit. Note that it is a repainted colour image, originally provided by Prof. B. Lee.

The wavelet analysis of the binary BW image Figure 1 shows almost uniform shape (a flat-top curve) for the depth planes between -6 and +6, where the digits of this 3D image are presumably located in space; see Figure 2(a). The wavelet coefficients for each digit processed separately are shown in Figure 2(b), where all three maxima are close to each other.

Based on Figure 2(b), one may conclude that the digit 1 is located between the +1<sup>st</sup> and +2<sup>nd</sup> planes, digit 2 in 0<sup>th</sup>, digit 3 between -2<sup>nd</sup> and -3<sup>rd</sup> planes. Outside of this region ( $|depth| > 3$ ), the wavelet coefficients monotonously decay. Therefore later in the related Figures 4 and 5, we will show the wavelet coefficients within the depth region [-2, +2] only, where the expected result is a flat-top horizontal line.

Then, if the shades of grey of digits or their colours are not the same as in Figure 3, the expected results of the wavelet analysis would be different for every digit.

The results of the wavelet analysis (wavelet coefficients) of greyscale images, Figures 3(a) and 3(b), are shown in Figure 4(a). The wavelet coefficients of the colour digits, Figures 3(c) and 3(d), are shown in Figure 4(b).

There is an essential difference between the wavelet coefficients of digits of various colours. In all cases, instead of a flat top and decay (as in Figure 2(a) for the binary image),

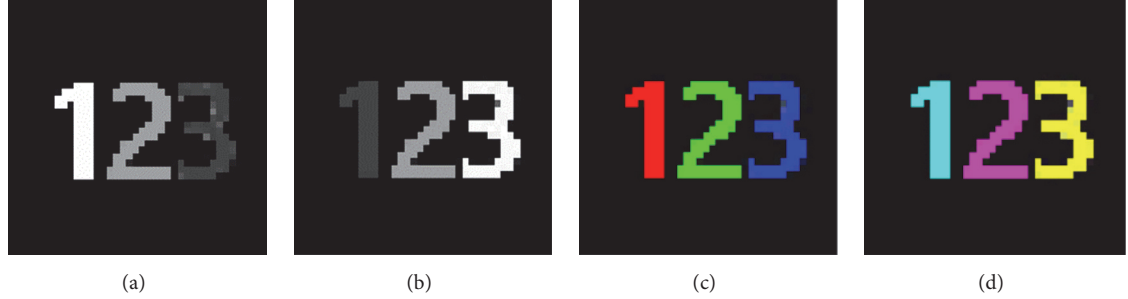


FIGURE 3: Various grey levels and colours of digits (CVs).

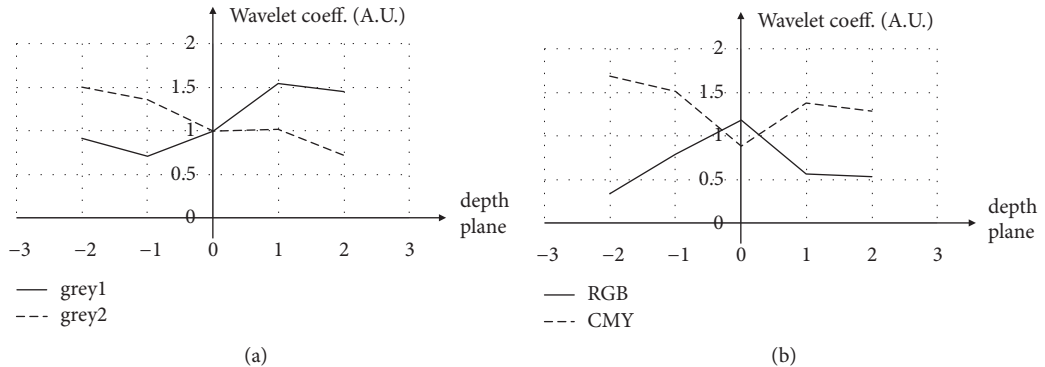


FIGURE 4: Wavelet coefficients of images from Figure 2: (a) grey-scale, (b) colour.

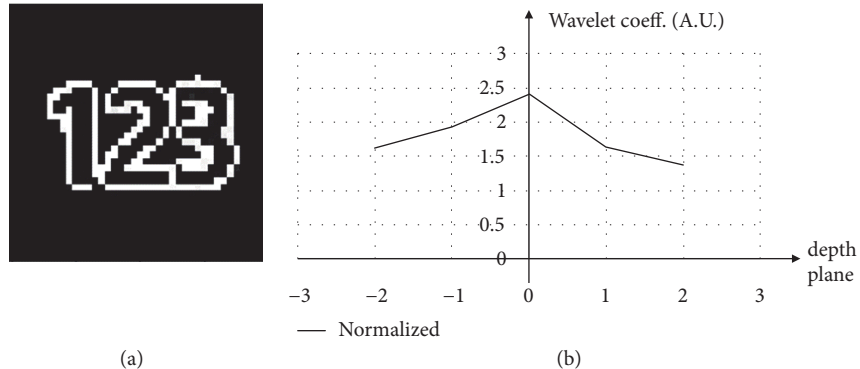


FIGURE 5: (a) Normalized image (CV). (b) Wavelet coefficients of normalized image.

the wavelet coefficients of grey images may rise up, fall down, or have a maximum or minimum in the middle; see Figure 4. These graphs can be treated ambiguously: either the digits in the same plane have different colours, or the digits of the same colour are located at different distances. A variety of intermediate interpretations is also possible.

This confirms a strong dependence of the results on the colours of voxels (texture); it is an undesirable side effect in the depth (shape) extraction. Below, we describe how to eliminate it.

### 3. Materials and Methods

In our examples, the source images are integral/multiview/plenoptic images with the square grid of the image cells (a

cell is an area under a lenticular lens). The images were taken from different independent sources, either photographs or synthesized (computer-generated) images.

The multiview wavelets and the algorithm of the continuous multiview wavelet transform are exactly the same as presented in our previous paper about the multiview wavelets [10, 11].

In order to avoid the undesirable effect of texture and to restore the spatial structure without regard to the colours, we propose to process so-called normalized image [24]. A normalized image is typically used in order to reduce a nonuniform illumination in a local neighbourhood. The normalized image can be built by the algorithm [25]. The normalized image corresponding to the original image of digits

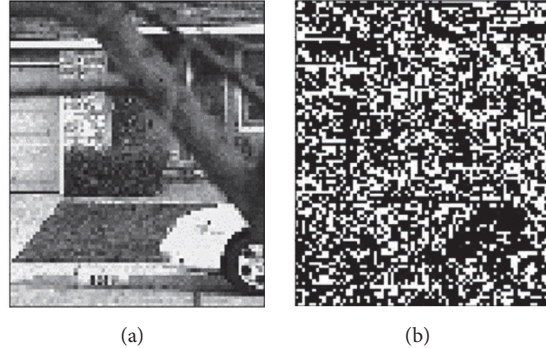


FIGURE 6: Source and normalized images of the house (CVs). The original colour image “house crop” is available “for free” at the website by T. Georgiev [26].

Figure 1 is shown in Figure 5(a). The result of the wavelet analysis of this normalized image is shown in Figure 5(b).

Despite insignificant imperfection (such as non-100% horizontal flat top), the graphs in Figures 2(a) and 5(b) are similar to each other more than any graphs in Figure 4. This means that the normalized image predominantly contains the information about the 3D structure (depth), rather than about colours (texture). For instance, the RMS difference of the wavelet coefficients between the processed RGB and BW images is 1.2 A.U. (normalized RMS error 60%); in grey and BW images it is 0.7 A.U. (48%); however, in BW and normalized images it is 2.5 – 4.2 times less (0.3 A.U, 19%). This is not a complete elimination of the undesirable effect, but its essential reduction.

Before processing, the colour images were transformed into the grey-scaled images, but it is not necessary. The full-colour images can be processed as well, by processing the R, G, B colour components separately.

The dimensions of the images are as follows: the image of digits is 800 x 800 pixels (CV and normalized image are 40 x 40 pixels), the rabbit 1350 x 1350 (CV and normalized 45 x 45), the books 4031 x 4031 pixels (CV and normalized 139 x 139), and the house 4575 x 4575 pixels (CV and normalized 75 x 90).

## 4. Results

To illustrate the proposed technique, we applied it to plenoptic/integral images from various sources. The normalization is followed by the wavelet transform. In the examples, we will compare the results (i.e., the wavelet coefficients for the source and normalized images) by the depth planes and along the rows (horizontal lines) in the array of the coefficients.

The original and normalized images of the house are shown in Figure 6 (recall, this is a CV).

Consider, for example, the depth plane 0 and the row 70 of this image. The boundary line between the path and the lawn is at the same time the line of the change of colour of the texture. Because of that, the depth of this line is concealed (hidden) in the original image; see the wavelet coefficients and the graph along the horizontal row in Figures 7(a) and 7(b). What is important is that in the normalized image, this

line can be clearly seen as a separate pulse in Figures 7(c) and 7(d).

N.B. The first image of each pair in Figure 7 displays the modulus of the wavelet coefficients (the black colour means maximum, and the white colour means zero), while the second graph is the full profile along the selected row. The same layout will be used later in Figures 9, 11, and 12.

Also, note the difference in the average (mean) level on the body of the car between the columns 45 and 65 as indicated by the dashed line in Figures 7(b) and 7(d). The influence of the texture colour of the body of the car is clearly reduced in Figure 7(d) down to the average level of that row.

The source and normalized images of books are shown in Figure 8.

In this example, we consider the depth plane -1, the row 95. Figures 9(c) and 9(d) clearly show a recognized 3D edge (backbone of the book) as a separate pulse, but not a texture-induced effect (a step pulse) as in Figures 9(a) and 9(b).

The influence of the texture is reduced in this image too. The average level at the cover of the book is almost the same along the row in the processed normalized image (shown in Figures 9(b) and 9(d) by the dashed line).

N.B. The letters “EG” on the cover of the book in Figure 9(a) are not a restored 3D structure, rather a texture of the surface.

The source and normalized images of the rabbit are shown in Figure 10. In the 3D analysis, two planes will be considered.

(1) Plane 2, row 13. The eye of the rabbit becomes clearly recognized in the normalized image, while it is completely invisible in the unnormalized one; see Figure 11.

(2) Plane 5, row 17. The same is valid for the nose. The nose is clearly recognized in the processed normalized image, while it is hidden in the source (unnormalized) image; see Figure 12.

These two examples also demonstrate that the influence of the texture is reduced in the normalized images, so as some previously unrecognized features appear.

## 5. Discussion

We processed the greyscale images. Before processing, the colour images (if any) were transformed into the grey-scaled

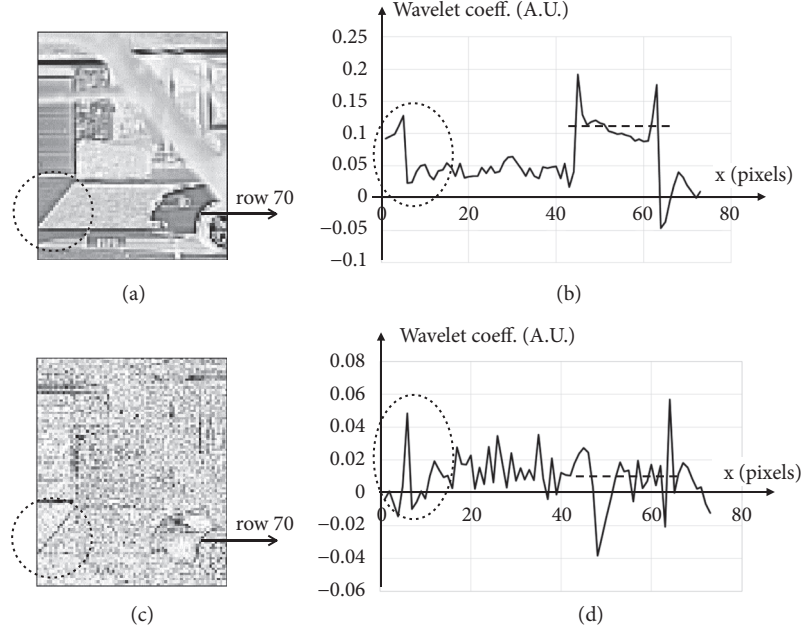


FIGURE 7: Wavelet coefficients of source image (picture and graph on the top) and normalized image (on the bottom): modulus of the wavelet coefficients in (a), (c); the wavelet coefficients along the row 70 in (b), (d).

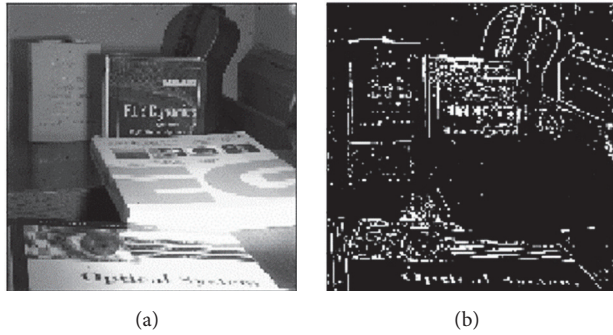


FIGURE 8: Source and normalized images of books (CVs). The original colour image “input” is available “for free” at the website of T. Georgiev [26].

images, but it is not necessary. The full-colour images can be processed as well, by processing the RGB colour components. Also, we used the BW normalized image; however in general, each colour component can be normalized individually, and a colourful normalized image could be obtained.

The numeration of the rows and columns in the array of the wavelet coefficients is slightly different from that of rows and columns in the CV, because of the different sizes. (The size of the CV is fixed, but the array size at each depth plane varies, because we did not make any assumptions about the behaviour of the image beyond the sides of the original image.) The difference is less than the number of the current depth plane, but this small difference is out of the scope of the current paper.

The 3D images used in this paper were obtained by the independent authors either from a plenoptic camera (Figures

6 and 8) or by means of the computer simulation of the integral imaging (Figures 1 and 10). In either case, a lens array with a square grid of microlenses or its computational equivalent was used. The high quality lens arrays are known for their very uniform structure (a small deviation of the lens pitch across the array). The proposed image processing procedure can be applied to the 3D images built on the hexagonal grid of the lenses (with properly redesigned wavelets).

Instead of a lens array, the 3D images can be also obtained from a camera array, as described in [27] and in the references in [3]; on the other hand, the layout of cameras in the camera array might be less uniform than that of the lens array. Moreover, the 3D imaging with the sensors at random locations is demonstrated [28]. Therefore, we hope that a wavelet processing can be in principle applied to 3D images from the camera arrays; however the wavelets have to be radically modified in this case.

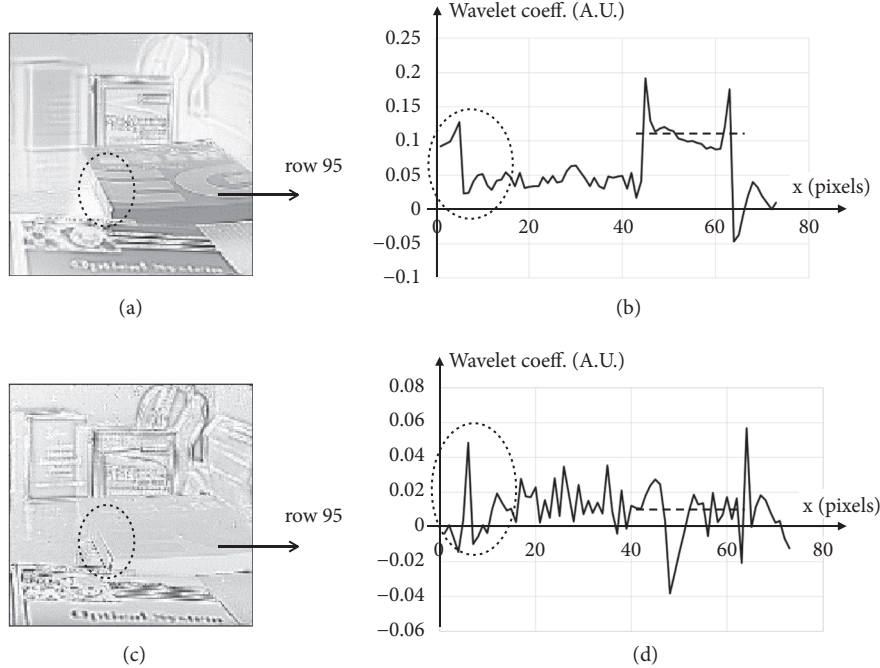


FIGURE 9: Wavelet coefficients (modules on the left, graph along the row 95 on the right) of source (top) and normalized (bottom) images. The layout is the same as in Figure 7.

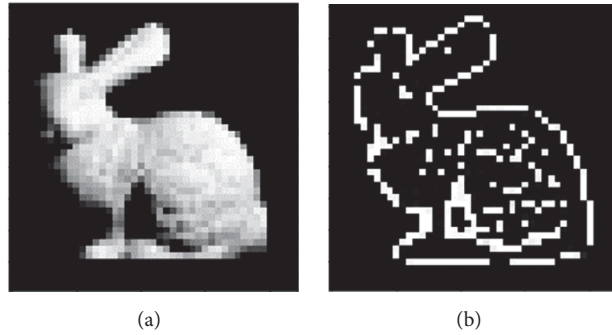


FIGURE 10: Source and normalized images of rabbit (CVs). The original colour image was provided by Prof. Lee by a personal request.

In the normalization of the most images (only a few of many processed images are presented in this paper), we used the default values  $\sigma_1 = 18$ ,  $\sigma_2 = 24$ ; however in a few cases, these values were reduced to  $\sigma_1 = 4.5$ ,  $\sigma_2 = 6$ .

## 6. Conclusions

The influence of colours (texture) is essentially reduced by means of the normalized image instead of the source full-colour or greyscale image. The technique is confirmed by processing integral/plenoptic images from independent sources. The numerical comparison became possible between the planes and within each plane (because the wavelet coefficients are normalized by definition, and because the integral image itself is used in the normalized form). Integral, multiview, plenoptic (light-field) images with the square grid of cells can be processed. Colour images can be processed as well. The

proposed technique can be efficiently used in 3D imaging for the depth extraction and the shape reconstruction without regard to the colour/texture.

## Data Availability

The plenoptic/integral image data used to support the findings of this study were obtained from two sources. Namely, two of four images we used in the examples are available for free on the website "<http://www.tgeorgiev.net/>" by Dr. T. Georgiev [26]; the other two images were kindly supplied by Prof. B. Lee upon our personal request.

## Conflicts of Interest

The authors declare that there are no conflicts of interest regarding the publication of this paper.

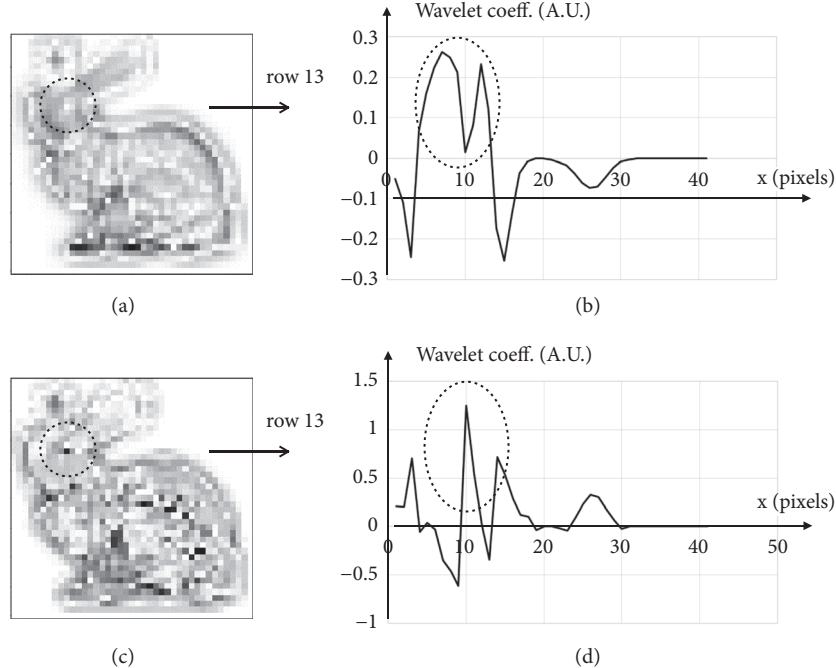


FIGURE 11: Wavelet coefficients in 2<sup>nd</sup> plane for source and normalized images, row 13 on the right. The layout is the same as in Figure 6.

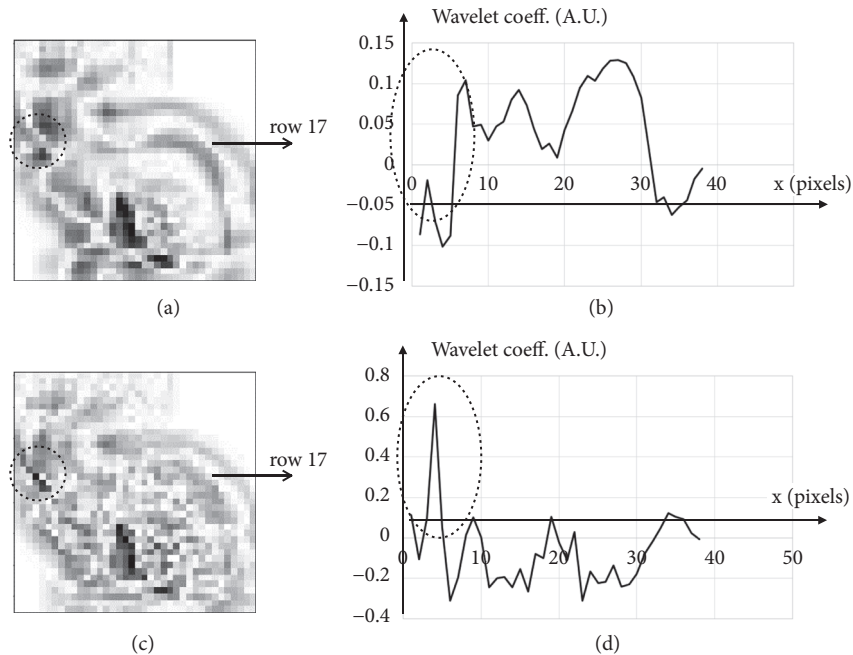


FIGURE 12: Wavelet coefficients in 5<sup>th</sup> plane for source and normalized images, row 17 on the right. The layout is the same as in Figure 6.

## Acknowledgments

This work was partially supported for one author (Prof. I. Palchikova) by the Russian Foundation for Basic Research and by the Ministry of Education, Science, and Innovative Policy of the Novosibirsk Region within the framework of

the research [project No. 17-47-540269]. We greatly appreciate Prof. B. Lee for the images provided to us personally (the digits and the rabbit). Also, we are thankful to Dr. T. Georgiev for his wonderful and very useful website (research until 2014), particularly, for the images available at that site for free (the input and the house crop).

## References

- [1] J. Hong, Y. Kim, H. Choi et al., "Three-dimensional display technologies of recent interest: principles, status, and issues," *Applied Optics*, vol. 50, no. 34, pp. H87–H115, 2011.
- [2] J.-Y. Son, B. Javidi, and K.-D. Kwack, "Methods for displaying three-dimensional images," *Proceedings of the IEEE*, vol. 94, no. 3, pp. 502–522, 2006.
- [3] M. Martínez-Corral and B. Javidi, "Fundamentals of 3D imaging and displays: a tutorial on integral imaging, light-field, and plenoptic systems," *Advances in Optics and Photonics*, vol. 10, no. 3, p. 512, 2018.
- [4] M. Flierl and B. Girod, "Multiview video compression," *IEEE Signal Processing Magazine*, vol. 24, no. 6, pp. 66–76, 2007.
- [5] W. Yang, Y. Lu, F. Wu, J. Cai, K. N. Ngan, and S. Li, "4-D wavelet-based multiview video coding," *IEEE Transactions on Circuits and Systems for Video Technology*, vol. 16, no. 11, pp. 1385–1395, 2006.
- [6] J. L. Rubio-guivernau, V. Gurchenkov, M. A. Luengo-oroz et al., "Wavelet-based image fusion in multi-view three-dimensional microscopy," *Bioinformatics*, vol. 28, no. 2, pp. 238–245, 2012.
- [7] P. B. Zadeh and C. V. Serdean, "Stereo video disparity estimation using multi-wavelets," in *Proceedings of the Seventh International Conference on Digital Telecommunications (ICDT)*, pp. 50–54, 2012.
- [8] E. Bosc, F. Battisti, M. Carli, and P. Le Callet, "A wavelet-based image quality metric for the assessment of 3D synthesized views," in *Proceedings of the 24th IS and T/SPIE Stereoscopic Displays and Applications Conference, SD and A 2013*, vol. 8648, USA, February 2013.
- [9] V. Saveljev, "Wavelets and continuous wavelet transform for autostereoscopic multiview images," *Journal of Electrical Engineering*, vol. 4, no. 1, pp. 19–23, 2016.
- [10] V. Saveljev and I. Palchikova, "Analysis of autostereoscopic three-dimensional images using multiview wavelets," *Applied Optics*, vol. 55, no. 23, pp. 6275–6284, 2016.
- [11] V. Saveljev and I. Palchikova, "Analytical model of multiview autostereoscopic 3D display with a barrier or a lenticular plate," *Journal of Information Display*, vol. 19, no. 2, pp. 99–110, 2018.
- [12] V. V. Saveljev and S.-J. Shin, "Layouts and cells in integral photography and point light source model," *Journal of the Optical Society of Korea*, vol. 13, no. 1, pp. 131–138, 2009.
- [13] S.-G. Park, J. Yeom, Y. Jeong, N. Chen, J.-Y. Hong, and B. Lee, "Recent issues on integral imaging and its applications," *Journal of Information Display*, vol. 15, no. 1, pp. 37–46, 2014.
- [14] X. Xiao, B. Javidi, M. Martinez-Corral, and A. Stern, "Advances in three-dimensional integral imaging: Sensing, display, and applications," *Applied Optics*, vol. 52, no. 4, pp. 546–560, 2013.
- [15] J.-H. Park, K. Hong, and B. Lee, "Recent progress in three-dimensional information processing based on integral imaging," *Applied Optics*, vol. 48, no. 34, pp. H77–H94, 2009.
- [16] N. A. Dodgson, "Analysis of the viewing zone of multi-view autostereoscopic displays," in *Proceedings of the Stereoscopic Displays and Virtual Reality Systems IX*, vol. 4660, pp. 254–265, USA, January 2002.
- [17] B.-R. Lee, J.-J. Hwang, and J.-Y. Son, "Characteristics of composite images in multiview imaging and integral photography," *Applied Optics*, vol. 51, no. 21, pp. 5236–5243, 2012.
- [18] Y. Takaki, K. Tanaka, and J. Nakamura, "Super multi-view display with a lower resolution flat-panel display," *Optics Express*, vol. 19, no. 5, pp. 4129–4139, 2011.
- [19] R. Ng, M. Levoy, M. Bredif, G. Duval, M. Horowitz, and P. Hanrahan, "Light field photography with a hand-held plenoptic camera," Stanford [Tech Report], CTSR 2005-02, April 2005.
- [20] T. Georgiev and A. Lumsdaine, "Focused plenoptic camera and rendering," *Journal of Electronic Imaging*, vol. 19, no. 2, 2010.
- [21] J. Kim, S. Moon, Y. Jeong, C. Jang, Y. Kim, and B. Lee, "Dual-dimensional microscopy: real-time in vivo three-dimensional observation method using high-resolution light-field microscopy and light-field display," *Journal of Biomedical Optics*, vol. 23, no. 6, pp. 1–11, 2018.
- [22] M.-C. Park, S. Ju Park, V. V. Saveljev, and S. Hwan Kim, "Synthesizing 3-D images with voxels," in *Three-Dimensional Imaging, Visualization, and Display*, pp. 207–225, Springer, 2009.
- [23] P. V. Johnson, J. Kim, and M. S. Banks, "Stereoscopic 3D display technique using spatiotemporal interlacing has improved spatial and temporal properties," *Optics Express*, vol. 23, no. 7, pp. 9252–9275, 2015.
- [24] D. Sage and M. Unser, "Teaching image-processing programming in Java," *IEEE Signal Processing Magazine*, vol. 20, no. 6, pp. 43–52, 2003.
- [25] D. Sage, "Local Normalization," *Web-Page*, 07 Sep. 2018, <http://bigwww.epfl.ch/sage/soft/localnormalization/>.
- [26] T. Georgiev, "Research in the area of light fields until 2014," *Web-Page*, 13 Sep. 2018, <http://tgeorgiev.net/>.
- [27] Y. Xing, Z.-L. Xiong, M. Zhao, and Q.-H. Wang, "Real-time integral imaging pickup system using camera array," in *Proceedings of the Advances in Display Technologies VIII*, vol. 10556, p. 12, San Francisco, USA, January 2018.
- [28] M. DaneshPanah, B. Javidi, and E. A. Watson, "Three dimensional imaging with randomly distributed sensors," *Optics Express*, vol. 16, no. 9, pp. 6368–6377, 2008.

## Research Article

# Study on Quantitative Phase Imaging by Dual-Wavelength Digital Holography Microscopy

**Lin Hu, Yunxiu Shui, Yaohui Dai, Haiyu Wu, Gang Zhu, and Yan Yang** 

*College of Mechanical Engineering, Chongqing University of Technology, Chongqing 400054, China*

Correspondence should be addressed to Yan Yang; yangyan@cqu.edu.cn

Received 15 October 2018; Revised 18 October 2018; Accepted 21 October 2018; Published 1 November 2018

Guest Editor: Xiaowei Li

Copyright © 2018 Lin Hu et al. This is an open access article distributed under the Creative Commons Attribution License, which permits unrestricted use, distribution, and reproduction in any medium, provided the original work is properly cited.

A dual-wavelength digital holographic microscopy with premagnification is proposed to obtain the object surface measurements over the large gradient. The quantitative phase images of specimens are captured in high precision by the processing of filtering and phase compensation. The phase images are acquired without phase unwrapping, which is necessary in traditional digital holographic microscopy; thereby the proposed system can greatly increase the speed of reconstruction. The results of numerical simulation and optical experiments demonstrated that the reconstructed speed increased by 37.9 times, and the relative error of measurement is 4% compared with the traditional holographic microscopy system. It means that the proposed system can directly acquire the higher quality quantitative phase distribution for specimens.

## 1. Introduction

Digital holographic microscopy (DHM) is a powerful technology for the measurement of microscopic samples by recording and reconstructing the amplitude and phase of the wave. The dual-wavelength digital holographic microscopy uses two different wavelength lasers to simultaneously record the hologram and numerically reconstruct the phase information according to phase distribution under two wavelengths. As early as 1998, a new method for the extraction of quantitative phase imaging by using partially coherent illumination and an ordinary transmission microscope was proposed by A. Barty et al., which can recover a phase even in the presence of amplitude modulation [1]. A solution for absolute phase measurements was presented by Cuche Etienne et al. [2]. They introduced digital reference wave and phase mask, which were applied in phase-contrast imaging and optical meteorology. This property of holograms offers phase-contrast techniques, which can be used in quantitative 3D imaging. The compensation of the inherent wave front curvature by subtracting the reference hologram in DHM for quantitative phase-contrast imaging is introduced by Ferraro, Pietro, et al. [3]. This simple method can be implemented efficiently under the ideal experimental conditions. The dual-wavelength phase-shifting digital holography that selectively

extracts wavelength information from five wavelength-multiplexed holograms is presented by Tahara, Tatsuki, et al. [4]. The color hyperchaotic image encryption method by the DHM and CA encoding algorithm is proposed by Sichuan University, which has great security and robustness [5, 6]. It is an important application about digital holography. The enhanced quantitative three-dimensional measurement system is introduced by JaeYong Lee. It can simplify the configuration by a dual-peak quantum dot wavelength converter and a blue LED [7]. There are great researches for reducing speckle noise and increasing the speed of reconstruction [8–10]. We have successfully achieved the near real-time three-dimensional surface measurement by digital holography [11, 12].

If the optical path difference is less than the equivalent wavelength, the real phase distribution of object can be directly obtained without phase unwrapping by the dual-wavelength digital holographic interferometry. If the optical path difference is greater than the equivalent wavelength, the phase unwrapping process will be simplified by dual-wavelength digital holographic interferometry. The noise immunity and the scope of phase unwrapping algorithms will be improved and expanded, respectively [13–15]. C. J. Mann obtained the measurement results of the surface height over several microns of range by three-wavelength digital

holography [16]. The optical path length can be converted to physical thickness, and the sample height information will be provided. The dual-wavelength DHM imaging experiment of a stepped phase plate and the smoke particles were conducted by P. Song et al. [17]. M.K. Kim et al. successfully achieved three-dimensional imaging of resolution plates and cancer cells using dual-wavelength DHM [18]. A phase-imaging technique to quantitatively study the three-dimensional structure of cells by simultaneous dual-wavelength reflection digital holography was presented by A. Khmaladze et al. [19]. It proves that the dual-wavelength DHM allows a faster imaging, which does not rely on the surrounding pixels to correct the phase discontinuities, but simply compares two single-wavelength phases. Dual-wavelength DHM has been widely applied in the fields of surface topography measurement [20–22], cell imaging [23, 24], 3D particle imaging [25, 26], transparent medium physical quantity measurement [27–29], and so on. Due to the limitation of the dual-wavelength DHM technique, more noise will be introduced with the increase in synthesis wavelength and the expanding of the sample range. The accuracy of measurement decreased as the noise increased. The setup of dual-wavelength DHM consists of two laser machines, which makes it difficult to ensure the concentricity of two laser beams in an optical assembly. All the above have the adverse effects on obtaining high precision phase information.

A system of dual-wavelength DHM with premagnification, which can directly and accurately obtain quantitative phase images, is presented. The principle of surface topography measurement and phase unwrapping method based on dual wavelength digital holography is introduced. The effectiveness of the system is verified by computer simulations and optical experiments using the 1951 USAF target and the standard groove object. Compared with the traditional single wavelength DHM, the system can not only obtain the phase information without phase unwrapping, but also get the low noise and high precision quantitative phase images.

## 2. Experimental Principle

**2.1. Principle.** In dual-wavelength digital holographic microscopy, two laser beams in different wavelengths from separated laser sources are coupled into one beam, and the optical assemblies are shown in Figure 1. The two lasers were used as coherent light sources. Both beams are collimated by spatial filter. Beam splitters (BS1) divide the beams into the reference and the object arms. The object beam passes through the sample and microscope objective. There are different tilts in orthogonal directions for reference waves of two lasers, which allows us to capture both wavelengths simultaneously. Then the interference pattern between the reference waves and object wave is recorded by a CCD camera.

The dual-wavelength composite digital hologram will be acquired on the CCD, and the interference pattern can be expressed as

$$\begin{aligned} I_H(x, y) = & |O_1|^2 + |R_1|^2 + |O_2|^2 + |R_2|^2 + R_1^* O_1 \\ & + R_1 O_1^* + R_2^* O_2 + R_2 O_2^* \end{aligned} \quad (1)$$

where  $I_H$  is the intensity of the composite digital hologram,  $x, y$  are the coordinates of the holographic plane,  $*$  is the complex conjugate,  $O_1, O_2$  are object beams, and  $R_1, R_2$  are reference beams.

The interferometric phase can be extracted by the spatial filtering method and shifted to the center position to perform the Fourier transform. The complex amplitude distribution of the reproducing light field can be obtained as follows:

$$O_i(x, y) = R_i(x, y) [R_i^*(x, y) O_i(x, y)] \quad i = 1, 2 \quad (2)$$

The intensity and the wavefront phase distribution of optical field can be calculated according to the following expressions:

$$I_i(x, y) = O_i(x', y') R_i^*(x', y') \quad (3)$$

$$\Phi_i(x, y) = \arctan \left[ \frac{\text{Im} O_i(x', y')}{\text{Re} O_i(x', y')} \right] \quad (4)$$

In order to overcome the issue of phase ambiguity produced by single wavelength approach, a synthetic beat-wavelength is used and expressed as follows:

$$\Phi = \Phi_1(x, y) - \Phi_2(x, y) = 2\pi \frac{nh}{\lambda_1} - 2\pi \frac{nh}{\lambda_2} = 2\pi \frac{nh}{\Lambda} \quad (5)$$

where  $h$  is the height distribution of the specimens, which means the optical path difference of the twice of the topography for reflection scheme.  $nh$  is the optical path difference of the homogeneous sample in the air.  $\Lambda$  is the equivalent wavelength defined as follows:

$$\Lambda = \frac{\lambda_1 \lambda_2}{|\lambda_1 - \lambda_2|} \quad (6)$$

If the optical path difference is less than the equivalent wavelength, the real phase of specimens can be directly obtained without unwrapping. Otherwise, the phase distribution is wrapped between  $-\pi$  and  $+\pi$ . In this case, the package phase difference is compensated to obtain its equivalent phase.

$$\Phi \begin{cases} \Phi_1(x, y) - \Phi_2(x, y) & \Phi > 0 \\ \Phi_1(x, y) - \Phi_2(x, y) + 2\pi & \Phi < 0 \end{cases} \quad (7)$$

In summary, the dual-wavelength digital holographic microscopy to measure the large gradient of specimens can solve the problem of phase unwrapping with single-wavelength digital holographic microscopy. As the range of measurement increases, the noise of the phase distribution in the single-wavelength digital holographic microscope also increases. Therefore, the reasonable choice of wavelength and the method of noise reduction are key points in the dual-wavelength holographic microscopy.

## 3. Experimental Results

**3.1. Experimental Setup.** The experiments were conducted in a DHM developed by our team. The schematic diagram and

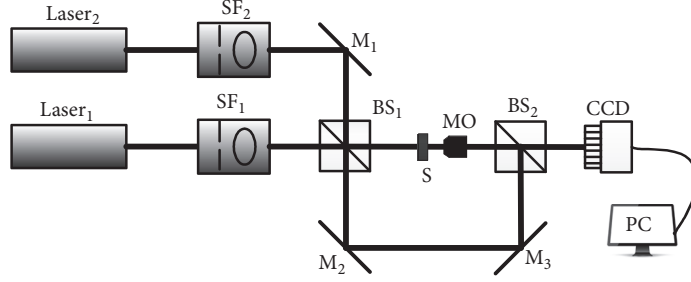


FIGURE 1: The schematic diagram of dual-wavelength digital holographic microscopy. SF, spatial filter; M, mirrors; BS, beam splitters; S, sample; MO, microscope objective; CCD, charge-coupled devices; PC, personal computer.

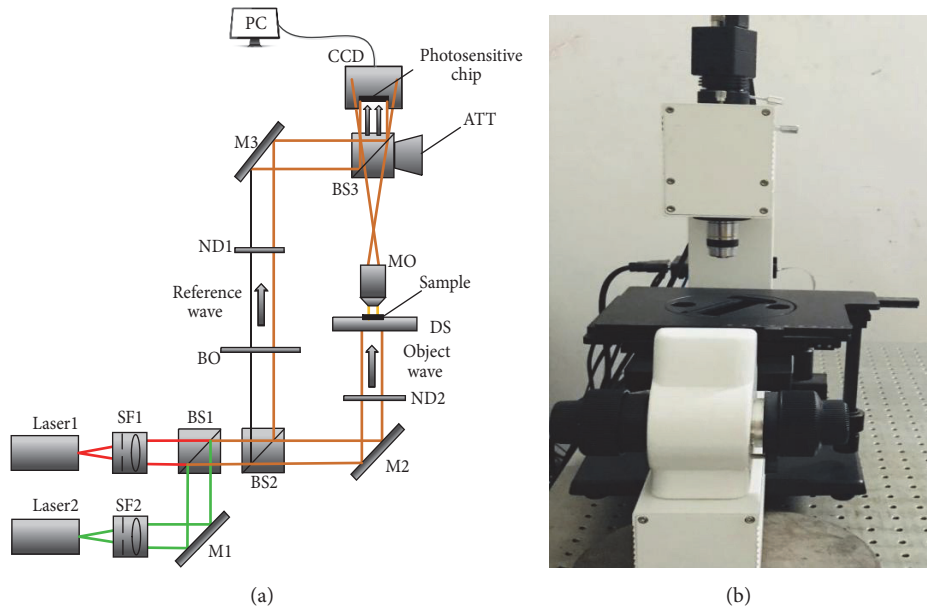


FIGURE 2: (a) The schematic diagram of the dual-wavelength DHM system. SF, spatial filter; BS, beam splitters; M, mirrors; ND, neutral density; DS, displacement stage; S, sample; MO, microscope objective; ATT, adjustable tilting stage; BO, beam obstacle. (b) Real picture of DHM.

the setup are shown in Figure 2, where  $\lambda_1 = 632.8 \text{ nm}$  and  $\lambda_2 = 532 \text{ nm}$ , the equivalent wavelength,  $\Lambda = 3.34 \mu\text{m}$ . The beams emitted by the two lasers pass through the beam expanders and collimation systems (SF), the mirror and the cube beam splitting prism (BS). Then the beam is divided into two beams by beam splitter; one is object wave, and the other is the reference wave. In the premagnification optical path, the object wave, which is reflected by mirror, passes through the microscope objective (MO,  $10\times$ ,  $NA = 0.25$ ) and the sample. On the other hand, the reference wave passes through beam obstacle and neutral density. It should be noted that beam obstacle is turned on so that the optical path is the one of off-axis digital holography (in this experiment, the beam obstacle is turned on); otherwise, it will become in-line digital holography. The two beams are combined by the cube splitting prism. Finally, the interference hologram is recorded by CCD (SENTECH STC-SBS241POE; the pixel area is  $1296 \text{ pixel} \times 966 \text{ pixel}$ ). It is worth noting that the dual-wavelength preamplification digital holographic microscopy systems with large numerical aperture microscope objectives

can acquire more sample information, which can be compressed to amplify the CCD acceptable sampling frequency [30].

**3.2. Numerical Simulation.** In order to illustrate that the phase image of sample whose optical path difference is less than the equivalent wavelength can be obtained directly and quickly by dual-wavelength DHM; a numerical simulation experiment is carried out. The computer-generated cone is a phase object with a maximum phase height of  $2.5 \mu\text{m}$ . The simulation parameters of cone are as follows:  $\lambda_1 = 632.8 \text{ nm}$ ,  $\lambda_2 = 532 \text{ nm}$ , in which each single wavelength is less than the optical path difference. According to (6), the equivalent wavelength is  $3.34 \mu\text{m}$ , which means that the dual-wavelength phase unwrapping will obtain a continuous phase distribution. Based on the designed height, the wrapping phase distribution of single-wavelength and the phase distribution of equivalent wavelength are shown in Figure 3, respectively.

To demonstrate the advantages and compare the unwrapping speed of the dual-wavelength DHM and traditional

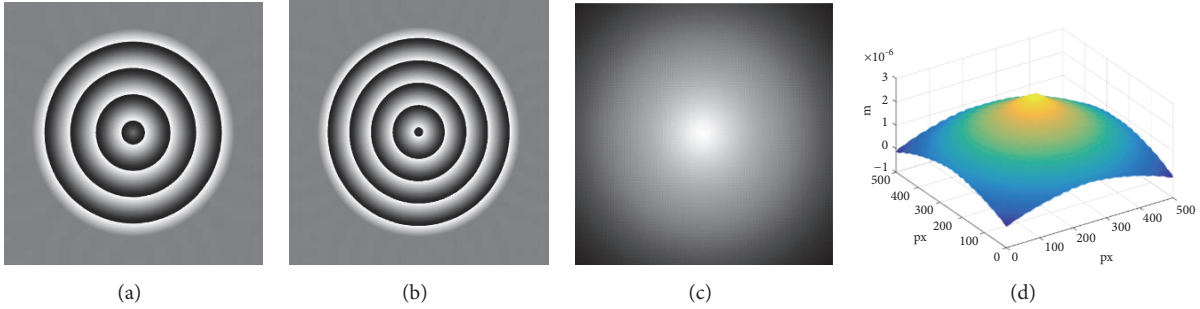


FIGURE 3: Simulation results for slope: (a) phase distribution for  $632.8\text{ nm}$ , (b) phase distribution for  $532\text{ nm}$ , (c) phase distribution for equivalent wavelength, and (d) 3D view of dual-wavelength phase distribution.

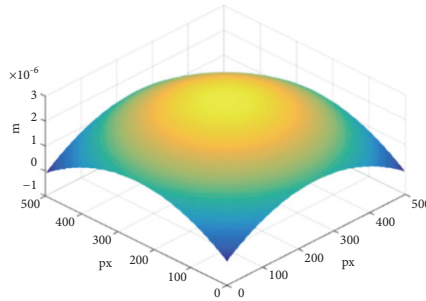


FIGURE 4: 3D view of dual-wavelength phase distribution.

single-wavelength DHM, a  $632.8\text{ nm}$  wrapped phase image is chosen to obtain the final height distribution by unwrapping procedure, which is named the quality-guided phase unwrapping algorithm. And the results for  $632.8\text{ nm}$  through the quality-guided phase unwrapping algorithm [31, 32] are shown in Figure 4.

The height distributions of cone by dual-wavelength DHM and quality-guided phase unwrapping method are compared. And the results are shown in Table 1. The results show that both of them can accurately obtain the height distribution of the cone, but in terms of time, the dual-wavelength holographic microscopy in the system is faster. The speed of reconstruction by the proposed system is 37.9 times more than the value of the quality-guided phase unwrapping method.

### 3.3. Optical Experiment

**3.3.1. Quantitative Phase Imaging of USAF 1951 Target.** Based on the dual-wavelength phase imaging system, the surface of an USAF 1951 target was measured. At the same time, the target was also measured by the scanning three-dimensional profiler (NanoMap 500LS, AEP Technology Inc., USA) and the results showed that the height was about  $0 \sim 100\text{nm}$ . Since the sample height is much smaller than the single-wavelength, the phase distribution of the sample can be obtained directly. Figures 5 and 6 present the measurement results using traditional single-wavelength and dual-wavelength, respectively.

In the reconstruction process, filtering and secondary phase distortion compensation processing are performed

[33–35]. The hologram is spectrally separated by Fourier transform. The microscope objective lens will introduce a secondary phase distortion factor in the system. In order to obtain the real phase, two holograms are recorded, which are the reference holograms for the background of the hologram and the hologram of measured sample. The real phase can be obtained by subtracting the two reconstruction phases of hologram.

The comparison of the height distribution curve along the middle symmetrical line of phase with different wavelength (in Figures 5(a), 5(b), and 6(a)) is shown in Figure 7. The height distribution along the middle symmetrical line of sample was scanned by NanoMap 500LS and its absolute height was measured to be  $54\text{ nm}$ . The average absolute height and the relative error between the measurement result and scanning result using three measurement methods are shown in Table 2.

Table 2 shows that the result of the equivalent wavelength is much closer to scanning value. From the experimental results, it can be seen that both the traditional DHM and the dual-wavelength DHM can obtain the phase distribution of the object surface. It is not hard to see that the system of dual-wavelength DHM can accurately obtain the three-dimensional morphology distribution of the object surface. The results prove that the measurement accuracy and stability of the proposed system are better than the traditional single wavelength.

**3.3.2. Quantitative Phase Imaging of Groove.** The transparent groove standard plate, which is artificially designed, was used as an experimental sample to measure its three-dimensional

TABLE 1: Comparison of two methods.

Method	Maximum phase ( $\mu\text{m}$ )	Time (s)
Quality-guided phase unwrapping	2.5749	716.61
Dual-wavelength DHM (in the system)	2.5971	18.93

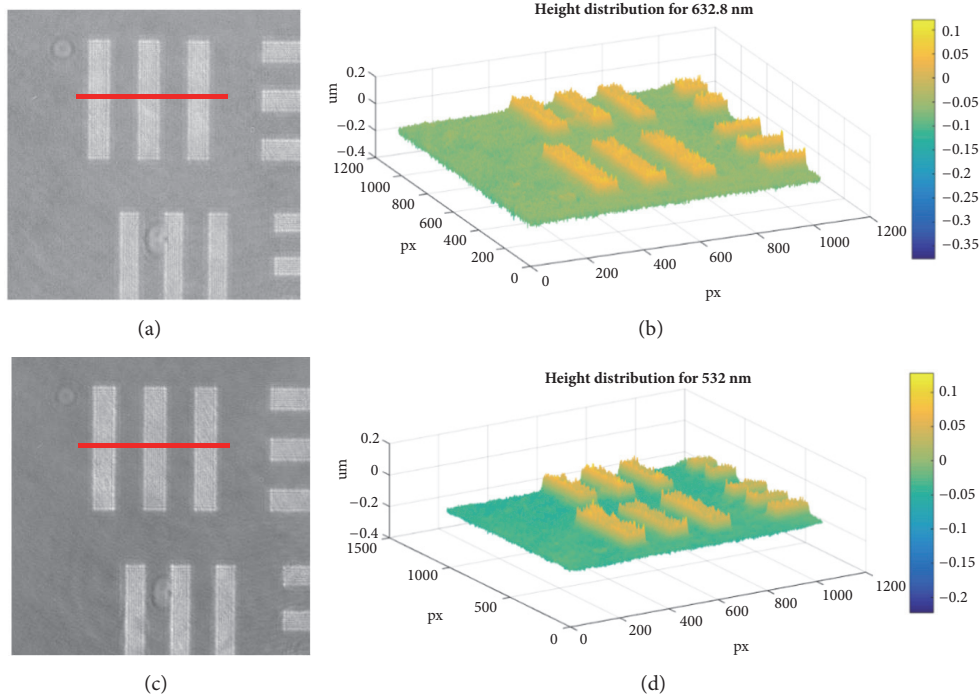
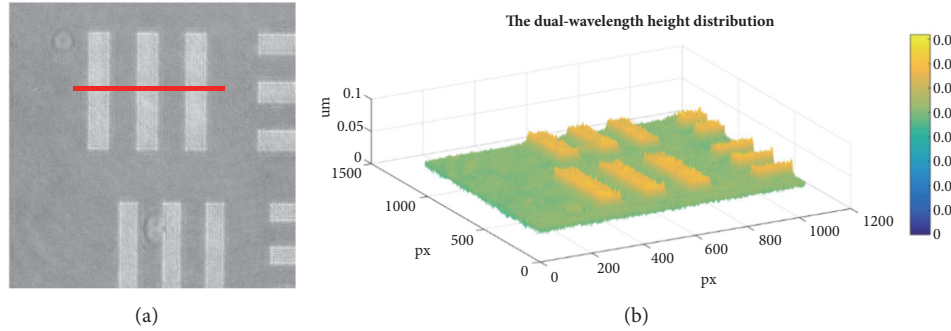
FIGURE 5: Experimental results with single wavelength measurement. (a) Phase image for  $632.8 \text{ nm}$ , (b) height distribution for  $632.8 \text{ nm}$ , (c) phase image for  $532 \text{ nm}$ , and (d) height distribution for  $532 \text{ nm}$ .

FIGURE 6: Experimental results for equivalent wavelength. (a) Phase image for equivalent wavelength, (b) 3D view of dual-wavelength height distribution.

TABLE 2: The comparison of the height distributions.

Wavelength( nm)	Absolute height ( nm)	Relative error (compared with the scanned value)	Variance
632.8	61.8	14.4%	$1.925 \times 10^{-4}$
532	99.3	83.8%	$3.188 \times 10^{-4}$
equivalent wavelength	47.5	13.8%	$1.504 \times 10^{-5}$

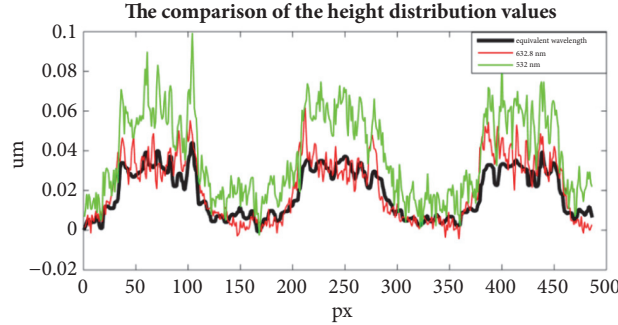


FIGURE 7: The comparison of the height distribution values along the middle symmetrical line of sample in pane Figures 5(a), 5(b), and 6(a).

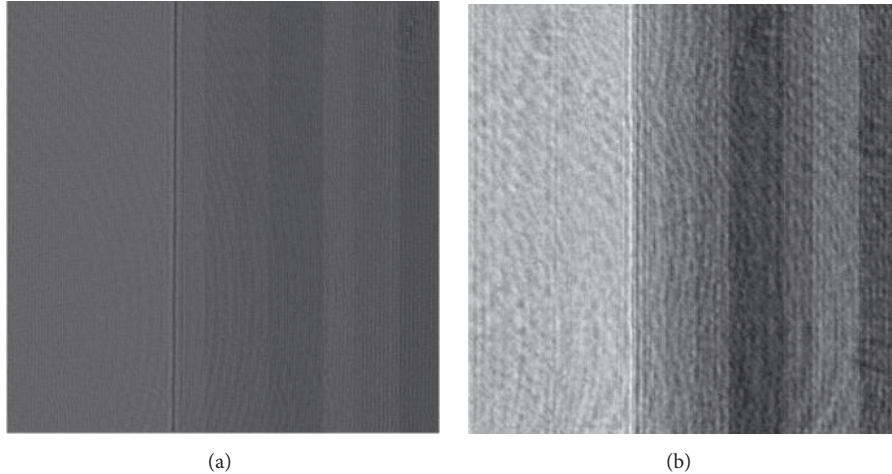


FIGURE 8: Experimental results with single wavelength measurement. (a) Phase image for 632.8 nm, (b) phase image for 532 nm.

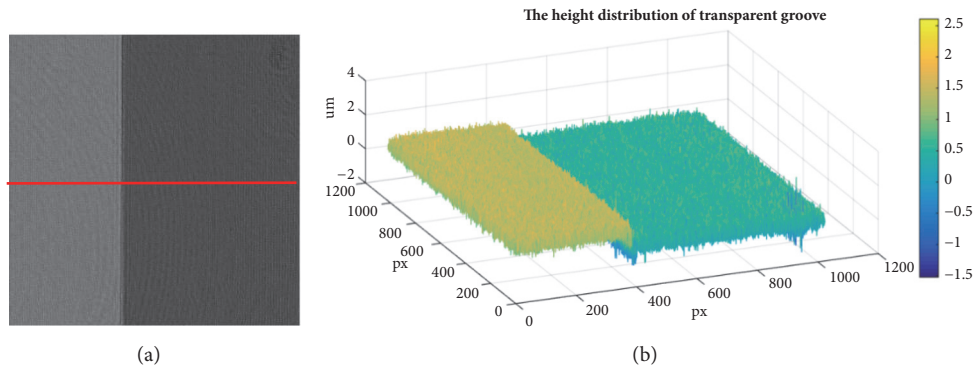


FIGURE 9: Results for equivalent wavelength. (a) Phase distribution, (b) three-dimensional height distribution.

appearance. The width of groove is 1 mm and the depth is 9  $\mu\text{m}$ . Figure 8(a) shows the phase distribution measured by wavelength, 632.8 nm. Figure 8(b) shows the phase distribution measured by wavelength, 532 nm. It is clear to see that there is phase folding in the phase distribution at each single wavelength. The phase distribution measured by the dual wavelength interference is shown in Figure 9.

The height distribution of the middle symmetrical line of the groove (Figure 9(a)) is obtained by the median filtering, which is shown in Figure 10. According to the formula of the surface profile distribution and phase distribution (in (5)),

the height difference between the base and the bottom of the groove  $b = 0.936 \mu\text{m}$ . The relative error between the actual groove height and experimental result is 4%, which is in good agreement with the theoretical values.

#### 4. Conclusions

In order to solve the quantitative phase imaging problem of traditional digital holographic microscopy system for the large gradient of object surface, a dual-wavelength preamplification digital holographic microscopy optical system is

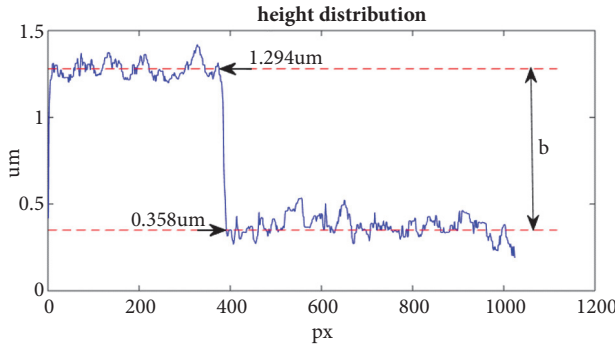


FIGURE 10: Height distribution values along the middle symmetrical line of groove in Figure 8(a).

proposed. The numerical simulation and experiments are carried out and the effectiveness of the system is verified. The experimental results of the sample phase imaging of the traditional DHM and dual-wavelength preamplification DHM system are compared. The results show that the experimental system can effectively overcome the limitations of the single-wavelength method in the imaging of complex surface objects, increase the observation speed, and simplify the reconstruction process, which further validates the effectiveness of the experimental system for quantitative phase imaging.

## Data Availability

The data used to support the findings of this study are included within the article.

## Conflicts of Interest

The authors declare that they have no conflicts of interest.

## Acknowledgments

This work has been supported by the National Natural Science Foundation of China (Nos. 11272368 and 51875068), the International Cooperation Special Project in Science and Technology of China (No. 2015DFR70480), the Chongqing Municipal Education Commission's science and technology research project (KJ1600929), and the Graduate Innovation Foundation of Chongqing University of Technology (No. ycx2018216).

## References

- [1] A. Barty, K. A. Nugent, D. Paganin, and A. Roberts, "Quantitative optical phase microscopy," *Optics Express*, vol. 23, no. 11, pp. 817–819, 1998.
- [2] E. Cuche, F. Bevilacqua, and C. Depeursinge, "Digital holography for quantitative phase-contrast imaging," *Optics Express*, vol. 24, no. 5, pp. 291–293, 1999.
- [3] A. Finizio, C. Magro, G. Pierattini et al., "Compensation of the inherent wave front curvature in digital holographic coherent microscopy for quantitative phase-contrast imaging," *Applied Optics*, vol. 42, no. 11, p. 1938, 2003.
- [4] T. Tahara, R. Mori, S. Kikunaga, Y. Arai, and Y. Takaki, "Dual-wavelength phase-shifting digital holography selectively extracting wavelength information from wavelength-multiplexed holograms," *Optics Express*, vol. 40, no. 12, pp. 2810–2813, 2015.
- [5] X. Li, Y. Wang, and Q. H. Wang, "Modified integral imaging reconstruction and encryption using an improved SR reconstruction algorithm," *Optics & Lasers in Engineering*, pp. 112–162, 2019.
- [6] X. Li, D. Xiao, and Q.-H. Wang, "Error-free holographic frames encryption with CA pixel-permutation encoding algorithm," *Optics and Lasers in Engineering*, vol. 100, pp. 200–207, 2018.
- [7] S. Jeon, J. Lee, J. Cho, S. Jang, Y. Kim, and N. Park, "Wavelength-multiplexed digital holography for quantitative phase measurement using quantum dot film," *Optics Express*, vol. 26, no. 21, p. 27305, 2018.
- [8] H. Cho, D. Kim, Y. Yu, W. Jung, and S. Shin, "Dual-wavelength Digital Holography Microscope for BGA Measurement Using Partial Coherence Sources," *Journal of the Optical Society of Korea*, vol. 15, no. 4, pp. 352–356, 2011.
- [9] J. Cho, J. Lim, S. Jeon et al., "Dual-wavelength off-axis digital holography using a single light-emitting diode," *Optics Express*, vol. 26, no. 2, pp. 2123–2131, 2018.
- [10] V. Bianco, P. Memmolo, and M. Leo, "Strategies for reducing speckle noise in digital holography," *Light Science & Applications*, p. 7, 2018.
- [11] Z. Gang, Z. Zhixiong, W. Huarui, and Y. Yan, "Near real-time digital holographic microscope based on GPU parallel computing," in *Proceedings of the SPIE- 2017 International Conference on Optical Instruments and Technology: Optical Systems and Modern Optoelectronic Instruments*, p. 10616, 2018.
- [12] Z. Zhao, "A holographic display method combining amplitude of real picture and phase of hologram," *Proc. SPIE*, vol. 10255, Article ID 1025503, 2017.
- [13] J. Kühn, J. Conchello, C. J. Cogswell et al., "Real-time dual-wavelength digital holographic microscopy for extended measurement range with enhanced axial resolution," *Biomedical Optics International Society for Optics and Photonics*, 2008.
- [14] Z. Gao, Z. Jiang, Y. Wang et al., "Phase imaging for photorefractive holographic gratings with dual-wavelength digital holography," in *Proceedings of the Photonics Asia*, p. 85561G, Beijing, China.
- [15] Y. Zeng, F. Wang, H. Lei, X. Hu, and X. Hu, "Surface profile measurement of microstructures based on dual-wavelength digital microscopic image-plane holography," *Guangxue Xuebao/Acta Optica Sinica*, vol. 33, no. 10, 2013.

- [16] C. J. Mann, P. R. Bingham, V. C. Paquit, and K. W. Tobin, "Quantitative phase imaging by three-wavelength digital holography," *Optics Express*, vol. 16, no. 13, pp. 9753–9764, 2008.
- [17] S. Peiyong, *3D Topography Recovery of Objects Based on Digital Holographic Technology*, Nanjing Normal University, 2011.
- [18] D. Parshall and M. K. Kim, "Digital holographic microscopy with dual-wavelength phase unwrapping," *Applied Optics*, vol. 45, no. 3, pp. 451–459, 2006.
- [19] A. Khmaladze, M. Kim, and C.-M. Lo, "Phase imaging of cells by simultaneous dual-wavelength reflection digital holography," *Optics Express*, vol. 16, no. 15, pp. 10900–10911, 2008.
- [20] Y. Kou, E. Li, J. Di, Y. Zhang, M. Li, and J. Zhao, "Surface morphology measurement of tiny object based on dual-wavelength digital holography," *Zhongguo Jiguang*, vol. 41, no. 2, 2014.
- [21] D. G. Abdelsalam and D. Kim, "Two-wavelength in-line phase-shifting interferometry based on polarizing separation for accurate surface profiling," *Applied Optics*, vol. 50, no. 33, pp. 6153–6161, 2011.
- [22] W. Yunxin, W. Dayong, Y. Yishu et al., "Application and Analysis in the Biomedicine Field Using Digital Holographic Technology," *Chinese Journal of Lasers*, vol. 41, no. 2, Article ID 002, 2014.
- [23] A. Khmaladze, E. Seeley, J. Jasensky et al., "Dual wavelength digital holographic imaging of cells with phase background subtraction," 2012.
- [24] D. G. Abdelsalam, R. Magnusson, and D. Kim, "Single-shot, dual-wavelength digital holography based on polarizing separation," *Applied Optics*, vol. 50, no. 19, pp. 3360–3368, 2011.
- [25] S. Grare, S. Coetmellec, D. Allano, G. Grehan, M. Brunel, and D. Lebrun, "Dual wavelength digital holography for 3D particle image velocimetry," *Journal of the European Optical Society: Rapid Publications*, vol. 10, no. 3, 2015.
- [26] Z. Yanan, L. Junshen, L. Yuan et al., "Three-Dimensional Displacement Tracking Technique of Particle Based on Digital Holographic Microscopy," *Chinese Journal of Lasers*, pp. 44–12, 2017.
- [27] B. Rappaz, P. Marquet, E. Cuche, Y. Emery, C. Depeursinge, and P. J. Magistretti, "Measurement of the integral refractive index and dynamic cell morphometry of living cells with digital holographic microscopy," *Optics Express*, vol. 13, no. 23, pp. 9361–9373, 2005.
- [28] D. Boss, P. T. So, E. Beaurepaire et al., "Dual-wavelength Digital Holography for quantification of cell volume and integral refractive index (RI)," in *Proceedings of the European Conferences on Biomedical Optics*, p. 808608, Munich, Germany.
- [29] M. Frómeta, G. Moreno, J. Ricardo et al., "Optimized setup for integral refractive index direct determination applying digital holographic microscopy by reflection and transmission," *Optics Communications*, vol. 387, pp. 252–256, 2017.
- [30] Z. Yanan, L. Hai, L. Yuan et al., "Compensation of the Phase Aberrations in Digital Holographic Microscopy Based on Reference Lens Method," *Acta Photonica Sinica*, vol. 47, no. 1, pp. 216–222, 2018.
- [31] Y. Lu, X. Wang, and X. Zhang, "Weighted least-squares phase unwrapping algorithm based on derivative variance correlation map," *Optik - International Journal for Light and Electron Optics*, vol. 118, no. 2, pp. 62–66, 2007.
- [32] S. Li, W. Chen, and X. Su, "Reliability-guided phase unwrapping in wavelet-transform profilometry," *Applied Optics*, vol. 47, no. 18, pp. 3369–3377, 2008.
- [33] Z. Wenjing, X. Qiangsheng, and Y. Yingjie, "Compensation for the Quadratic Phase Aberration in Off-axis Digital Microholography," *Acta Photonica Sinica*, vol. 38, no. 8, pp. 1972–1976, 2009.
- [34] Z. Wang, Y. Chen, and Z. Jiang, "Dual-wavelength digital holographic phase reconstruction based on a polarization-multiplexing configuration," *Chinese Optics Letters*, vol. 14, no. 1, pp. 31–35, 2016.
- [35] S. Liu, "Dynamic phase-contrast microscopy of living cells by digital holography," *Journal of Beijing University of Aeronautics & Astronautics*, vol. 38, no. 9, pp. 1186–1188, 2012.

## Research Article

# A Structured Light RGB-D Camera System for Accurate Depth Measurement

Van Luan Tran  <sup>1</sup> and Huei-Yung Lin <sup>1,2</sup>

<sup>1</sup>Department of Electrical Engineering, National Chung Cheng University, 168 University Rd., Chiayi 621, Taiwan

<sup>2</sup>Advanced Institute of Manufacturing with High-Tech Innovation, National Chung Cheng University, 168 University Rd., Chiayi 621, Taiwan

Correspondence should be addressed to Van Luan Tran; [tranvanluan07118@gmail.com](mailto:tranvanluan07118@gmail.com)

Received 9 July 2018; Revised 20 September 2018; Accepted 15 October 2018; Published 1 November 2018

Guest Editor: Wei Liu

Copyright © 2018 Van Luan Tran and Huei-Yung Lin. This is an open access article distributed under the Creative Commons Attribution License, which permits unrestricted use, distribution, and reproduction in any medium, provided the original work is properly cited.

The ability to reliably measure the depth of the object surface is very important in a range of high-value industries. With the development of 3D vision techniques, RGB-D cameras have been widely used to perform the 6D pose estimation of target objects for a robotic manipulator. Many applications require accurate shape measurements of the objects for 3D template matching. In this work, we develop an RGB-D camera based on the structured light technique with gray-code coding. The intrinsic and extrinsic parameters of the camera system are determined by a calibration process. 3D reconstruction of the object surface is based on the ray triangulation principle. We construct an RGB-D sensing system with an industrial camera and a digital light projector. In the experiments, real-world objects are used to test the feasibility of the proposed technique. The evaluation carried out using planar objects has demonstrated the accuracy of our RGB-D depth measurement system.

## 1. Introduction

In recent years, 3D imaging has received a great value in industrial and consumer applications. Machine vision systems developed with 3D imaging allow faster and more accurate measurement of components at manufacturing whereabouts. Nowadays, RGB-D cameras, such as Microsoft Kinect and Asus Xtion, are very popular due to the ability to provide the depth information directly. However, they have the limitation on accuracy and thus are not suitable for the applications that require accurate shape measurements [1–3]. As a result, the development of real-time RGB-D cameras still receives much attention from researchers and practitioners. The objective is to provide highly accurate RGB-D sensing techniques with more effective implementation approaches in terms of the density of acquired point clouds, time consumption, working environment, noise level, etc.

3D reconstruction based on the structured light technique has been investigated in the past few decades due to its popularity in the manufacturing applications. Structured light systems are suitable solutions for structured light

scanning, 3D reconstruction, and 3D sensing with accurate shape measurements [4, 5]. Structured light refers to the process of projecting predesigned known patterns on the scene and capturing the images to calculate the depth for 3D surface reconstruction. It is an important contribution to the development of 3D measurement systems. The patterns projected on the scene can be generated by a projector or other devices [6], and the relationship between the light source and the camera is a crucial factor. The accuracy of 3D reconstruction depends on the correctness of the calibration, which provides the relative pose between the camera and the light source projector.

In recent literature, several works presented the structured light systems for 3D reconstruction and proposed different approaches to deal with the related problems [7–10]. Scharstein *et al.* [11] proposed a method for acquiring high-complexity stereo image pairs with pixel-accurate correspondence information using structured light. Some previous works such as [12–15] described various methods to perform 3D reconstruction and obtained some satisfactory results. However, those techniques require to use precalibrated

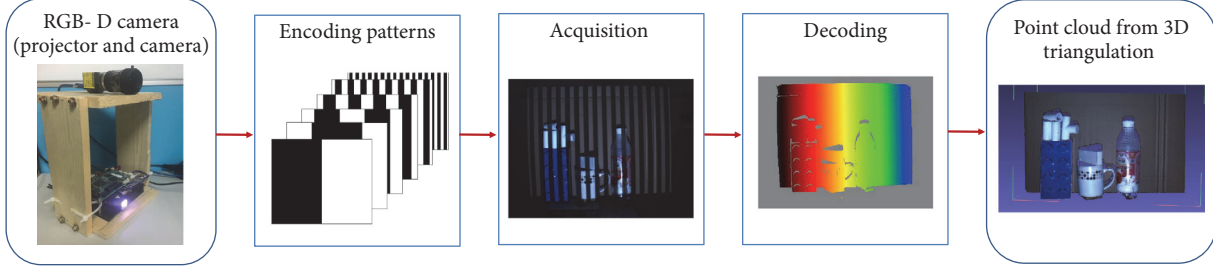


FIGURE 1: The overview of our RGB-D camera system with the structured light technique. The encoding pattern is a gray-code pattern. The acquisition is the images captured by the camera for each pattern in the sequence. The decoding is a coded map.

cameras to find the 3D world coordinates of the projected pattern. Thus, they highly depend on the accuracy of camera calibration and may transfer the error to the projector calibration. In [16], Huang and Tang described a method to perform fast 3D reconstruction using one-shot spatial structured light. Although the method can provide relatively accurate results, the evaluation and analysis were not carried out comprehensively. Some restrictions are also shown in their experiments when performing the tests on complex object surfaces. Cui and Dai [17] proposed a simple and efficient 3D reconstruction algorithm using structured light from 3D computer vision. However, their approach has some limitations on measuring inclined objects, and the 3D information cannot be recovered for the shadow areas.

In this work, we develop an RGB-D camera system based on the structured light technique. A system flowchart is shown in Figure 1. The encoding method is based on the gray-code coding [5], and the 3D reconstruction is achieved by the ray triangulation principle with the estimation of intersection points. The accuracy and density of the obtained point clouds are both high, and therefore it is suitable for the applications such as accurate shape measurements, 3D object recognition, and pose estimation for robotic manipulation.

This article is organized as follows: Section 2 presents a general overview of the structured light system and an accurate calibration method to derive the parameters of the camera-projector system. Section 3 contributes a method to create encoded patterns and decode the captured images from the camera and presents a ray triangulation principle for 3D computation by point intersection. Section 4 provides some experimental results, including the experimental setup, results with several different objects, and the evaluation of the accuracy of the object reconstruction. Finally, Section 5 gives the conclusion.

## 2. Background

**2.1. Structured Light Technique.** Currently, the development of structured light systems is in high demand. The structured light technique is based on the principle described in Figure 2. In general, the process of a structured light system can be divided into three basic steps:

- (i) **Encoding.** The encoding of the information into a sequence of patterns is performed in the temporal domain. A sequence of structured light patterns

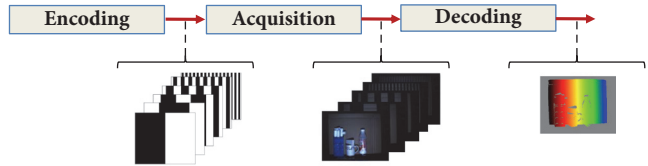


FIGURE 2: The overview of three basic steps in the process of a structured light system [1].

depends on the number of required patterns, parameters of the system, and the resolution of the projector and the camera.

- (ii) **Acquisition.** The sequence of patterns is projected on the scene by a data projector, and a camera is used to continuously capture the images.
- (iii) **Decoding.** The captured pattern-coded images are processed with the recognition of projected patterns to find the corresponding points associated with the projector and the camera.

In the implementation, there might be some additional steps depending on the solution of the system designer. It often follows a procedure to create range images, point clouds, or mesh models and possibly integrates several decoded coordinate maps, calibration, and triangulation principle. The calibration is to determine the intrinsic and extrinsic parameters of the camera and the projector, and the reconstruction is usually based on the ray triangulation principle by computing the intersection point.

**2.2. Calibration.** Calibration is an important issue which greatly affects the accuracy of the results [18]. In the proposed technique, firstly, we find the parameters of the system using the calibration method by Moreno and Taubin [6]. It is a simple and accurate method to calibrate the projector and camera systems. In this method, the projected corner locations are estimated with subpixel precision using local homographies to each corner in the images as illustrated in Figure 3. It includes three main steps as follows:

- (i) The camera calibration step to determine the intrinsic parameters of the camera. Camera calibration includes collecting a sequence of images of a planar

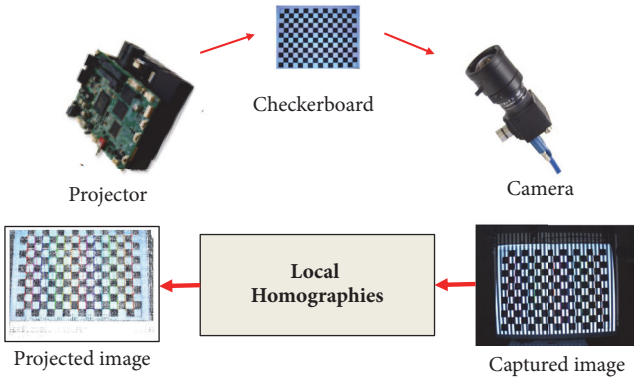


FIGURE 3: An illustration of the structured light system calibration. The captured image was selected in a set of the calibrated images, which are the projector project the patterns on the checkerboard and captured by the camera. The projected image is estimated with subpixel precision using local homographies to each corner in the captured images [1].

checkerboard pattern. The intrinsic camera calibration is derived by estimating the parameters using the perspective camera model [19]. We find the coordinates in the camera image plane for all of the checkerboard corners captured with different pattern orientations. We use OpenCV's `findChessboardCorners()` function [20] to automatically find the checkerboard corner locations. They are then refined to approach the subpixel accuracy. Finally, OpenCV's `calibrateCamera()` function is used to derive the calibrated camera parameters.

- (ii) The projector calibration step is to determine the intrinsic parameters of the projector. The mathematical model of our projector can be described the same as the camera. But the projector cannot capture the images from its viewpoint to find checkerboard corners. In this situation, we know a relation between the projector and image pixels extracted from the structured light sequences. Thus, we can estimate the checkerboard corner locations in the projector pixel coordinates based on a local homography [6] as an illustration in Figure 3.
- (iii) The stereo system calibration step is to derive the extrinsic parameters of the system, which consist of the rotation matrix and the translation vector. We use OpenCV's `stereoCalibrate()` function with the previously found checkerboard corner coordinates and their projections. The stereo parameters are a rotation matrix R and a translation vector T relating the projector-camera pair.

### 3. RGB-D Sensing Based Using Structured Light

**3.1. Encoding and Decoding Patterns.** The gray-code pattern [4] is a sequence of images with black and white stripes created for encoding the scene from the camera viewpoint.

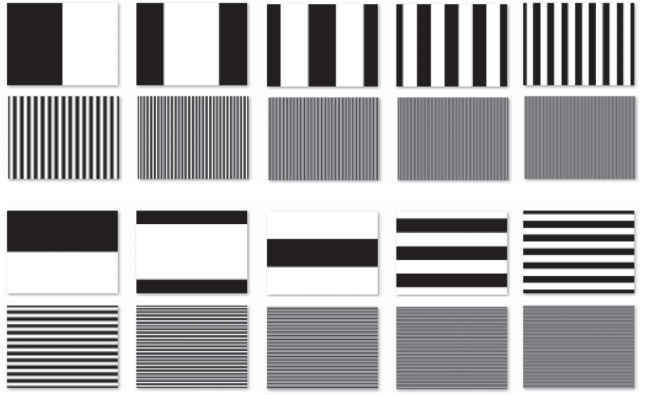


FIGURE 4: The gray-code patterns for the RGB-D camera used by the structure light technique [1].

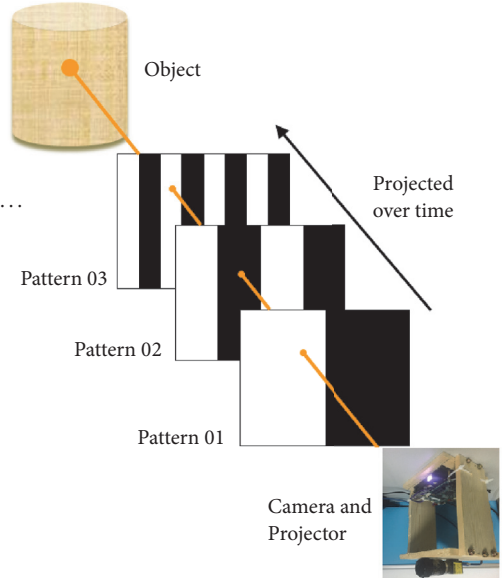


FIGURE 5: The acquisition of the projected patterns on an object. The gray-code pattern is projected by the projector and the scene is captured by the camera [1].

The pattern sequence has two types, one is the horizontal stripe and the other is the vertical stripe, as illustrated in Figure 4. All patterns are projected to a scene or an object as shown in Figure 5. The horizontal patterns consist of 10 pattern images which represent 10-bit values for each pixel. The first pattern is half black and half white, which represents the most significant bit, and the rest patterns are the images that switch between black and white in the columns. After combining all of the 10 horizontal patterns into one image, each column has the same 10 bits with the columns in the same image.

Structured light encoding depends on the resolution of the projector. The information is encoded into a sequence of patterns performed in the temporal domain. Commonly used approaches include gray-code coding and binary-code coding. Gray codes can be calculated by first computing the

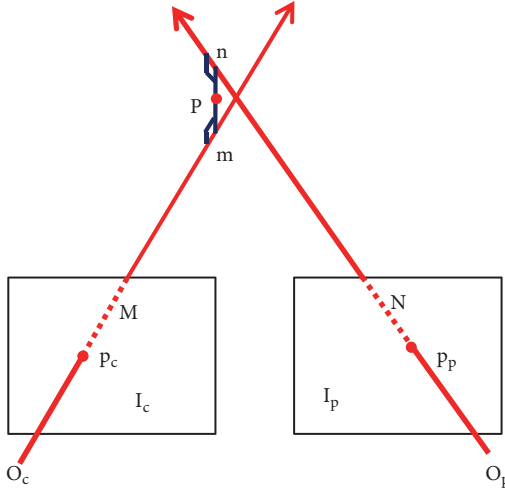


FIGURE 6: The intersection point of two rays from the pixels in the camera and projector coordinates [1].

binary representation of a number and then converting it using the following process: copy the most significant bit as it is, and replace the remaining bits (taking one bit at a time) with the result of an XOR operation of the current bit, with the previous bit of higher significance in the binary form.

For the binary-code coding, only two illumination levels are used and encoded as 0 and 1. The gray-code coding is an alternative to the binary representation, with only one bit change at a time between any two adjacent numbers. If there is an error reading on any changed bit, the value will never be off by more than one unit. In our system, we use a projector with the resolution of  $1024 \times 768$  and decode the pattern with 10 bits ( $2^{10} = 1024$  and  $2^{10} - \text{offset} = 768$ ), where the number of vertical patterns is  $\lceil \log(1024)/\log(2.0) \rceil = 10$  and the number of horizontal patterns is  $\lceil \log(768)/\log(2.0) \rceil = 10$ .

The camera captures the images of the projected patterns, and the coding step is to decode each pixel in the captured images into their corresponding decimal number presenting the column and row. It will be used to create a coded map as shown in Figure 1, which presents the corresponding point between the projector and the camera.

**3.2. 3D Reconstruction.** With a robust projector-camera calibration step, we define the location and orientation of the camera and projector with respect to the world coordinate frame. In the pattern encoding and decoding step, we determine one pixel in image  $I_c$  and its corresponding pixel in image  $I_p$ . Our reconstruction is based on the ray triangulation principle by the estimation of intersection points [4]. In order to compute the direction vector, two points in a ray are needed. The first point is the camera's center of projection, which is determined based on the extrinsic parameters of the structured light system. The second point is the point corresponding to the pixel from which the ray passes through. One ray passes through  $O_c$  and  $p_c$  of the left image ( $I_c$ ), and the other ray passes through  $O_p$  and  $p_p$  of the right image ( $I_p$ ), as shown in Figure 6. Here,  $O$  is the origin of the system and  $p$  is a pixel in the image. The 3D point cloud is obtained from

the intersection point  $P$ , which is a midpoint of the shortest segment between the rays.

To estimate the intersection point, we consider two rays  $M$  and  $N$  in 3D space passing through points  $p_c$  and  $p_p$  with direction vectors  $\vec{x}$  and  $\vec{y}$ , respectively. Let the two closest points on the lines be  $m$  and  $n$ , as defined in (1) and (2), where  $g$  and  $k$  are scalar values.

$$m = p_c + g\vec{x} \quad (1)$$

$$n = p_p + k\vec{y} \quad (2)$$

The  $mn$  segment connecting rays  $M$  and  $N$  is perpendicular to the rays, and therefore the dot product of the vectors is equal to 0 as follows:

$$(m - n) \cdot \vec{x} = 0 \quad (3)$$

$$(m - n) \cdot \vec{y} = 0 \quad (4)$$

With (1) and (2), (3) and (4) are represented by

$$\vec{r} \cdot \vec{x} + g\vec{x} \cdot \vec{x} - k\vec{y} \cdot \vec{x} = 0 \quad (5)$$

$$\vec{r} \cdot \vec{y} + g\vec{y} \cdot \vec{x} - k\vec{y} \cdot \vec{y} = 0 \quad (6)$$

where

$$\vec{r} = p_c - p_p \quad (7)$$

From (5) and (6), the scalar values are calculated by

$$g = \frac{(\vec{r} \cdot \vec{x})(\vec{y} \cdot \vec{y}) - (\vec{y} \cdot \vec{x})(\vec{r} \cdot \vec{y})}{(\vec{y} \cdot \vec{x})(\vec{y} \cdot \vec{x}) - (\vec{y} \cdot \vec{y})(\vec{x} \cdot \vec{x})} \quad (8)$$

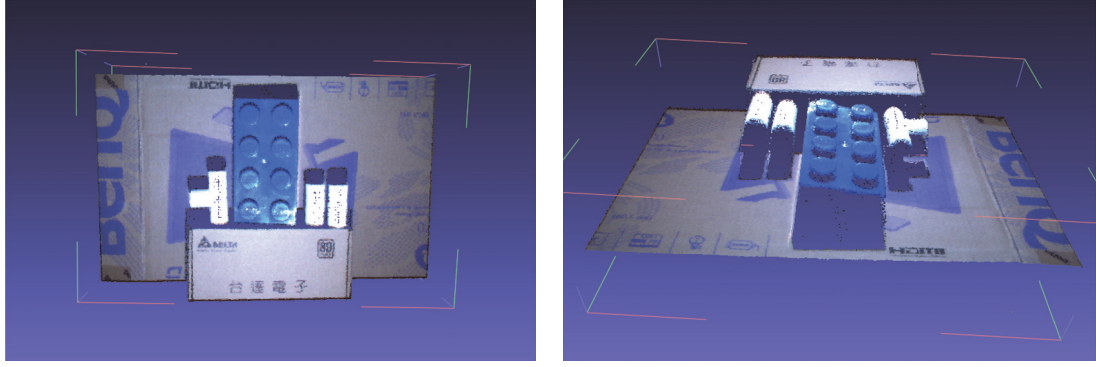
$$k = \frac{(\vec{y} \cdot \vec{x})(\vec{r} \cdot \vec{x}) - (\vec{x} \cdot \vec{x})(\vec{r} \cdot \vec{y})}{(\vec{y} \cdot \vec{x})(\vec{y} \cdot \vec{x}) - (\vec{y} \cdot \vec{y})(\vec{x} \cdot \vec{x})} \quad (9)$$

The midpoint of the shortest segment are then estimated by

$$P = \frac{p_c + g\vec{x} + p_p + k\vec{y}}{2} \quad (10)$$

## 4. Experiments

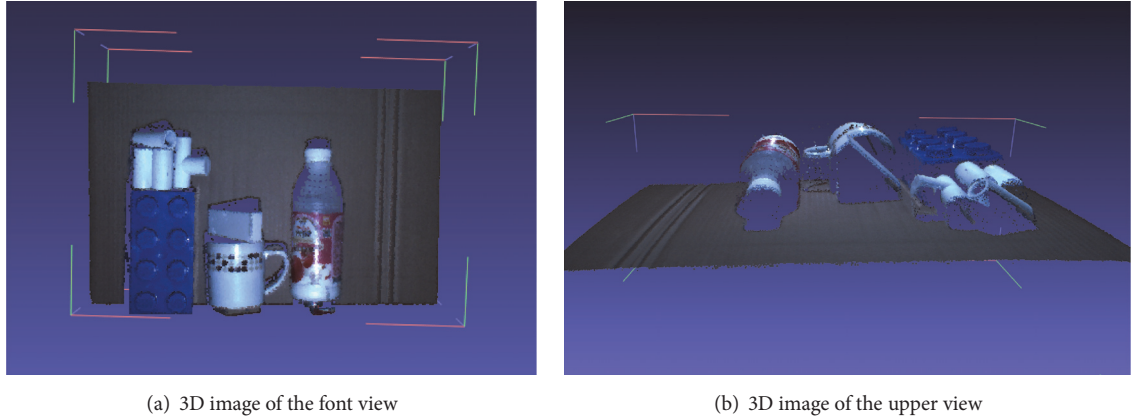
In the structured light system, the quality of the captured images is important for obtaining a good pattern database to perform the calibration, decoding, and reconstruction. Hence, the resolution of the camera is usually higher than the resolution of the projector. Then, the projection field of view is adjusted inside the field of view of the camera. In the experiments, we use a Flea3 FL3-U3-32S2C from Point Grey Research with the image resolution of  $2080 \times 1552$ . The digital light projector is a DLP Light Crafter 4500 projector from Texas Instrument with the resolution of  $1024 \times 678$ . Their focus length, resolution, zoom, and direction were selected prior to calibration accordingly to the target of the system. All devices are connected to a host computer. After the system is calibrated, part of the system cannot be moved. We have to



(a) 3D image of the font view

(b) 3D image of the upper view

FIGURE 7: 3D reconstruction result with some objects (a lego box, three plastic pipes, and a big box), these objects are low reflecting light.



(a) 3D image of the font view

(b) 3D image of the upper view

FIGURE 8: 3D reconstruction result with multiple objects (a cup, bottle, small box, lego box, and some plastic pipes), the bottle and cup are with high reflecting light.

keep the distance and orientation between the projector and the cameras intact; otherwise it will be essential to perform a recalibration.

The settings of the camera and projector should be adapted according to the lighting in the scene. Other lighting sources projected directly in the scene should be rejected. If not, the calibrated and reconstructed results will be affected. The system was calibrated with 12 sets of acquired projected checkerboard patterns. An acquisition set includes the images captured by the camera for each pattern in the sequence. After the system is calibrated as exposed in Section 2.2, the calibration result is stored in a .yml file.

For reconstruction, our system includes three main steps. Firstly, our system loads the calibration parameters and projects one acquisition set of patterns on objects. Secondly, decoding the captured pattern-coded images provides a coded map to store the corresponding points between the projector and the camera. Finally, with calibrated parameters and the coded map, we apply the ray triangulation principle to get the 3D point that will be rendered simultaneously with one color image to create an XYZRGB point cloud. In Figures 7 and 8, we present the 3D reconstruction results of several objects. The results successfully measure objects with reflecting light for some of the projected colors. After

performing the reconstruction, the 3D information of the reconstructed objects is saved in a .txt file.

The evaluation of the proposed technique is performed by measuring the dimension of a reconstructed checkerboard pattern and its corner points. The checkerboard has the dimension of  $399 \times 285 \text{ mm}^2$  and each small square has the size of  $28.5 \times 28.5 \text{ mm}^2$  as demonstrated in Figure 9. After performing the 3D reconstruction for this checkerboard, we can use 3ds Max Design or Meshlab software to examine, as shown in Figure 10. A distance measurement tool is used to measure the dimension of the checkerboard. The accuracy is presented in Table 1, with the errors of the corner points. This table reports that our system can measure the objects with high accuracy. Compared with the algorithms proposed by Moreno *et al.* [6] with Max. error of 0.8546(%). They use a method to estimate the image coordinates of 3D points in the projector image plane and perform the calibration on both projector and camera. With Max. error of 0.1240(%), our proposed method provides the better 3D reconstruction results.

## 5. Conclusion

In this work, we have developed an RGB-D camera system based on the structured light technique. It contains a camera

TABLE 1: Measuring the accuracy of a reconstructed checkerboard (CB) as shown in Figure 10.

Name	Real CB (mm)	Reconstructed CB (mm)	Error (%)
Width of top checkerboard (AB)	399.000	399.382	0.0957
Width of bottom checkerboard (CD)	399.000	399.495	0.1240
Height of left checkerboard (AC)	285.000	284.746	0.0891
Height of right checkerboard (BD)	285.000	285.298	0.1045
Max. error			0.1240

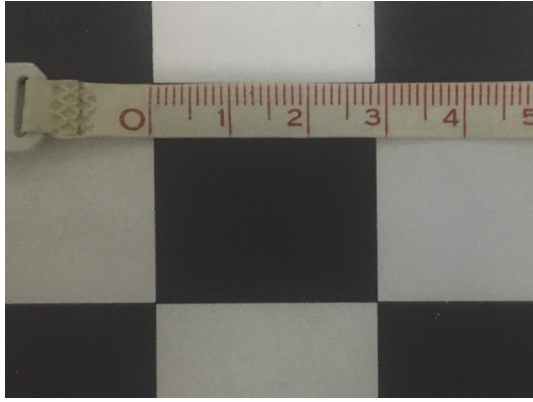
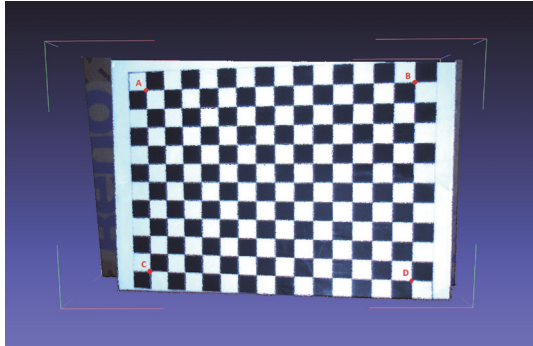
FIGURE 9: The real dimension of each small square has the size of  $28.5 \times 28.5 \text{ mm}^2$  in the checkerboard reconstructed as shown in Figure 10.

FIGURE 10: The 3D reconstruction of a checkerboard shown with Meshlab software. We used a measuring tool of the Meshlab to measure it.

and a projector to perform accurate shape measurements with high-density point cloud outputs. 3D reconstruction with multiple objects and performance evaluation of the system are carried out in the real-world environment. Our method has high accuracy as presented in the experimental results. In the experiment, we tested the system with different objects to check the surface of reconstruction and accuracy evaluation. The results have demonstrated that the proposed technique is feasible for dense 3D measurement applications.

## Data Availability

The data used to support the findings of this study are available from the corresponding author upon request

(<https://github.com/luantran07/data-for-a-structured-light-rgb-d-camera-system>).

## Disclosure

This publication is an extended version of 2017 International Conference on System Science and Engineering (ICSSE) [1].

## Conflicts of Interest

The authors declare that they have no conflicts of interest.

## Acknowledgments

The support of this work in part by the Ministry of Science and Technology of Taiwan under Grant MOST 104-2221-E-194-058-MY2 is gratefully acknowledged.

## References

- [1] V.-L. Tran and H.-Y. Lin, “Accurate RGB-D camera based on structured light techniques,” in *Proceedings of the 2017 International Conference on System Science and Engineering, ICSSE 2017*, pp. 235–238, Viet Nam, July 2017.
- [2] O. Wasenmüller and D. Stricker, “Comparison of Kinect V1 and V2 Depth Images in Terms of Accuracy and Precision,” in *Computer Vision – ACCV 2016 Workshops*, vol. 10117 of *Lecture Notes in Computer Science*, pp. 34–45, Springer International Publishing, Cham, 2017.
- [3] J. Smisek, M. Jancosek, and T. Pajdla, “3D with Kinect,” in *Proceedings of the 2011 IEEE International Conference on Computer Vision Workshops (ICCV ’11)*, pp. 1154–1160, IEEE, Barcelona, Spain, November 2011.
- [4] Q. Gu, K. Herakleous, and C. Poullis, “3DUNDERWORLD-SLS: An open-source structured-light scanning system for rapid geometry acquisition,” *Computer Vision and Pattern Recognition*, 2016.
- [5] D. Moreno, W. Y. Hwang, and G. Taubin, “Rapid Hand Shape Reconstruction with Chebyshev Phase Shifting,” in *Proceedings of the 2016 Fourth International Conference on 3D Vision (3DV)*, pp. 157–165, Stanford, CA, USA, October 2016.
- [6] D. Moreno and G. Taubin, “Simple, accurate, and robust projector-camera calibration,” in *Proceedings of the 2nd Joint 3DIM/3DPVT Conference: 3D Imaging, Modeling, Processing, Visualization and Transmission, 3DIMPVT 2012*, pp. 464–471, Switzerland, October 2012.
- [7] C.-Y. Chen, P.-S. Huang, S.-W. Huang, J.-H. Zhang, and B. R. Chang, “Structured light 3D face scanning system,” in *Proceedings of the 2nd IEEE International Conference on Consumer Electronics - Taiwan, ICCE-TW 2015*, pp. 344–345, Taiwan, June 2015.

- [8] M. Massot-Campos, G. Oliver-Codina, H. Kemal, Y. Petillot, and F. Bonin-Font, "Structured light and stereo vision for underwater 3D reconstruction," in *Proceedings of the MTS/IEEE OCEANS 2015 - Genova*, Italy, May 2015.
- [9] M. Piccirilli, G. Doretto, A. Ross, and D. Adjeroh, "A Mobile Structured Light System for 3D Face Acquisition," *IEEE Sensors Journal*, vol. 16, no. 7, pp. 1854-1855, 2016.
- [10] D. Lanman, *Grey code patterns for 3D reconstruction by structure light technique*, AIT Computer Vision Wiki, Brown University, 2014.
- [11] D. Scharstein and R. Szeliski, "High-accuracy stereo depth maps using structured light," in *Proceedings of the 2003 IEEE Computer Society Conference on Computer Vision and Pattern Recognition*, p. I/202, USA, June 2003.
- [12] J. Wang, C. Zhang, W. Zhu, Z. Zhang, Z. Xiong, and P. A. Chou, "3D scene reconstruction by multiple structured-light based commodity depth cameras," in *Proceedings of the 2012 IEEE International Conference on Acoustics, Speech, and Signal Processing, ICASSP 2012*, pp. 5429–5432, Japan, March 2012.
- [13] C. Bourgeois-Republique, A. Dipanda, and A. Koch, "A Structured Light System Encoding for an Uncalibrated 3D Reconstruction Based on Evolutionary Algorithms," in *Proceedings of the 2013 International Conference on Signal-Image Technology & Internet-Based Systems (SITIS)*, pp. 124–129, Kyoto, Japan, December 2013.
- [14] S. Huang, L. Xie, Z. Wang, Z. Zhang, F. Gao, and X. Jiang, "Accurate projector calibration method by using an optical coaxial camera," *Applied Optics*, vol. 54, no. 4, pp. 789–795, 2015.
- [15] K. Herakleous and C. Poullis, "Stripe boundary codes for real-time structured-light range scanning of moving objects," in *Proceedings of the Eighth IEEE International Conference on Computer Vision*, vol. 2, pp. 359–366, Vancouver, Canada.
- [16] B. Huang and Y. Tang, "Fast 3D reconstruction using one-shot spatial structured light," in *Proceedings of the 2014 IEEE International Conference on Systems, Man, and Cybernetics, SMC 2014*, pp. 531–536, USA, October 2014.
- [17] H. Cui, N. Dai, W. Liao, and X. Cheng, "An accurate reconstruction model using structured light of 3-D computer vision," in *Proceedings of the 7th World Congress on Intelligent Control and Automation, WCICA'08*, pp. 5095–5099, China, June 2008.
- [18] M. Fu, Y. Leng, and H. Zhang, "A calibration method for structured light systems based on a virtual camera," in *Proceedings of the 8th International Congress on Image and Signal Processing, CISIP 2015*, pp. 57–63, China, October 2015.
- [19] S. Zhang and P. S. Huang, "Novel method for structured light system calibration," *Optical Engineering*, vol. 45, no. 8, Article ID 083 601083 6018, 2006.
- [20] G. Bradski, "The OpenCV Library," *Dr Dobbs Journal of Software Tools*, 2000.

## Research Article

# Measuring the Phase of an Optical Field from Two Intensity Measurements: Analysis of a Simple Theoretical Model

Damien P. Kelly 

Oryx Optics Ltd, 19 The Elms, Athlone, Co. Westmeath, Ireland

Correspondence should be addressed to Damien P. Kelly; [damienspkelly@gmail.com](mailto:damienspkelly@gmail.com)

Received 21 June 2018; Accepted 16 September 2018; Published 1 October 2018

Guest Editor: Wei Liu

Copyright © 2018 Damien P. Kelly. This is an open access article distributed under the Creative Commons Attribution License, which permits unrestricted use, distribution, and reproduction in any medium, provided the original work is properly cited.

Under the scalar paraxial approximation, an optical wavefield is considered to be complex function dependent on position; i.e., at a given location in space the optical field is a complex value with an intensity and phase. The optical wavefield propagates through space and can be modeled using the Fresnel transform. Lenses, apertures, and other optical elements can be used to control and manipulate the wavefield and to perform different types of signal processing operations. Often these optical systems are described theoretically in terms of linear systems theory leading to a commonly used Fourier optics framework. This is the theoretical framework that we will assume in this manuscript. The problem which we consider is how to recover the phase of an optical wavefield over a plane in space. While today it is relatively straightforward to measure the intensity of the optical wavefield over a plane using CMOS or CCD sensors, recovering the phase information is more complicated. Here we specifically examine a variant of the problem of phase retrieval using two intensity measurements. The intensity of the optical wavefield is recorded in both the image plane and the Fourier plane. To make the analysis simpler, we make a series of important theoretical assumptions and describe how in principle the phase information can be recovered. Then, a deterministic but iterative algorithm is derived and we examine the characteristics and properties of this algorithm. Finally, we examine some of the theoretical assumptions we have made and how valid these assumptions are in practice. We then conclude with a brief discussion of the results.

## 1. Introduction

Visible light is an electromagnetic field with a wavelength that ranges roughly from ultraviolet (300 nm) to infrared (800 nm). An electromagnetic field is vectorial in nature with three electric and magnetic orthogonal field components. When designing a microwave radio receiver (long wave wavelengths relative to visible light) one must consider how these different magnetic and electric field components interact with each other and with conducting strips of metal and dielectric substrates that are used for impedance matching, mixing, and waveguiding. The resulting equations (that follow from Maxwell's equations) are quite complex and require intensive numerical calculation procedures since the different vectorial components of the EM field interact with each other forming coupled vectorial equations [1].

Fortunately when examining optical problems in the visible regime it is often possible to make the scalar approximation. This means that we can assume that the different

vectorial components of the optical wavefield do not “see” each other and hence each vectorial component can be treated independently as a separate scalar problem. This approximation is very useful and quite accurate and can be used to analyze a wide range of important and practical optical problems.

Therefore in this manuscript we assume that a scalar description of light propagation is valid and use the Fresnel transform to relate an optical field in one plane to that in another plane, where the optical planes are separated from each other by an axial distance  $z$ . The light sources used are assumed to be of a definite monochromatic temporal frequency and are both temporally and spatially coherent [2, 3]. Optical elements used to shape the form of the illuminating wavefield are assumed to be “thin” and operate on an incident optical field, multiplying it by a function describing the optical element over a plane [4]. The assumptions we have described place us in a Fourier optics framework [4]. Fourier optics is an important branch of optical theory since it allows

the development of relatively simple and intuitive models of optical systems. These models provide significant insight into the characteristics of the underlying optical systems and are also reasonably accurate. Furthermore Fourier optics builds important bridges between disciplines in particular allowing optical systems to be interpreted in terms of signal processing operations that are commonly used in electrical engineering, communication theory, and control engineering [4–9]. This type of viewpoint can be extended still further with the development of mixed space/time transforms or mixed space/spatial frequency transforms such as the fractional Fourier transform [10], the Linear Canonical Transform (LCT), and perhaps even more generally the form of Wigner distribution functions [11–17].

We note that in this theoretical framework if we know the intensity and phase of the optical field in a give optical plane, it is then possible to calculate (numerically or under certain circumstances analytically) the field distribution in any other plane using the LCT [18, 19] and hence we can image over a 3D volume, with varying levels of spatial resolution [19].

In a practical sense then it is important to be able to measure experimentally both the intensity and the phase of an optical wavefield in a given plane. Nowadays high quality low noise CCD and CMOS sensors are commercially available and widely used. With these devices it is relatively straightforward to measure the intensity of an optical field in a particular plane. We will now briefly discuss several techniques for indirectly measuring the phase distribution of the field.

**1.1. Digital Holography.** Digital holography (DH) was first proposed by Gabor himself in [20–22] and the first experimental implementation was done by Goodman et al. in [23]; later pioneering work was done by Yaroslawski, [24], Onural and Scott [25], and Schnars and Jüptner [26]. More recent theoretical and experimental analysis of these systems is given [19, 27–36]. In holography we need both an object wave and a so-called reference wave. Light from the laser source in the optical setup is divided by a beam splitter into a reference and illuminating plane waves. The illuminating plane wave is directed by a mirror so that it illuminates the object we wish to examine. The wavefront interacts with a “thin” object and the resulting object wavefield scatters and propagates a distance  $z$  to the CCD/CMOS plane. Meanwhile the reference wave is directed through the optical system where it is recombined with the object wave at a second beam splitter. Thus at the sensor plane we record the interference between the reference and object wavefields thereby recording a hologram. A drawback of this approach is that the additional optics parts are required; a clean stable reference beam is essential; and several undesired “noise” terms, two DC terms and a twin image term, are produced by the recording process. These terms can be removed by capturing several phase shifted intensity images and performing some postprocessing operations. Single shot off-axis holography with a tilted plane reference wave is possible; however the spatial resolution of the resulting real image term (object wavefield) is significantly reduced. The accuracy and limitations of this approach have already been examined in several publications; see, for example, [33, 37].

**1.2. Transport of Intensity.** These approaches are quite different in nature and require the capture of two separate intensity distributions. Usually these distributions are captured in an image plane and in a slightly defocused plane. Using the so-called transport of intensity equation, see, for example, [38, 39], it is possible to recover an estimate for the phase distribution. There are several interesting aspects of the reconstruction of the phase; firstly the reconstructed phase is not wrapped over  $2\pi$  and secondly with some reconstruction approaches, namely, an FFT based approach to indefinite integration, see [40], low frequencies can be more difficult to recover.

**1.3. Iterative Phase Retrieval.** Finally we turn our attention to iterative phase retrieval approaches. Here usually two or more intensity distributions are captured in different LCT domains, or in physical optics terms the intensity is captured in several different optical planes. Often these different optical planes are separated from each other by sections of free-space and combinations of lenses, but also in the image and corresponding Fourier transform planes. The origin of these types of algorithms dates back to the iterative Gerschberg-Saxton (GS) approach first published in the 70s and was further developed Fienup et al. [41, 42]. The initial algorithms assumed that two measurements were made and the intensity distribution was recorded in the image plane and in the Fourier plane. Later algorithms extended these approaches to work with multiple different Fresnel domains [43–47].

The image-Fourier plane (GS) algorithm works as follows:

- (1) One starts with an initial guess of the phase distribution in the image plane
- (2) We then numerically calculate the Fourier transform of this distribution and compare the calculated intensity in the Fourier plane to the experimentally measured result. The calculated intensity distribution will differ from the experimentally measured distribution because our initial guess at the phase distribution will not be correct
- (3) At this stage we replace the incorrect numerically calculated intensity distribution with the correct experimentally measured intensity, while retaining the phase values and numerically propagate the distribution back to the image plane
- (4) We do not expect the calculated image intensity to be the same as the measured intensity distribution. Again we replace the numerically calculated distribution with the measured distribution
- (5) Steps (2)-(4) are repeated until the algorithm converges, i.e., when there is little difference between the measured and calculated intensity distributions. The similarity between the measured and numerically calculated distributions can be estimated with a root mean square error measure [46].

In [41], Fienup directly compares the behavior of this algorithm to gradient descent optimization approaches. The behavior and properties of these algorithms have been of significant interest in the field. It is generally said that for phase

retrieval to work effectively one needs to have a good estimate of the initial phase. When that is the case the algorithms tend to converge to the nearest local minimum which in this case would be one of the global minimums. And hence the algorithm will return the real-physical phase distribution and not a solution that merely satisfies the numerical constraints of the problem but which has no physical meaning. In this manuscript we will explore this question of multiple phase solutions more closely, by examining a simplified version of the phase retrieval problem. A major outstanding issue with these iterative approaches is that algorithm often stagnates in a local minimum yielding a poor estimate for the phase. There is also the possibility that there are several different solutions to this ill-posed problem, at least in the 1D case [48].

In the iterative phase retrieval approach that we have just been discussing the intensity distributions are captured using CCD/CMOS arrays. And so in practice the intensity distribution is only recorded over a finite spatial extent and with a finite number of pixels which limits the spatial resolution and also introduces numerical sampling effects [37, 49]. The numerical procedures that are then used with these 2D arrays of intensity values tend to rely on fast Fourier transform (FFT) based algorithms for their implementation. This requires developing the software and numerical techniques for implementing these algorithms so that they are sufficiently fast and so that other sampling rules and numerical issues can be addressed [49]. This development, while necessary, tends to concentrate attention on the software implementation rather than on other physical and mathematical modeling aspects of the problem.

Therefore in this manuscript we deliberately take a different approach that emphasizes a theoretical analysis using a relatively simple model. Similar to the iterative phase retrieval approach we analyze how the phase may be estimated from two intensity measurements: one made in the image plane and one made in the Fourier plane. We do however make an important simplification. We assume that we can measure the intensity distribution in the Fourier plane over an infinite extent and ignore any sampling or discretization process that occurs due to the finite extent of the pixels in the CCD/CMOS array. Furthermore we assume that the intensity distribution in the image plane consists of a finite set of discrete point sources. With these two simplifications we can derive an analytical solution to the phase retrieval problem.

The manuscript is organized in the following manner: In Section 2, we show, under assumptions, which we have outlined in the text above and which are detailed in Section 2, how the phase values can in principle be determined using an analytical solution. To recover the phase values we must use an iterative procedure which has a finite but large number of steps. In Section 3, we examine an algorithm for implementing the iterative strategy derived in Section 2 and examine how the number of operations depends on the number of contributing point sources in the image plane. We show that there are multiple solutions to the phase retrieval problem. We then examine approaches for reducing the number of possible solutions. In Section 4, we finish with a brief discussion of the presented analysis and highlight some practical

difficulties when extending the theoretical model to realistic real-world phase measurements.

## 2. Analysis of an Idealized Experiment

We begin our analysis by examining the idealized optical system depicted in Figure 1. There is a set of  $N$  distinct point sources, each with a known intensity value and hence a known magnitude,  $a_n$ , where  $a_n$  is the magnitude of point source  $n$ . The phase value,  $\phi_n$ , associated with each point source however remains the unknown physical parameter that we wish to measure. So to reiterate, the problem as depicted in Figure 1 is that we are given a set of  $N$  point sources with known amplitudes and unknown phase values. We further assume that these points sources are uniformly spaced a distance  $\Delta$  from each other. We are also given a second measurement, the intensity distribution in the Fourier plane. What we have just described is very similar to the practical iterative phase retrieval experiment described in the Introduction. In a real experiment however these intensity distributions are recorded by CCD/CMOS arrays which have a finite extent, a finite number of pixels, and which sample of the intensity distribution they measure. These are critical factors when considering the performance limitations of these systems; see [33, 36]. They also complicate the theoretical analysis and so now we neglect these factors so that we can develop a simpler theoretical description of the phase retrieval problem.

We imagine that we can measure the intensity in the Fourier domain over an infinite extent and with a sampling step size that is extremely small, so that any sampling effects can be ignored. We also imagine that only a finite number of perfect point sources in the input plane (with known intensity but unknown phase) contribute to the Fourier plane intensity distribution. Hence in this analysis we exclude any physical imposed limiting factors on the ability of our system to make a measurement. This will allow us to significantly simplify the analysis and to concentrate on another and arguable more important effect: the existence of a very high number of alternative solutions to the phase retrieval problem. As we shall see it is possible that many different combinations of phase values can produce identical intensity distributions. Hence this phase retrieval problem is said to be ill-posed.

We refer back to Figure 1, where we have indicated that the contributing point sources are Fourier-transformed by an optical Fourier transform system. This type of optical system is well known; see, for example, [4]. The distribution in the Fourier plane is scaled by both the wavelength,  $\lambda$ , of the light source and the focal length of the lens. It is convenient for our purposes here to set  $\lambda f = 1$  so that we can analyze an unscaled Fourier distribution. Here this distribution is incident on an ideal recording material, allowing us to record the continuous intensity distribution. Then we perform a second unscaled inverse Fourier transform on this intensity distribution numerically. We note however that although we perform two successive Fourier operations (a forward and inverse transform), we do not arrive back at the input plane distribution since we perform the second Fourier transform

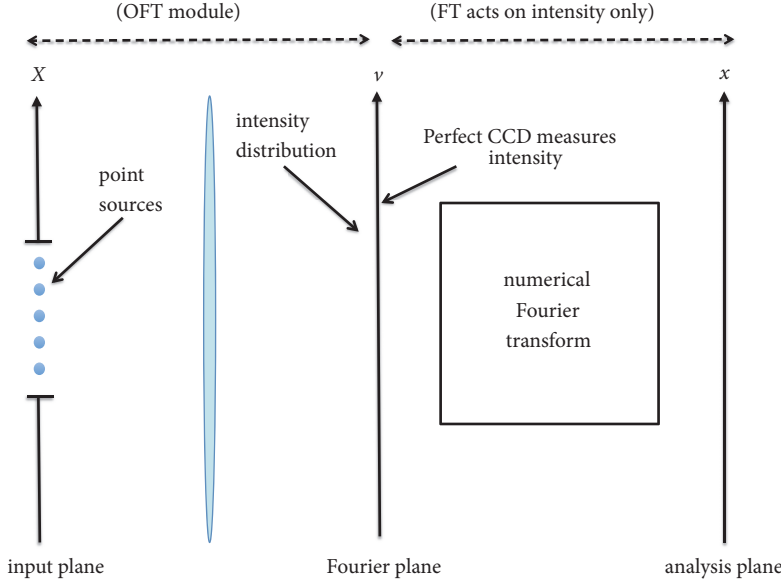


FIGURE 1: Depiction of phase retrieval setup for an idealized phase retrieval experiment, OFT: optical Fourier transform. A set of  $N$  point sources with known amplitude and unknown phase are present in the input plane. This distribution is Fourier-transformed by the lens and the intensity of the resulting distribution in the Fourier plane is recorded. We assume that we can measure this intensity distribution over an infinite extent and with extremely high spatial resolution so that we can ignore the numerical effects of sampling due to the CCD/CMOS pixels. We show how this intensity distribution is processed using a second Fourier transform, this time calculated numerically, and we examine its properties in the “analysis plane” (as depicted above). We show how to determine the phase values of the  $N$  point sources in the input plane.

operation on the intensity of the Fourier distribution not on its complex amplitude, as in a 4-f imaging system [50].

We thus begin by noting that the Fourier transform of a point source is given by

$$\begin{aligned} FT \{ \delta(x + X_n) a_n \exp(j\phi_n) \} (\nu) \\ = \exp(-j2\pi X_n \nu) a_n \exp(j\phi_n), \end{aligned} \quad (1)$$

where  $X_n$  is the spatial location of point source “ $n$ ” while the parameters  $a_n$  and  $\phi_n$  refer to its phase and amplitude respectively. Hence for a sum of  $N$  distinct point sources we can write

$$\begin{aligned} FT \left\{ \sum_{n=1}^N \delta(x - X_n) a_n \exp(j\phi_n) \right\} (\nu) \\ = \sum_{n=1}^N \exp(-j2\pi X_n \nu) a_n \exp(j\phi_n). \end{aligned} \quad (2)$$

We are however interested in the intensity distribution of the field in the Fourier plane. We remember that the intensity of a complex number is given by that number times its complex conjugate. With this relationship in mind we now write the conjugate expression for (2)

$$\begin{aligned} FT \left\{ \sum_{n=1}^N \delta(x - X_n) a_n \exp(j\phi_n) \right\}^* (\nu) \\ = \sum_{n=1}^N \exp(j2\pi X_n \nu) a_n \exp(-j\phi_n), \end{aligned} \quad (3)$$

where “ $*$ ” refers to a complex conjugate operation. We can now write an analytical expression for the intensity distribution in the Fourier plane which when simplified can be written in the following form

$$\begin{aligned} I_{FT}(\nu) \\ = \sum_{n=1}^N a_n^2 \\ + 2 \sum_{n=1}^{N-1} \sum_{m=1}^{N-n} a_m a_{m+n} \{ \cos[2\pi(n\Delta)\nu + \phi_m - \phi_{m+n}] \}. \end{aligned} \quad (4)$$

From (4) we can see that we have a sum of cosines. For each given value of  $n$  there is a specific spatial frequency component  $f_s = n\Delta$ , and there are  $N - 1$  terms. It is easier to analyze this double summation by initially concentrating on a single spatial frequency component, i.e., for a specific value of  $n$ , and we refer to such a component as  $I_{FT}^n(\nu)$ . Noting the following trigonometric relationship,  $\cos(A+B) = \cos(A)\cos(B) - \sin(A)\sin(B)$ , we can express  $I_{FT}^n(\nu)$  as

$$I_{FT}^n(\nu) = \sum_{n=1}^N a_n^2 + \sum_{n=1}^{N-1} I_{FT}^n(\nu), \quad (5)$$

where

$$\begin{aligned} I_{FT}^n(\nu) &= 2 \sum_{m=1}^{N-n} a_m a_{m+n} \cos[2\pi n\Delta\nu + (\phi_m - \phi_{m+n})] \\ &= 2 \cos(2\pi n\Delta\nu) \sum_{m=1}^{N-n} a_m a_{m+n} \cos(\phi_m - \phi_{m+n}) \\ &\quad + 2 \sin(2\pi n\Delta\nu) \sum_{m=1}^{N-n} a_m a_{m+n} \sin(\phi_m - \phi_{m+n}). \end{aligned} \quad (6)$$

We now consider the inverse Fourier transform of  $I_{\text{FT}}^n(\nu)$ , which we specifically define as

$$\overline{M}_n(x) = \int_{-\infty}^{\infty} I_{\text{FT}}^n(\nu) \exp(+j2\pi x\nu) d\nu, \quad (7)$$

which is now in a spatial domain once again, specifically the “analysis” plane in Figure 1. Noting that

$$\text{FT}\{\sin(2\pi k_0 x)\}(k) = \frac{j}{2} [\delta(k+k_0) - \delta(k-k_0)], \quad (8)$$

$$\text{FT}\{\cos(2\pi k_0 x)\}(k) = \frac{1}{2} [\delta(k+k_0) + \delta(k-k_0)],$$

then

$$\begin{aligned} \overline{M}_n(x) &= \delta(x+n\Delta) \left\{ \sum_{m=1}^{N-n} a_m a_{m+n} \cos(\phi_m - \phi_{m+n}) \right. \\ &\quad \left. - j \sum_{m=1}^{N-n} a_m a_{m+n} \sin(\phi_m - \phi_{m+n}) \right\} + \delta(x-n\Delta) \\ &\quad \cdot \left\{ \sum_{m=1}^{N-n} a_m a_{m+n} \cos(\phi_m - \phi_{m+n}) \right. \\ &\quad \left. + j \sum_{m=1}^{N-n} a_m a_{m+n} \sin(\phi_m - \phi_{m+n}) \right\}. \end{aligned} \quad (9)$$

We see from (9) that the complex numbers (arising from the summation of sines and cosines) multiplying the  $\delta(x-n\Delta)$  and  $\delta(x+n\Delta)$  components are complex conjugates of each other. Hence we see that

$$\text{Re}\{\overline{M}_n(n\Delta)\} = \sum_{m=1}^{N-n} a_m a_{m+n} \cos(\phi_m - \phi_{m+n}), \quad (10)$$

and that

$$\text{Im}\{\overline{M}_n(n\Delta)\} = - \sum_{m=1}^{N-n} a_m a_{m+n} \sin(\phi_m - \phi_{m+n}). \quad (11)$$

We also remember that the iterator  $n$  above spans the range  $1 \leq n \leq N-1$ . Examining (10) and (11) we recognize that the only unknowns are the values for the phase parameters,  $\phi_n$ . Both the initial amplitudes  $a_n$  and the LHS of each equation are given. The LHS values are found by calculating the Fourier transform of the intensity distribution that we measure in the Fourier plane, see the “analysis plane” in Figure 1, and determining the value of the resulting complex function at the locations  $x = n\Delta$ .

We also note that the larger the value of  $n$ , the lower the number of terms from (10) and (11) that contribute to both  $\text{Im}\{\overline{M}_n(n\Delta)\}$  and  $\text{Re}\{\overline{M}_n(n\Delta)\}$ . When we set about trying to find  $\phi_n$  from (10) and (11), we start by first setting  $n = N-1$ , in which case the equations reduce to the following:

$$\text{Re}\{\overline{M}_{N-1}((N-1)\Delta)\} = a_1 a_N \cos(\phi_1 - \phi_N), \quad (12)$$

and

$$\text{Im}\{\overline{M}_{N-1}((N-1)\Delta)\} = -a_1 a_N \sin(\phi_1 - \phi_N). \quad (13)$$

If we arbitrarily set  $\phi_1 = 0$ , then we can calculate  $\phi_N$  from the following

$$\phi_N = \arctan \left[ \frac{\sin(\phi_N)}{\cos(\phi_N)} \right], \quad (14)$$

which means that we now have values for both  $\phi_1$  and  $\phi_N$ .

Now setting  $n = N-2$ , (10) and (11) will reduce to the following:

$$\begin{aligned} \text{Re}\{\overline{M}_{N-2}((N-2)\Delta)\} \\ = a_1 a_{N-1} \cos(\phi_1 - \phi_{N-1}) + a_2 a_N \cos(\phi_2 - \phi_N), \end{aligned} \quad (15)$$

and

$$\begin{aligned} \text{Im}\{\overline{M}_{N-2}((N-2)\Delta)\} \\ = -a_1 a_{N-1} \sin(\phi_1 - \phi_{N-1}) - a_2 a_N \sin(\phi_2 - \phi_N). \end{aligned} \quad (16)$$

It is instructive to consider the next step in the procedure before we generalize the results. Setting  $n = N-3$ , and substituting into (10) and (11), we arrive at

$$\begin{aligned} \text{Re}\{\overline{M}_{N-3}((N-3)\Delta)\} - a_2 a_{N-1} \cos(\phi_2 - \phi_{N-1}) \\ = a_1 a_{N-2} \cos(\phi_1 - \phi_{N-2}) + a_3 a_N \cos(\phi_3 - \phi_N), \end{aligned} \quad (17)$$

and

$$\begin{aligned} \text{Im}\{\overline{M}_{N-2}((N-1)\Delta)\} + a_2 a_{N-1} \sin(\phi_2 - \phi_{N-1}) \\ = -a_1 a_{N-2} \sin(\phi_1 - \phi_{N-2}) - a_3 a_N \sin(\phi_3 - \phi_N). \end{aligned} \quad (18)$$

Again we see that we can calculate the LHS of (17) and (18) from an experimental measurement and by using values for  $\phi_2$  and  $\phi_{N-1}$  that were estimated in the previous iteration step. We summarize our theoretical results so far:

- (i) We set  $\phi_1 = 0$  and calculate  $\phi_N$  using (14)
- (ii) Once  $\phi_1$  and  $\phi_N$  are determined, we need in turn to determine  $\phi_2$  and  $\phi_{N-1}$  from (12) and (13)
- (iii) If we can find values for  $\phi_2$  and  $\phi_{N-1}$ , then we need to repeat the process to determine  $\phi_3$  and  $\phi_{N-2}$
- (iv) We repeat this iterative process  $N/2 - 1$  times to find all the unknown phase values

To proceed further we must therefore find a solution to the following coupled set of equations

$$\Omega_R = a \cos(\alpha) + b \cos(\beta - \Theta), \quad (19)$$

$$\Omega_I = a \sin(\alpha) - b \sin(\beta - \Theta), \quad (20)$$

where  $\alpha$  and  $\beta$  are the unknown phase values for a particular step in the iterative procedure. Using a software package like Mathematica it is possible to find an analytical solution for these equations; however the solution is not unique: there are 8 possible coupled values for  $\alpha$  and  $\beta$ .

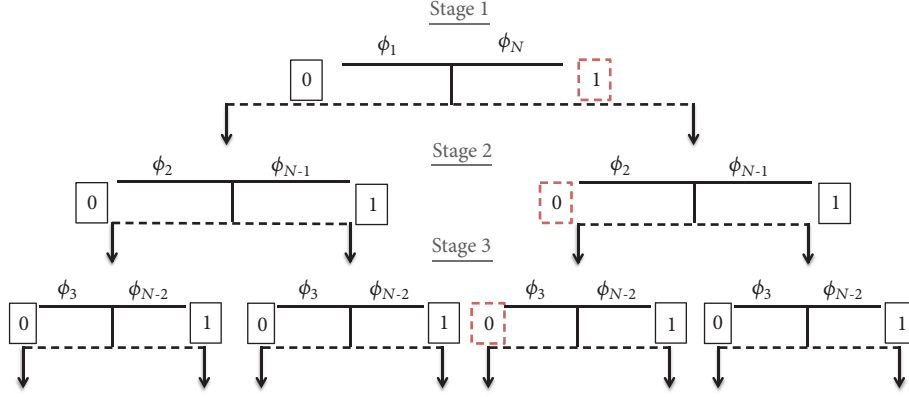


FIGURE 2: Decision tree illustrating the choices made by the algorithm as it steps through the unknown phase values. At each stage of the algorithm, a choice between two paths, Path 0 or Path 1, is made. A particular path through the solution space is then uniquely identified with a bit sequence. For example, if the dashed red boxes are chosen at each stage of the algorithm being chosen, this corresponds to the path [1 0 0 ....].

### 3. Algorithm Analysis

In this section we will examine some of the implications of the theoretical analysis we have just derived. First we will examine how we may reduce the number of possible solutions at each level of the iteration, reducing them from eight to two. To find a phase value for each contributing point source the algorithm must move through  $N/2 - 1$  steps. At each step a decision on which solution to take must be made; we examine how this can be considered as a set of different possible paths through the solution space. We examine the character of the solutions produced by the algorithm. Finally we examine how to prune (reduce) the solution space by ruling out “unphysical” solutions and outline an algorithm for implementing this procedure.

*3.1. From Eight Solutions to Two.* We note that it is possible to rewrite the coupled equations, (19) and (20), in the following form

$$\Omega_R = as_1 + bs_2, \quad (21)$$

$$\Omega_I = a\sqrt{1-s_1^2} - b\sqrt{1-s_2^2}, \quad (22)$$

where  $\cos(\alpha) \rightarrow s_1$ ,  $\cos(\beta - \Theta) \rightarrow s_2$  and where we use the trigonometric relation  $\cos^2(A) + \sin^2(A) = 1$  and hence we can write the  $\sin(\alpha)$  in terms of the  $\cos(\alpha)$ , i.e.,  $\sin(\alpha) = \sqrt{1 - [\cos(\alpha)]^2}$ . Using (21) to find an expression for  $s_2$  and subbing into (22) we can express  $s_1$  as a quartic equation with four possible solutions [51]. For each value of  $s_1$  there are two possible angles for  $\alpha$  that satisfy  $s_1 = \cos(\alpha)$  and hence eight possible solutions for  $\alpha$  and similarly eight solutions for  $\beta$ .

This is where the difficulties with our phase retrieval approach begin in earnest. Although it is possible to find an analytical solution to the coupled equations (19) and (20), the solution has eight different possible solutions for the unknown pair:  $(\alpha, \beta)$ . In reality however only one of the solution pairs corresponds to the actual correct physical result. If we randomly choose from these solutions we will

have a probability of 1/8 that we have chosen the physically correct answer.

Having decided on a particular choice of  $(\phi_2, \phi_{N-2})$ , we can then set  $n = N - 3$  and repeat the process. Hence at each step we have a 1/8 chance of guessing the physically correct solution, and for  $N$  point sources we will need to make approximately  $N/2 - 1$  guesses at each step of the algorithm. Hence the chance that we correctly guess the correct phase for each point source is  $(1/8)^{N/2-1}$ , which would seem to be a vanishingly small probability. In practical experimental phase retrieval systems we may wish to find  $N$  phase values where  $N \approx 10^6$ .

Fortunately, we have found from numerical simulations that although there are eight solutions possible in principal, including solutions with complex values, in practice when we substitute real physical parameters into our system of equations several of these solutions yield the same answer. We have found that at each step in the algorithm only two solutions are produced. This is the case for all simulations we have run. We do not pursue this question further here, concluding that at each step in an iterative algorithm we are able to find two solutions that are physically valid and satisfy (19) and (20).

*3.2. Solution Paths.* From the previous section we have found that it is possible at each stage in the iterative procedure to reduce the number of solutions to two possible answers. At each stage in the algorithm then a “binary” choice has to be made about which solution to choose. If we have  $N$  contributing point sources then we must move through  $N/2 - 1$  stages. In Figure 2, we depict how to track our progress through such a decision tree, in this example making the following choices at each stage of the algorithm, [1, 0, 0, ...]; see the red dashed boxes in Figure 2. In general then there are  $2^{(N/2-1)}$  possible paths in total and each possible path is identified as a unique binary number. For example, if  $N = 8$ , then there are  $2^3$  or 8 possible solutions and if  $N = 16$ , there are  $2^7$  or 128 solutions while if  $N = 32$  the number of possible solutions jumps to 32,768.

**3.2.1. Results of Numerical Simulations.** We have run numerous numerical simulations of the equations derived in Section 2 with some interesting results that we now summarize.

- (i) The correct phase solution is always found among the other different solutions
- (ii) The overwhelming majority of solutions have complex numbers for the phase and hence can be excluded as real physical solutions to the phase retrieval problem
- (iii) There are often several other real valued solutions in addition to the actual real solution
- (iv) We have run several numerical simulations with  $N = 32$ . In one run we found that there are 32,768 solutions of which 32,764 are complex and the 2 remaining solutions are real valued, one of which is the correct phase solution. On a second run we found that only 32,762 solutions were complex while the 6 remaining were real valued, one of which was the correct solution.

We conclude that if we had unlimited computing resources and time it would in principle be possible to calculate all possible solutions even when  $N$  is very large, for example,  $N \approx 10^6$ . In practice however this calculation would result in a solution space of  $2^{499999}$ , which is not feasible with standard computing resources. When  $N$  is relatively small and all the possible solutions can be calculated we have found that the vast majority are complex valued, and only a small number of solutions are real valued.

**3.3. Pruning the Solution Space.** From the preliminary analysis we have reported in the previous section, we find that the overwhelming majority of the solutions yield phase values that are complex and hence “unphysical” in nature and can be discarded. This opens up the opportunity of pruning the solution space. We will now outline a strategy that can be employed to greatly reduce the search space. This solution depends on unique binary number that identifies each particular path through the search space and we note that it will be a  $2^{(N/2-1)}$ -bit number. As we move through the solution space we will need a variable, which we refer to as *location* to keep track of where we are in the search tree. We will also need an iterator variable  $k$  to refer to the “stage” of the algorithm; see Figure 2.

From Figure 2 we see that at the first stage, i.e., when  $k = 1$ , we identify values for  $\phi_1$  and  $\phi_N$  and when  $k = 2$ , we identify possible candidates for  $\phi_2$  and  $\phi_{N-1}$ , which we denote by  $S_0$  and  $S_1$ . We initially set *location* to be all zeros and of length  $2^{(N/2-1)}$ . For example if  $N = 8$  then initially *location* would be set to *location* = 000. We also need to address the individual bits in *location* specifically. We do this using the following notation *location*[ $n$ ], where  $n$  refers to  $n^{th}$  individual bit. We illustrate this with the following example: Consider the case when *location* = 10010 and then *location*[1] = 1, *location*[2] = 0, and *location*[4] = 1.

The algorithm then runs as follows:

- (i) For a given  $N$ , set  $k = 1$  and *location* = 000..., where the length of *location* is  $2^{(N/2-1)}$ ,
- (ii) WHILE  $k < N/2$ ,
  - (1) Using Eq. (20) and Eq. (21), find  $S_0$  and  $S_1$
  - (2) IF  $\text{location}[k] = 0$ , then  $(\phi_k, \phi_{N-k+1}) = S_0$ , ELSE  $(\phi_k, \phi_{N-k+1}) = S_1$
  - (3) IF  $(\phi_k, \phi_{N-k+1})$  are real valued then  $k = k + 1$ ,
  - (4) ELSE:
    - IF  $\text{location}[k] = 0$  then set *location*[ $k$ ] = 1,
    - ELSE  $k = k - 1$ , and *location*[ $k$ ] = 1
- (iii) Return *location*

This algorithm will run through the search space checking the solutions. If a complex solution is found it will choose the alternate solution. For a given stage in the algorithm if both  $S_0$  and  $S_1$  are complex the algorithm will go back up the search tree, updating *location* and choosing a different path through the search space. This algorithm will return only the first real valued solution it finds but can be modified to return all solutions that are physically significant.

When employing the “pruning” approach to search the solutions space we must still search a very large space; however the depth of the search per path will be greatly reduced; see, for example, [52]. This will significantly reduce the number of numerical operations performed. Whether the phase retrieval problem can be solved depends on the rate of branching (or the depth of the search) before a given path can be excluded from further search. From a preliminary analysis based on simulations results we find that the depth when one must search a path before an incorrect complex value is returned as the phase estimate can be modeled using statistical methods. We have found that the average path “length” approximately follows a negative exponential distribution similar to speckle intensity statistics [37, 53].

## 4. Conclusion

In this manuscript we have examined the problem of measuring the phase of an optical wavefield. In the Introduction, we briefly reviewed several approaches for making this measurement before concentrating on iterative phase retrieval. In these phase retrieval problems an attempt is made to estimate the phase of wavefield using usually two or more intensity distributions captured in different Linear Canonical Transform planes. An iterative FFT based algorithm is employed that tunes/modifies the phase values iteratively so that the difference between a numerically calculated intensity distribution and an experimentally captured intensity distribution is minimized. Fienup [41] compares this algorithmic approach to a gradient descent algorithm. As is often the case with such optimization algorithms, they can stagnate at local minima, producing phase estimates that are quite far from the correct physical solution. This is particularly the case when the initial guess at the phase distribution is quite far from this correct physical solution [46]. This is an important issue and different approaches for improving these algorithms are

an active research topic. There is however understandably an emphasis on the numerical aspects of these algorithms.

Here we have deliberately chosen to examine a simplified version of the phase retrieval problem, assuming that we can make perfect measurements of the intensity distribution in an image and its corresponding Fourier plane. We assume that the distribution in the image plane consists of  $N$  point sources with unknown phase values. Importantly we assume that we can measure the intensity distribution in the Fourier plane over an infinite extent and with an infinitely fine resolution; in short we assume that we can perfectly measure the continuous intensity distribution. We have found the following under these idealized conditions:

- (1) It is possible in principle to find solutions to the phase retrieval problem that satisfy the physical constraints of the problem. The algorithm for finding these solutions works iteratively but deterministically and will find among the many solutions returned the physically correct solution
- (2) The number of solutions is enormous; if there are  $N$  contributing point sources there are  $2^{(N/2-1)}$  possible solutions; however the overwhelming majority of these solutions are complex valued and hence “unphysical” and can be excluded as potential solution candidates
- (3) We can modify the algorithm so that “unphysical” solutions are excluded which we refer to as pruning. Using a pruning approach we can significantly reduce the space of possible solutions. The performance of the pruning approach can be approximately estimated using statistical techniques. A critical factor determining whether the algorithm can be computed in a realistic time is the “branching” rate or depth of search before a given solution can be excluded

It is important to also highlight the significant practical shortcomings of this theoretical analysis.

**4.1. Physical Model.** We model the field whose phase values we wish to recover as a set of point sources (with known amplitude) in an image plane which are separated uniformly from each other by a fixed distance,  $\Delta$ . Of course an optical wavefield is continuous in nature and so this representation is only an approximation of the real physical field. Nevertheless in standard iterative phase retrieval problems, the intensity value measured at each pixel is considered to be a point source; hence the description of the field that we use is in keeping with the standard approach in the literature.

There is however a difference in the modeling in this paper for the intensity distribution recorded in the Fourier plane. In this paper we effectively assume that we can measure the continuous Fourier plane intensity; i.e., it is as if we can record and measure the intensity over an infinite plane in the Fourier domain and with an infinitely fine spatial resolution. Making these assumptions means that we can develop convenient analytical equations relating the unknown phase values directly to experimental measurements. These analytical equations are used then to develop the iterative algorithm

so that the phase values can be estimated. This contrasts with real experimental systems in that the intensity in the Fourier plane is measured only at a finite number of locations, i.e., at each pixel, and is therefore sampled. And secondly the Fourier intensity distribution is only measured over the finite extent of the CCD/CMOS array. This summarizes the theoretical differences between the analysis presented in this manuscript and the standard theoretical treatment of the iterative phase retrieval problem.

We note however that it is possible to replicate experimentally the theoretical conditions we have assumed in the manuscript. We can achieve this by making several individual measurements of the Fourier plane intensity distribution where we move the CCD/CMOS array between measurements. Then using standard digital signal processing operations we synthetically increase both the spatial resolution and the spatial extent of the measurement by stitching together the single intensity measurements.

**4.2. Effects of Noise.** A significant shortcoming of this theoretical approach is the effect that even small amounts of measurement noise would have on the algorithm. In every experiment there will be measurement error, for example, electronic noise in the readout of a CCD or CMOS device. If a measurement is made on a variable that has a low signal level, the relative error tends to be larger [36]. In the situation described here, we find that intensity measurements associated with higher spatial frequencies have a lower number of contributing point sources. For example, the highest spatial frequency component of the measurement has contributions from only two point sources. In general (but not always) these measurements will contain the most noise. These measurements however are used to directly estimate  $\phi_1$  and  $\phi_N$ , which in turn feed iteratively back into the algorithm and are repeatedly used to estimate the remaining phase values.

So we can see that to turn this theoretical approach into a practical solution would require careful experimental measurements and the development of additional signal processing algorithms to overcome unavoidable noise in these measurements. Nevertheless we hope that by approaching the phase retrieval problem from a different direction we stimulate some new interesting ideas and insights and also shed some light on the character of the solution space for the phase distributions that are recovered from intensity measurements.

**4.3. Extension to 2D.** In this manuscript we deliberately focused on a simple 1D theoretical model (we only consider the  $x$  and  $z$  spatial coordinates) so that we could examine different aspects of the phase retrieval problem. We choose to set  $\phi_1$  to zero and then iteratively solve for the other phase values. Extension to 2D, where we consider both  $x$  and  $y$  as well as the  $z$  spatial coordinates, is not necessarily straightforward and will change depending on the geometry of the contributing point sources. For example, if the contributing point sources are arranged in a square lattice, then the highest spatial frequency components arise from the two point sources that are spatially separated from each other by the largest amount,

i.e., the vertices of the square. The square has four vertices; we can assign a phase value of zero to only one of those vertices, which acts as an effective reference value for the others. Sequential illumination with lines of 1D light could also be considered whereupon the 1D analysis considered here could be more easily extended.

## Data Availability

This is a theoretical paper: all signal processing data can be generated from equations therein.

## Conflicts of Interest

The authors declare that they have no conflicts of interest.

## Acknowledgments

The author gratefully acknowledges the EU commission (H2020-TWINN-2015 HOLO, project Nr. 687328), for supporting his attendance at Summer School “Digital Holography and Related Techniques” organized in Stuttgart, 21-23 June 2017. Part of the work described in this paper results from discussions that the author had during this meeting.

## References

- [1] J. D. Jackson, *Classical Electrodynamics*, Wiley, New York, NY, USA, 1962.
- [2] P. Meystre, *Physics Today*, vol. 61, no. 12, pp. 59-60, 2008.
- [3] D. P. Kelly, A simple optical system for interpreting coherence theory , ArXiv e-prints 1609.05734..
- [4] J. Goodman, *Introduction to Fourier Optics*, New York, McGraw-Hill, 2nd edition, 1966.
- [5] E. O'Neill, *Introduction to Statistical Optics* , Dover books on physics, Dover Publications, 2004.
- [6] C. E. Shannon, “A mathematical theory of communication,” *Bell Labs Technical Journal*, vol. 27, pp. 379–423, 1948.
- [7] C. E. Shannon, “Communication in the presence of noise,” *Proceedings of the IRE*, 1998.
- [8] D. Slepian, “On Bandwidth,” *Proceedings of the IEEE*, vol. 64, no. 3, pp. 292–300, 1976.
- [9] A. Stern and B. Javidi, “Shannon number and information capacity of three-dimensional integral imaging,” *Journal of the Optical Society of America A: Optics, Image Science & Vision*, vol. 21, no. 9, pp. 1602–1612, 2004.
- [10] C. Shen, J. Tan, C. Wei, and Z. Liu, “Coherent diffraction imaging by moving a lens,” *Optics Express*, vol. 24, no. 15, pp. 16520–16529, 2016.
- [11] A. W. Lohmann, “Image rotation, wigner rotation, and the fractional fourier transform,” *Journal of the Optical Society of America A: Optics, Image Science, and Vision*, vol. 10, no. 10, pp. 2181–2186, 1993.
- [12] Z. Zalevsky, D. Mendlovic, and A. W. Lohmann, “Understanding superresolution in Wigner space,” *Journal of the Optical Society of America A: Optics, Image Science & Vision*, vol. 17, no. 12, pp. 2422–2430, 2000.
- [13] J. T. Sheridan, B. Hennelly, and D. Kelly, “Motion detection, the Wigner distribution function, and the optical fractional Fourier transform,” *Optics Express*, vol. 28, no. 11, pp. 884–886, 2003.
- [14] A. Stern and B. Javidi, “Sampling in the light of Wigner distribution,” *Journal of the Optical Society of America A: Optics, Image Science & Vision*, vol. 21, no. 3, pp. 360–366, 2004.
- [15] D. P. Kelly, B. M. Hennelly, and J. T. Sheridan, “Magnitude and direction of motion with speckle correlation and the optical fractional Fourier transform,” *Applied Optics*, vol. 44, no. 14, pp. 2720–2727, 2005.
- [16] B. M. Hennelly and J. T. Sheridan, “Generalizing, optimizing, and inventing numerical algorithms for the fractional Fourier, FRESNEL, and linear canonical transforms,” *Journal of the Optical Society of America A: Optics, Image Science & Vision*, vol. 22, no. 5, pp. 917–927, 2005.
- [17] A. Stern, “Uncertainty principles in linear canonical transform domains and some of their implications in optics,” *Journal of the Optical Society of America A: Optics, Image Science & Vision*, vol. 25, no. 3, pp. 647–652, 2008.
- [18] H. T. Yura and S. G. Hanson, “Optical beam wave propagation through complex optical systems,” *Journal of the Optical Society of America A: Optics, Image Science & Vision*, vol. 4, no. 10, p. 1931, 1987.
- [19] D. P. Kelly, J. J. Healy, B. M. Hennelly, and J. T. Sheridan, “Quantifying the 2.5D imaging performance of digital holographic systems,” *Journal of the European Optical Society: Rapid Publications*, vol. 6, 2011.
- [20] D. Gabor, “Microscopy by Reconstructed Wave-Fronts,” *Proceedings of the Royal Society A Mathematical, Physical and Engineering Sciences*, vol. 197, no. 1051, pp. 454–487, 1949.
- [21] D. Gabor, “Microscopy by reconstructed wave fronts: II,” *Proceedings of the Physical Society, Section B*, vol. 64, no. 6, pp. 449–469, 1951.
- [22] D. Gabor, “Light and information,” in *Progress in Optics*, Vol. I, pp. 109–153, North-Holland, Amsterdam; Interscience, New York, 1961.
- [23] J. W. Goodman and R. W. Lawrence, “Digital image formation from electronically detected holograms,” *Applied Physics Letters*, vol. 11, no. 3, pp. 77–79, 1967.
- [24] L. P. Yaroslavskii and N. S. Merzlyakov, *Methods of Digital Holography*, Springer US, Boston, MA, 1980.
- [25] L. Onural and P. D. Scott, “Digital decoding of in-line holograms,” *Optical Engineering*, vol. 26, no. 11, pp. 1124–1132, 1987.
- [26] U. Schnars and W. Jüptner, “Direct recording of holograms by a ccd target and numerical reconstruction,” *Applied Optics*, vol. 33, no. 2, pp. 179–181, 1994.
- [27] G. Pedrini, P. Fröning, H. J. Tiziani, and M. E. Gusev, “Pulsed digital holography for high-speed contouring that uses a two-wavelength method,” *Applied Optics*, vol. 38, no. 16, pp. 3460–3467, 1999.
- [28] W. Osten, T. Baumbach, and W. Jüptner, “Comparative digital holography,” *Optics Express*, vol. 27, no. 20, pp. 1764–1766, 2002.
- [29] P. Picart, J. Leval, D. Mounier, and S. Gougeon, “Some opportunities for vibration analysis with time averaging in digital Fresnel holography,” *Applied Optics*, vol. 44, no. 3, pp. 337–343, 2005.
- [30] G. Pedrini, I. Alexeenko, W. Osten, and U. Schnars, “On-line surveillance of a dynamic process by a moving system based on pulsed digital holographic interferometry,” *Applied Optics*, vol. 45, no. 5, pp. 935–943, 2006.
- [31] D. Claus, P. Bryanston-Cross, and B. Timmerman, “Digital Double Exposure Holography by Means of Polarization Optics,” in *Proceedings of the Digital Holography and Three-Dimensional Imaging*, p. PMA7, Vancouver, Canada, 2007.

- [32] P. Picart and J. Leval, "General theoretical formulation of image formation in digital Fresnel holography," *Journal of the Optical Society of America A: Optics and Image Science, and Vision*, vol. 25, no. 7, pp. 1744–1761, 2008.
- [33] D. P. Kelly, B. M. Hennelly, N. Pandey, T. J. Naughton, and W. T. Rhodes, "Resolution limits in practical digital holographic systems," *Optical Engineering*, vol. 48, no. 9, 2009.
- [34] D. P. Kelly, D. S. Monaghan, N. Pandey, T. Kozacki et al., "Digital Holographic Capture and Optoelectronic Reconstruction for 3D Displays," *International Journal of Digital Multimedia Broadcasting*, vol. 2010, Article ID 759323, 14 pages, 2010.
- [35] D. Claus, D. Iliescu, J. Watson, and J. Rodenburg, "Comparison of different digital holographic setup configurations," in *Proceedings of the Digital Holography and Three-Dimensional Imaging, DH 2012*, p. DM4C.3, USA, May 2012.
- [36] Y. Wu, J. P. Ryle, S. Liu, D. P. Kelly, and A. Stern, "Experimental evaluation of inline free-space holography systems," *Applied Optics*, vol. 54, no. 13, pp. 3991–4000, 2015.
- [37] D. P. Kelly and D. Claus, "Filtering role of the sensor pixel in Fourier and Fresnel digital holography," *Applied Optics*, vol. 52, no. 1, pp. A336–A345, 2013.
- [38] M. R. Teague, "Deterministic phase retrieval: a Green's function solution," *Journal of the Optical Society of America*, vol. 73, no. 11, p. 1434, 1983.
- [39] C. J. R. Sheppard, "Three-dimensional phase imaging with the intensity transport equation," *Applied Optics*, vol. 41, no. 28, pp. 5951–5955, 2002.
- [40] D. P. Kelly, L. Megel, T. Meinecke et al., "A theoretical comparison of Fresnel based digital holography and phase retrieval from the transport of intensity equation," in *Proceedings of the SPIE Optical Engineering + Applications*, p. 88330G, San Diego, California, United States.
- [41] J. R. Fienup, "Phase retrieval algorithms: a comparison," *Applied Optics*, vol. 21, no. 15, pp. 2758–2769, 1982.
- [42] J. R. Fienup, "Reconstruction of a complex-valued object from the modulus of its Fourier transform using a support constraint," *Journal of the Optical Society of America A: Optics, Image Science & Vision*, vol. 4, no. 1, p. 118, 1987.
- [43] P. F. Almoro and S. G. Hanson, "Random phase plate for wave-front sensing via phase retrieval and a volume speckle field," *Applied Optics*, vol. 47, no. 16, pp. 2979–2987, 2008.
- [44] P. F. Almoro, P. N. Gundu, and S. G. Hanson, "Numerical correction of aberrations via phase retrieval with speckle illumination," *Optics Express*, vol. 34, no. 4, pp. 521–523, 2009.
- [45] P. F. Almoro, G. Pedrini, P. N. Gundu, W. Osten, and S. G. Hanson, "Phase microscopy of technical and biological samples through random phase modulation with a diffuser," *Optics Express*, vol. 35, no. 7, pp. 1028–1030, 2010.
- [46] L. Megel, D. P. Kelly, T. Meinecke, and S. Sinzinger, "Iterative phase retrieval and the important role played by initial conditions," in *Fringe 2013*, W. Osten, Ed., pp. 123–128, Springer Berlin Heidelberg, Berlin, Heidelberg, 2014.
- [47] Z. Liu, C. Guo, J. Tan, Q. Wu, L. Pan, and S. Liu, "Iterative phase-amplitude retrieval with multiple intensity images at output plane of gyrator transforms," *Journal of Optics*, vol. 17, no. 2, p. 025701, 2015.
- [48] R. Barakat and G. Newsam, "Necessary conditions for a unique solution to two-dimensional phase recovery," *Journal of Mathematical Physics*, vol. 25, no. 11, pp. 3190–3193, 1984.
- [49] D. P. Kelly, "Numerical calculation of the Fresnel transform," *Journal of the Optical Society of America A: Optics, Image Science & Vision*, vol. 31, no. 4, p. 755, 2014.
- [50] D. P. Kelly, J. T. Sheridan, and W. T. Rhodes, "Fundamental diffraction limitations in a paraxial 4-f imaging system with coherent and incoherent illumination," *Journal of the Optical Society of America A: Optics and Image Science, and Vision*, vol. 24, no. 7, pp. 1911–1919, 2007.
- [51] P. Strobach, "The fast quartic solver," *Journal of Computational and Applied Mathematics*, vol. 234, no. 10, pp. 3007–3024, 2010.
- [52] P. H. Winston, *Artificial Intelligence*, Addison-Wesley Publishing Co., Reading, Mass.-London-Amsterdam, 1977.
- [53] J. Dainty, "The Statistics of Speckle Patterns," vol. 14 of *Progress in Optics*, pp. 1–46, Elsevier, 1977.

## Research Article

# Multirotor UAV-Based Photogrammetric Mapping for Road Design

Muhammad Akmal Zulkipli and Khairul Nizam Tahar 

*Centre of Studies for Surveying Science and Geomatics, Faculty of Architecture, Planning, and Surveying,  
Universiti Teknologi MARA, 40450 Shah Alam, Selangor Darul Ehsan, Malaysia*

Correspondence should be addressed to Khairul Nizam Tahar; nizamtahar@gmail.com

Received 18 June 2018; Revised 6 August 2018; Accepted 13 September 2018; Published 1 October 2018

Guest Editor: Wei Liu

Copyright © 2018 Muhammad Akmal Zulkipli and Khairul Nizam Tahar. This is an open access article distributed under the Creative Commons Attribution License, which permits unrestricted use, distribution, and reproduction in any medium, provided the original work is properly cited.

Unmanned Aerial Vehicles (UAVs) can be used for close range mapping. In engineering survey works, the conventional survey involves huge cost, labour, and time. Low-cost UAVs are very practical in providing reliable information for many applications such as road design. UAVs can provide the output that meets the accuracy of engineering surveys and policies, especially for small-scale mapping. UAVs are also a competitive technology which is stable and rapidly developing, same as other surveying technologies. This study investigates the performance of multirotor UAV for road design. This study involves four phases which consist of preliminary study, data collection, data processing, and analysis. This study focuses on the UAV as a tool to capture data of the ground from a certain altitude. The analysis includes UAV flight planning, image acquisition, and accuracy assessment of road design. It can be concluded that UAVs can be used to provide data for road design with reliable accuracy.

## 1. Introduction

Developed countries are constantly faced with high maintenance cost of aging transportation highways. The growth of the motor vehicle industry and accompanying economic growth has generated a demand for safer, better performing, less congested highways [1]. The growth of commerce, educational institutions, housing, and defense has largely drawn from government budgets in the past, making the financing of public highways a challenge. The multipurpose characteristics of highways, economic environment, and the advances in highway pricing technology are constantly changing. Therefore, the approaches to highway financing, management, and maintenance are constantly changing as well. Management of safety is a systematic process that strives to reduce the occurrence and severity of traffic accidents. The man/machine interaction with road traffic systems is unstable and poses a challenge to highway safety management [2]. High accuracy of topographical information and features information are very important in good road alignment design [3]. There are many previous methods used to capture topography information such as manned satellite

imagery, radar, LiDAR, and land survey. The Ground Sampling Distance (GSD) is the most important characteristic to be considered during road design. The other information such as elevation and positioning also influences the road design.

Previously, topography information especially in road design was obtained from land survey using total station. The land survey method required a lot of time to complete the survey especially for large area. Therefore, this method also increased the cost of the project and labour used to complete the project. The land survey method totally relies on human resource in order to carry out road design. Therefore, the road design is prone to the systematic error done by human. The undulated area is a challenge for land survey method because it requires the human to climb up and down and access the challenging site on their own. The other factor is weather conditions and land ownership issue during conducting the land survey. The long road alignment might cause a lot of errors and it might have problem to merge the data at the end [4]. The other method used to capture topography information is Light Detection and Ranging (LiDAR). This method offers the accurate topographic data

for road design application. LiDAR method can cover the large area in a minutes and could provide the accurate data. LiDAR is also an active sensor which is capable of capturing data the day or night. However, this method is very expensive which can affect the total project cost. Satellite imagery also can be used to obtain topographic information for road design application. The satellite imageries were captured from thousand kilometres from the earth surface [5]. This method could provide the location and classification of topographic information. This method also has its own problem due to the revisit time of the satellite at the same location, weather condition which refer to cloudy condition, and resolution of the satellite images.

The key for increasing the safety of highway systems is to design, build, and maintain them to be far more tolerant of the average range of this man or machine interaction with highways. Technological advancements in highway engineering have improved the design, construction, and maintenance methods used over the years. These advancements have allowed for newer highway safety innovations. By ensuring that all situations and opportunities are identified, considered, and implemented as appropriate, they can be evaluated in every phase of highway planning, design, construction, maintenance, and operation to increase the safety of our highway systems.

The new technology such as UAV photogrammetry opens numerous applications in the close range domain, combining aerial and terrestrial photogrammetry but also introduces low-cost alternatives to the conventional manned aerial photogrammetry [6–9]. UAV systems also offer various applications other than mapping such as surveillance, archaeological, geohazard studies, monitoring, and fire disaster [10–22]. The UAV system is equipped with various intelligent sensors such as barometer, Inertial Navigation System (INS), Global Positioning System (GPS), flight control, navigation control, sonar, and infrared and Electronic Speed Controller (ESC) [23–27]. There are many kinds of UAVs available in the market which are affordable. UAV photogrammetry describes photogrammetric measurement platforms which operate as either remotely controlled, semiautonomously, or autonomously. The definition covers balloons, kites, gliders, airships, rotary, and fixed wing UAVs with the capability for photogrammetric data acquisition in manual, semiautomated, and automated flight modes [28]. Model helicopters are able to operate closer to the object and are highly flexible in navigation compared to fixed wing UAVs. Microdrones are more stable against environmental conditions such as wind. The developments of model helicopters and comparable autonomous vehicles are primarily driven by the artificial intelligence. Nowadays, close range areas can be mapped by combining aerial and terrestrial photogrammetry using UAV technologies and also as an alternative way for large area mapping [29]. Low cost UAVs are used in mapping projects with low budgets. However, in the previous years, low-cost UAVs have reached a level of practical reliability and professionalism which allow the use of these systems such as mapping platforms. In study, the multirotor UAV is used to capture the topographic information for road design application.

## 2. Methodology

This study involves four phases which include preliminary study and planning, data collection, data processing, results, and analysis. The methodology plays an important role in implementing this study accordingly. The first phase is on the preliminary study and the planning of the work which are crucial parts of the study that require a lot of reading and planning. The first phase also includes reconnaissance, calibration of the equipment, and measurement of data. The next phase is on data collection using UAV images and getting the detailed plans from the unit facilities of UiTM Puncak Alam. Then, both sets of data are processed in the laboratory for the third phase of this study which is data processing. The UAV images are processed using the UAV Agisoft PhotoScan software which can generate the X, Y, and Z coordinates of the proposed road. This phase also includes the construction of road mapping of the area of interest. After the data processing is completed, the results are analysed. The flowchart of the research methodology is shown in Figure 1.

Reconnaissance survey is a general study of an area of interest that might be used for a road or airfield. The reconnaissance survey report should summarise all the collected information, including a description of the site, a conclusion on the economy of its use, and, wherever possible, maps. For UAV surveys, the important thing is the area of coverage of the site. Furthermore, the reconnaissance must include geographical features for the decision-making of minimum flying height, direction of flight path, and type of UAV used. Other than that, this survey also needs to consider the wind direction to make sure that it is carried out smoothly and also for the direction of the flying path to obtain better image capture. Figure 2 shows the location of study. Camera calibration is carried out before acquiring the digital aerial images or aerial photographs for the purpose of recovering all camera parameters for digital image processing. This study used a 4K camera with 4000 x 3000 resolution and the process of camera calibration also gives a result of focal length, principal points, radial lens distortion, and tangential lens distortions. These camera parameters need to be included during the interior orientation step in digital image processing

The UAV used in this study is the Quad-Rotors, Phantom 3 Professional. The UAV weight (including battery and propellers) is about 1280 g and the diagonal size (excluding propellers) is 350 mm. Its maximum speed can achieve 16 m/s (ATTI mode, no wind) and has a GPS Mode that uses GLONASS satellite. The UAV maximum flight time is approximately about 23 minutes. A single person can operate this UAV to collect the image data. The hardware uses IOS Ipad to control the flight planning and a computer for processing. The detailed plan is acquired from the unit facilities in the DWG file in AutoCAD and it can be georeferenced using the ArcGIS software. After that, the acquired UAV images were processed using the Agisoft PhotoScan software. Next, the outputs are transferred to the AutoCAD and the ArcGIS software to analyse the outputs.

**2.1. Data Acquisition and Flight Planning.** Flight planning involves the control of dimension of the study area, number

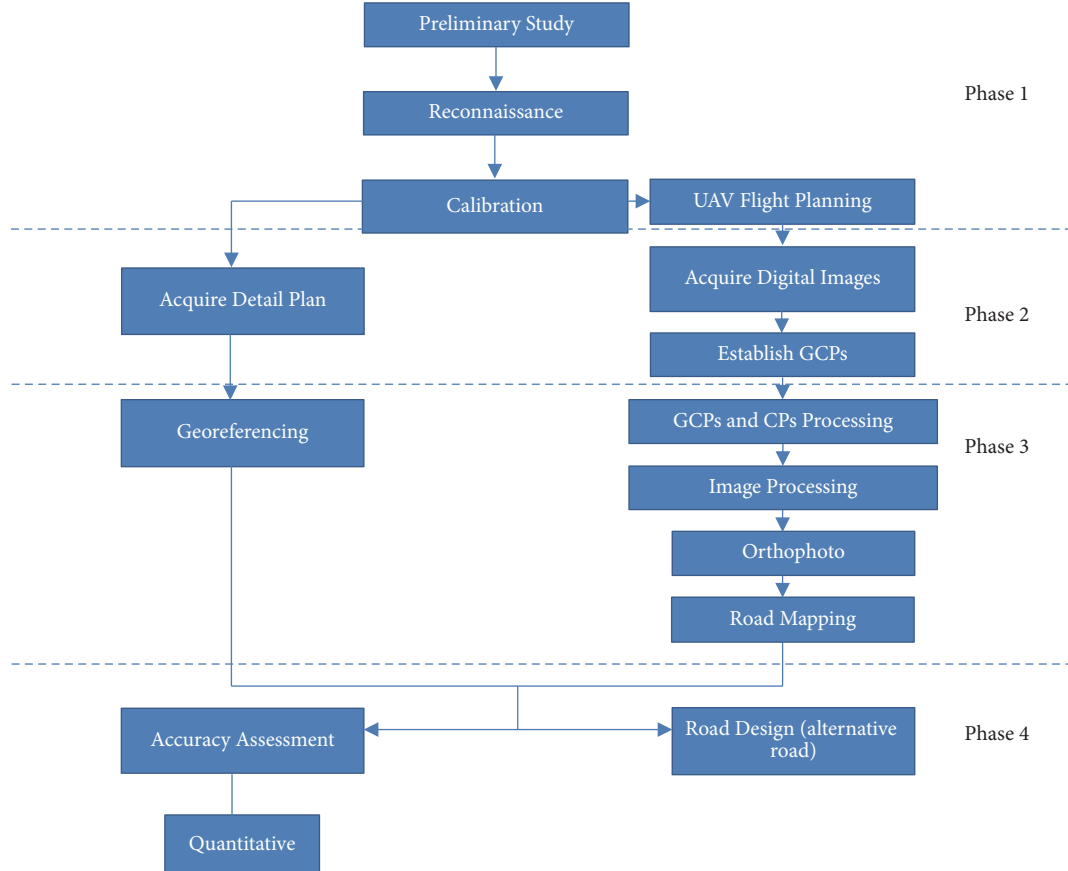


FIGURE 1: Research methodology.



FIGURE 2: Location of study area.

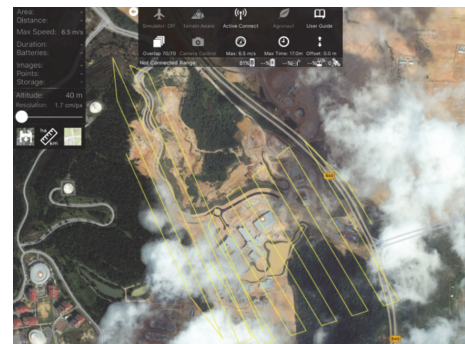


FIGURE 3: Flight planning for acquisition of data.

of strips required, pixel size, photo scale flying height, and percentage of the end lap and side lap. The Map Pilot used is a friendly software for the drone, module Waypoint Editor, and it is able to design flight planning. There are about 122 number of images with 148 m flying height created in the flight planning. In general, the aerial photographs should be overlapped at least 80% and the side for at least 60%. This requirement needs to be fulfilled to make sure that quality photogrammetry results could be obtained. The customised parameters such as spatial resolution, altitude,

endlap, sidelap, and wind direction are as shown in Figure 3. After parameters setting of the flight planning is completed in the Map Pilot, the flight planning is uploaded to the UAV. After uploading, the start button is pressed to begin the image acquisition. Once it started, the UAV gave information of the current altitude of the mission. After the UAV entered the survey area, images are automatically captured every 2.5 seconds and identical speed is used to ensure accurate data. Once the mapping is completed, the UAV returned to the takeoff location and landed automatically.

TABLE 1: Coordinates of road design.

CPs	Conventional Road Design			UAV Images road Design		
	X (m)	Y (m)	Z(m)	X (m)	Y (m)	Z(m)
CP1	-26926.806	3109.908	42.124	-26926.435	3110.456	41.431
CP2	-26847.403	3128.347	44.154	-26847.554	3128.184	44.310
CP3	-26715.708	3158.090	39.246	-26716.024	3157.619	38.570
CP4	-26813.002	3178.296	41.423	-26813.127	3178.034	41.133
CP5	-27024.207	3186.877	43.806	-27024.254	3186.939	44.205
CP6	-26967.798	3240.365	43.403	-26967.768	3240.422	43.903
CP7	-27064.443	3216.702	43.206	-27064.472	3216.801	43.322
CP8	-27167.600	3078.530	44.500	-27167.648	3078.670	44.406
CP9	-27188.670	2957.179	44.720	-27188.601	2957.334	45.069
CP10	-27182.072	2969.390	44.407	-27181.878	2969.580	45.146
CP11	-27078.698	2825.722	48.370	-27078.685	2825.727	48.610
CP12	-26879.317	2724.228	48.912	-26879.289	2724.209	48.114
CP13	-26860.444	2769.504	49.188	-26860.493	2769.433	48.635
CP14	-26851.342	2876.084	45.039	-26851.430	2875.994	44.772



FIGURE 4: Location of GCPs and CPs.

**2.2. Preprocessing and Processing.** The ground control points (GCPs) and check points (CPs) are collected using GPS observation through the rapid static technique. This technique can determine the position information which includes Northing, Easting, and Elevation (X, Y, and Z) through postprocessing by using the GNSS Solution software. This software can convert the raw data to a Rinex file, where it can be used in any GPS processing software for adjustments. The rapid static technique only takes 5 to 20 minutes for observation. In this study, there are six GCPs established for absolute orientation and fourteen CPs. For a better view, Figure 4 shows all the locations of the GCPs and CPs.

After data acquisition has been completed using the multirotor UAV, all acquired raw images data and GCPs are processed using the Agisoft PhotoScan software. The results are presented in the form of a digital map or hardcopy. The Agisoft PhotoScan software requires camera information such as pixel size, focal length, radial lens distortion, and tangential distortion to carry out the interior orientation. A total of six GCPs have been established during absolute orientation. After adding the raw images data in the Agisoft PhotoScan software, the process will start with aligning the photo input in a high accuracy setting and using the Reference for Pair Preselection. The key and tie point limit are 40,000 and 20,000. After aligning the photos, a reference to

establish the GCP on the UAV images is selected by importing the coordinates in the (txt) file. The coordinate is illustrated by point features in the software, where it needs to move the point to the exact location of the GCP. The process will produce Orthophoto and a map.

**2.3. Data Analysis and Assessment.** The objective of this study is to assess the accuracy of road mapping from the UAV product. There are two assessments describing the point and visual analysis. For quantitative accuracy, the error difference between the coordinates of check points by GPS (rapid static technique) and UAV processed images data is assessed using RMSE. After the accuracy assessment has been conducted, an alternative road can be designed using the UAV data and ground survey mapping of the study area. The designed road is focused on increasing the efficiency of road flow. The optimal road alignment is determined based on topographic map of the area and mapping the existing road network. There are two types of alignments which are vertical and horizontal alignment. The horizontal and vertical alignments based on topographic features from the UAV data are determined.

### 3. Results and Analysis

The analysis of the accuracy of the road mapping, production of the road map and all the results will be analysed in this chapter, including the evaluation of UAV images for road design or alternative road. All calculations are made for the RMSE point accuracy assessments and the road design. The accuracy is analysed based on computation of the RMSE between the coordinates of 3D stereo model and the check points. The locations of the check points are shown in Figure 4 with 14 samples (Table 1). It shows the comparisons between CPs using GPS and the 3D coordinates of the stereo model in Agisoft Photoscan software.

It can be seen that the accuracy could be achieved using the UAV system. The smaller the value of the RMSE

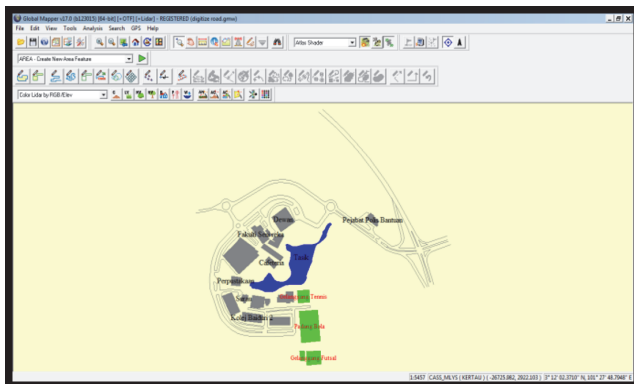


FIGURE 5: Digitized features from UAV images.

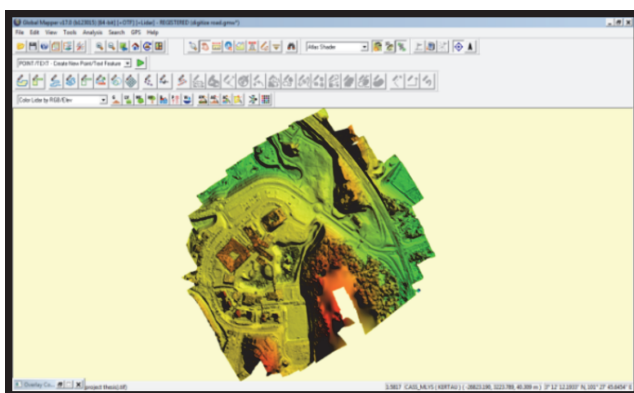


FIGURE 6: Digital surface models of UAV images data.

calculated, the higher the accuracy. Hence, the accuracy of the orthophoto can be calculated by the RMSE value. The latitude, longitude, and elevation (X, Y, and Z) are processed using the GNSS Solution software where the raw data collected from the site are converted to (Rinex) file to be used in any GPS processing software for adjustments. After processing the raw data of the UAV images in the Agisoft Photoscan software, the outcome of orthomosaic in a (tif) file will be imported to the Global Mapper software in order to carry out the digitisation of the features as shown in Figure 5. The analyses are carried out based on road features and the elevation produced by the Digital Surface Model (DSM) (Figure 6). The digitised features are displayed in ArcGIS to visualise the difference from the AutoCAD drawing.

After both road designs are completed, both UAV images and conventional road design are compared with the coordinate of chainage in every 30 meter intervals. In the CDS software, parameters of the road are needed to design the road curve such as bearing in, bearing out, and the optimum radius for the road curve. Two road curves have been designed with the radius of 50 and 60 meters for the first and second curve. After clicking the position of the Intersection Point and keying in the value of radius, bearing in and bearing out the software will calculate the other parameters values which are available for the designed road curve such as arc, chord, and tangent length. Figure 7 shows the finished road design

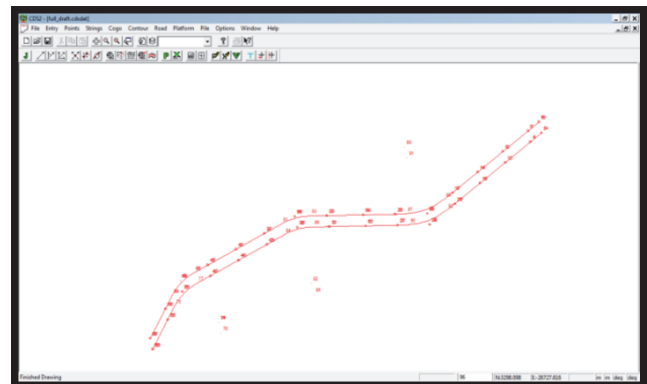


FIGURE 7: Complete road designs for UAV Images and Conventional Survey.

with 50 and 60 m radius. This radius follows the public work department standards for Exclusive Motorcycle Lane, EML.

#### 4. Discussions

After producing the adjustment coordinates, the WGS84 coordinate system is converted to a local coordinate system from angular units to meters. The coordinate system that is chosen is Cassini Malaysia, Selangor, by using Kertau as a datum. The reason that the coordinate system is converted to Cassini Malaysia is because it is easy to analyse the meter units than the angular degree minutes and seconds, where it can check the miss-closure (meter) of the data. The RMSE for x, y, and z coordinates are  $\pm 0.155$  metres,  $\pm 0.228$  metres, and  $\pm 0.479$  metres, respectively (Table 2).

In the Global Mapper software, digitising of features are carried out using orthophoto image and then exported to ArcGIS in order to produce a map. The analysis only focused on road features and it could be displayed in ArcGIS to visualise the differences between UAV road mapping and conventional road mapping. The AutoCAD drawings are obtained from the unit facilities of UiTM Puncak Alam. Figure 8 shows the slight difference between two methods of producing the map; the road with the pink outline is drawn using the AutoCAD software which is obtained from conventional ground measurement while the grey outline is digitised from the UAV's orthophoto in the Global Mapper software.

#### 5. Conclusions and Recommendations

Road mapping is produced from the UAV images using the Agisoft Photoscan software to create an orthophoto image. All the images went through the scaling and level process which also referred to the orientations such as interior, relative, and exterior orientation. It is demonstrated that the UAV together with the digital camera are capable of acquiring aerial photograph successfully for large scale mapping in a short amount of time. This study shows that UAV is also capable of producing road mapping at the selected study area. All of the results are analysed using the Root Mean

TABLE 2: Analysis on disparity between conventional and UAV coordinates.

CPs	X(m)	Y(m)	Z(m)	X <sup>2</sup> (m)	Y <sup>2</sup> (m)	Z <sup>2</sup> (m)
CP1	-0.371	-0.548	-0.693	0.138	0.300	0.480
CP2	0.151	0.163	-0.156	0.023	0.027	0.024
CP3	0.316	0.471	0.676	0.100	0.222	0.457
CP4	0.125	0.262	0.290	0.016	0.069	0.084
CP5	0.047	-0.062	-0.399	0.002	0.004	0.159
CP6	-0.030	-0.057	-0.500	0.001	0.003	0.250
CP7	0.029	-0.099	-0.116	0.001	0.010	0.013
CP8	0.048	-0.140	0.094	0.002	0.020	0.009
CP9	-0.069	-0.155	-0.349	0.005	0.024	0.122
CP10	-0.194	-0.190	-0.739	0.038	0.036	0.546
CP11	-0.013	-0.005	-0.240	0.000	0.000	0.058
CP12	-0.028	0.019	0.798	0.001	0.000	0.637
CP13	0.049	0.071	0.553	0.002	0.005	0.306
CP14	0.088	0.090	0.267	0.008	0.008	0.071
RMSE (m)				0.155	0.228	0.479

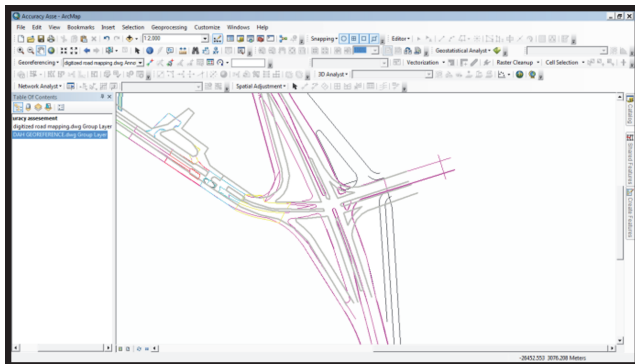


FIGURE 8: Visual Accuracy Assessments of Both Road Designs.

Square Error (RMSE). RMSE can assess the accuracy of the UAV images using the check points that have been measured on the ground for data validation analysis. The designed road in this study is for proposing an alternative road to increase the efficiency of road traffic flow. The Digital Terrain Model (DTM) data from the UAV images processed is used to evaluate the geographic features where it must follow the design policy parameters in order to help control the design of the road. The safety of the users must also be calculated by selecting the super elevation of the proposed road. Therefore, the alternative road can be designed using the parameters for road design provided by public work department standards. In the future, the accuracy of the orthophoto can be improved and enhanced by increasing the number of GCPs and CPs during data collection in the field using the GPS technique. It can also minimise the RMSE in data processing. The use of DTM (digital terrain model) for road design to check the accuracy of the road designed and to improve the validation of using UAV for road design construction. Different types of UAV should be used to improve the flexibility of the survey works; for example, a fixed wing UAV can cover a large area to

get more details for the topographical map to design a road. Different methods of camera calibration could be applied to optimise the quality of the UAV image processing. MyRTKnet data should be used as a base for better control of the coordinate GCP to apply on the UAV images for processing. Different flying heights should be applied for UAV to conduct better results for road design.

## Data Availability

The data used to support the findings of this study are available from the corresponding author upon request.

## Conflicts of Interest

The authors declare that they have no conflicts of interest.

## Acknowledgments

Faculty of Architecture, Planning, and Surveying Universiti Teknologi MARA (UiTM), Research Management Institute (RMi), and Ministry of Higher Education (MOHE) are greatly acknowledged for providing the fund BESTARI 600-IRMI/MyRA 5/3/BESTARI (001/2017) to enable this research to be carried out. The authors would also like to thank the people who were directly or indirectly involved in this research.

## References

- [1] Z. Jaal and J. Abdullah, "User's Preferences of Highway Landscapes in Malaysia: A Review and Analysis of the Literature," *Procedia - Social and Behavioral Sciences*, vol. 36, pp. 265–272, 2012.
- [2] S. Martínez, J. Ortiz, and M. L. Gil, "Geometric documentation of historical pavements using automated digital photogrammetry and high-density reconstruction algorithms," *Journal of Archaeological Science*, vol. 53, pp. 1–11, 2015.

- [3] M. M. S. Albattah, "Optimum Highway Design and Site Location Using Spatial Geoinformatics Engineering," *Journal of Remote Sensing & GIS*, vol. 5, no. 1, p. 10, 2016.
- [4] P. Kettunen, C. Koski, and J. Oksanen, "A design of contour generation for topographic maps with adaptive DEM smoothing," *International Journal of Cartography*, vol. 3, no. 1, pp. 19–30, 2017.
- [5] F. van Coillie, K. Delaplace, D. Gabriels et al., "Monotemporal assessment of the population structure of *Acacia tortilis* (Forssk.) Hayne ssp. *raddiana* (Savi) Brenan in Bou Hedma National Park, Tunisia: A terrestrial and remote sensing approach," *Journal of Arid Environments*, vol. 129, pp. 80–92, 2016.
- [6] H. Eisenbeiss, UAV Photogrammetry, DISS. ETH NO. 18515, 1–237, 2009.
- [7] Y. Fujii, E. Fodde, K. Watanabe, and K. Murakami, "Digital photogrammetry for the documentation of structural damage in earthen archaeological sites: the case of Ajina Tepa, Tajikistan," *Engineering Geology*, vol. 105, no. 1-2, pp. 124–133, 2009.
- [8] Z. Lin, "UAV airborne low altitude photogrammetry system," *Science of Surveying and Mapping*, vol. 36, no. 1, p. 5, 2011.
- [9] M. A. Núñez, F. Buill, and M. Edo, "3D model of the Can Sadurní cave," *Journal of Archaeological Science*, vol. 40, no. 12, pp. 4420–4428, 2013.
- [10] H. Bendea, F. Chiabrando, F. Tonolo, and D. Marenchino, "Mapping of archaeological areas using a low-cost UAV the Augusta Bagiennorum Test," *XXI International CIPA Symposium*, pp. 1–8, 2007.
- [11] I. Colomina and P. Molina, "Unmanned aerial systems for photogrammetry and remote sensing: a review," *ISPRS Journal of Photogrammetry and Remote Sensing*, vol. 92, pp. 79–97, 2014.
- [12] G. J. Grenzdörffer, M. Guretzki, and I. Friedlander, "Photogrammetric image acquisition and image analysis of oblique imagery," *The Photogrammetric Record*, vol. 23, no. 124, pp. 372–386, 2008.
- [13] R. N. Jiang and D. V. Jauregui, "Development of a digital close-range photogrammetric bridge deflection measurement system," *Measurement*, vol. 43, no. 10, pp. 1431–1438, 2010.
- [14] T. Luhmann, "Close range photogrammetry for industrial applications," *ISPRS Journal of Photogrammetry and Remote Sensing*, vol. 65, no. 6, pp. 558–569, 2010.
- [15] K. Konolige and M. Agrawal, "FrameSLAM: From bundle adjustment to real-time visual mapping," *IEEE Transactions on Robotics*, vol. 24, no. 5, pp. 1066–1077, 2008.
- [16] S. G. Kontogiannis and J. A. Ekaterinaris, "Design, performance evaluation and optimization of a UAV," *Aerospace Science and Technology*, vol. 29, no. 1, pp. 339–350, 2013.
- [17] M. Röder, H. Latifi, S. Hill et al., "Application of optical unmanned aerial vehicle-based imagery for the inventory of natural regeneration and standing deadwood in post-disturbed spruce forests," *International Journal of Remote Sensing*, pp. 1–22, 2018.
- [18] L. Sahar, S. Muthukumar, and S. P. French, "Using aerial imagery and gis in automated building footprint extraction and shape recognition for earthquake risk assessment of urban inventories," *IEEE Transactions on Geoscience and Remote Sensing*, vol. 48, no. 9, pp. 3511–3520, 2010.
- [19] S. Pal Singh, K. Jain, and V. Mandla, "Virtual 3D Campus Modeling by Using Close Range Photogrammetry," *American Journal of Civil Engineering and Architecture*, vol. 1, no. 6, pp. 200–205, 2013.
- [20] K. N. Tahar and A. Ahmad, "Production of Orthophoto and Volume Determination Using Low-Cost Digital Cameras," *Pertanika Journal of Science and Technology*, vol. 21, no. 2, pp. 387–396, 2011.
- [21] P. Xiaodong and L. Zongjian, "Unmanned airship low altitude system for aerial photogrammetry," *Science of Surveying and Mapping*, vol. 34, no. 4, pp. 33–35, 2009.
- [22] X. Du, X. Jin, X. Zhang, J. Shen, and X. Hou, "Geometry features measurement of traffic accident for reconstruction based on close-range photogrammetry," *Advances in Engineering Software*, vol. 40, no. 7, pp. 497–505, 2009.
- [23] J. Chahl, "Three biomimetic flight control sensors," *International Journal of Intelligent Unmanned Systems*, vol. 2, no. 1, pp. 27–39, 2014.
- [24] H. Chao, Y. Cao, and Y. Chen, "Autopilots for small unmanned aerial vehicles: A survey," *International Journal of Control, Automation, and Systems*, vol. 8, no. 1, pp. 36–44, 2010.
- [25] F. Delgado, J. Carvalho, T. Coelho, and A. Dos Santos, "An Optical Fiber Sensor and Its Application in UAVs for Current Measurements," *Sensors*, vol. 16, no. 11, p. 1800, 2016.
- [26] S. Jabari, F. Fathollahi, A. Roshan, and Y. Zhang, "Improving UAV imaging quality by optical sensor fusion: an initial study," *International Journal of Remote Sensing*, vol. 38, no. 17, pp. 4931–4953, 2017.
- [27] A. B. Junaid, Y. Lee, and Y. Kim, "Design and implementation of autonomous wireless charging station for rotary-wing UAVs," *Aerospace Science and Technology*, vol. 54, pp. 253–266, 2016.
- [28] H. Eisenbeiss, *Photogrammetric Week '11*, F. Dieter, Ed., 2011, Wichmann/VDE Verlag, Berlin & Offenbach.
- [29] K. N. Tahar and A. Ahmad, "A simulation study on the capabilities of rotor wing unmanned aerial vehicle in aerial terrain mapping," *International Journal of Physical Sciences*, vol. 7, no. 8, 2012.

## Research Article

# Two-Step Phase Retrieval Algorithm Using Single-Intensity Measurement

Cheng Zhang<sup>1,2</sup>, Meiqin Wang<sup>1</sup>, Qianwen Chen,<sup>1</sup> Dong Wang,<sup>1</sup> and Sui Wei<sup>1</sup>

<sup>1</sup>Key Laboratory of Intelligent Computing and Signal Processing, Ministry of Education, Anhui University, Hefei, Anhui Province 230039, China

<sup>2</sup>Key Laboratory of Modern Imaging and Displaying Technology, Anhui University, Hefei, Anhui Province 230039, China

Correspondence should be addressed to Meiqin Wang; 2417724433@qq.com

Received 13 July 2018; Accepted 30 August 2018; Published 1 October 2018

Academic Editor: Xiaowei Li

Copyright © 2018 Cheng Zhang et al. This is an open access article distributed under the Creative Commons Attribution License, which permits unrestricted use, distribution, and reproduction in any medium, provided the original work is properly cited.

Aiming at the problem that the single-intensity phase retrieval method has poor reconstruction quality and low probability of successful recovery, an improved method is proposed in this paper. Our method divides the phase retrieval into two steps: firstly, the GS algorithm is used to recover the amplitude in the spatial domain from the single-spread Fourier spectrum, and then the classical GS algorithm using two intensity measurements (one is recorded and the other is estimated from the first step) measurements is used to recover the phase. Finally, the effectiveness of the proposed method is verified by numerical experiments.

## 1. Introduction

Most of the information in the optical field is contained in the phase, such as the depth and shape of the object and so on. The oscillation frequency of the optical field is as high as  $10^{15}$  Hz. However, existing detection devices can only record intensity, directly [1]. Phase retrieval method recovers lost phase from recorded intensity measurements with some prior knowledge, which plays an important role in the imaging field. Phase retrieval problem arises in numerous of areas, such as crystallography [2–4], optics [5–9], astronomical imaging [10], microscopy [11, 12], biomedical [13], and holographic imaging[14, 15].

In 1972, Gerchberg and Saxton first proposed an alternate projection-based phase retrieval algorithm, the Gerchberg-Saxton (GS) algorithm [16]. The main idea of GS algorithm is to use the intensity of the spatial domain and the Fourier domain to recover the phase of the optical field. Subsequently, Fienup proved that the GS algorithm had obvious error-decreasing properties, Error Reduction (ER) algorithm, and Hybrid Input-Output (HIO) algorithm were proposed [17]. At present, ER algorithm and HIO algorithm are considered to be the most effective methods in the field of phase retrieval [18]. Since the above algorithms are only suitable for a positive

linear transformation system, nobody cares about any linear transformation system. Therefore, Yang and Gu proposed the amplitude-phase detection theory in arbitrary linear transformation systems, namely, the Yang-Gu (Y-G) algorithm [19]. In 2015, Guo et al. optimized the iterative algorithm and proposed two improved GS iterative phase retrieval algorithms, which were the spatial phase perturbation GS algorithm and the combined GS HIO algorithm. For the two improved algorithms, the squared value of the squared error value rapidly drops to an acceptable value, and the lost phase can be successfully recovered in the spatial domain and Fourier domain, which means that both algorithms can jump out of the local minimum value and convergence to the global minimum [9].

The GS algorithm was originally proposed in connection with the problem of reconstructing phase given only two-intensity measurements in the spatial domain and Fourier domain, i.e., given two intensity measurements (one is recorded in the spatial domain and the other is estimated in the Fourier domain) measurements. Unfortunately, such two intensity measurements at two different planes cannot be measured in some cases. Therefore, a GS algorithm using single-intensity measurement with some prior knowledge combined was proposed to recover the phase. However the

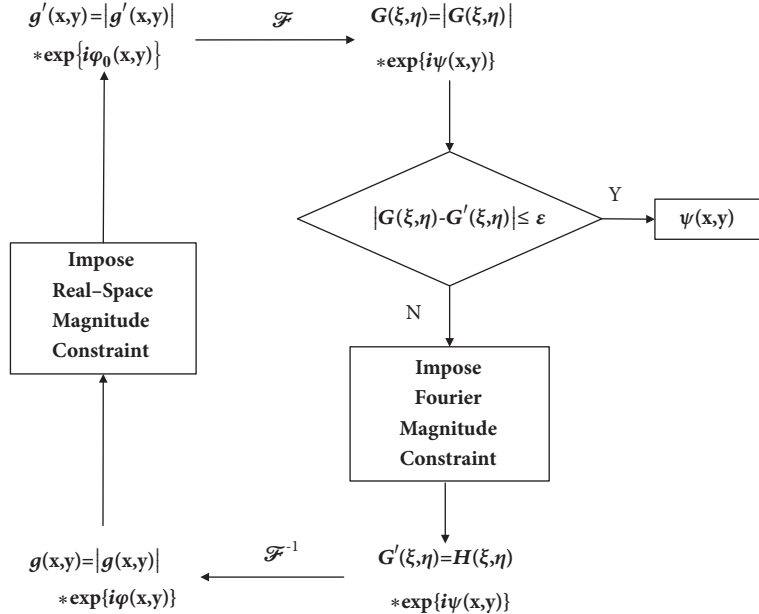


FIGURE 1: Flow chart of classical GS algorithms using two intensity measurements, i.e., TIPR.

single-intensity phase retrieval method has the drawbacks of poor reconstruction quality and low probability of successful recovery. This paper proposes an improved method based on single-intensity measurement, Two-Step Phase Retrieval (TSPR) from single-intensity measurement algorithm. The main idea of the TSPR algorithm is to first recover the amplitude (i.e., the square root of the intensity) in the spatial domain using the Single-Intensity Phase Retrieval (SIPR) algorithm with some prior knowledge and then recover the phase in the spatial domain using the Two-Intensity Phase Retrieval (TIPR) algorithm. Experimental results demonstrate that our proposed TSPR algorithm can effectively enhance the quality of phase recovered and the probability of successful recovery.

## 2. Basic Principles

The complex amplitude  $g(x, y)$  is

$$g(x, y) = |g(x, y)| \exp(i\varphi(x, y)) \quad (1)$$

Its Fourier transform form is

$$G(\xi, \eta) = |G(\xi, \eta)| \exp(i\psi(\xi, \eta)) \quad (2)$$

where  $g(x, y)$  and  $G(\xi, \eta)$  denote the complex amplitude in the spatial domain and Fourier domain, respectively,  $|g(x, y)|$  and  $|G(\xi, \eta)|$  denote the amplitude in the spatial domain and Fourier domain, respectively,  $\varphi(x, y)$  and  $\psi(\xi, \eta)$  denote the phase in the spatial domain and Fourier domain, respectively. Phase retrieval refers to recovering the losing phase  $\varphi(x, y)$  in the spatial domain from two amplitudes  $|g(x, y)|$  and  $|G(\xi, \eta)|$ .

The flow chart of the classical GS algorithm is shown in Figure 1. This algorithm was first proposed and was

easily used to solve the phase retrieval problem using two intensity measurements.  $\exp(i\phi_0(x, y))$  denotes the initialized phase distribution function. The algorithm repeatedly iterates between the spatial domain and the Fourier domain until the error  $\varepsilon$  satisfies the termination condition [20].

## 3. Two-Step Phase Retrieval Using Single-Intensity Measurement

The TIPR algorithm uses the two intensity measurements recorded in the spatial domain and the Fourier domain, respectively, to recover the amplitude and phase in the spatial domain with high quality. Although the TIPR algorithm can achieve good results, in some case, it is difficult to obtain two intensity measurements simultaneously in the both spatial and Fourier domains.

Therefore, the SIPR algorithm is proposed, and it can recover the phase from single-intensity measurement in the Fourier domain with some prior knowledge. However, the SIPR method has low probability of successful recovery and poor quality. As shown in Figure 2, the purpose of the experiment is to test the SIPR method's performance to recover the amplitude and phase. The coded aperture is generated by a uniform distribution. The sampling rate of the coded aperture is used as a variable parameter in the experiment. The sampling rate gradually increased from 0.1 to 0.7; the step length is 0.05. The experiment runs 500 times independently to compute the probability of successful recovery. If the SNR of the phase reconstructed is greater than 25 dB, the reconstruction is deemed as successful. The probability of successful recovery versus sampling rate for both amplitude and phase is shown in Figure 2.

As depicted in Figure 2, it can be found that the SIPR method can achieve high probability of successful recovery

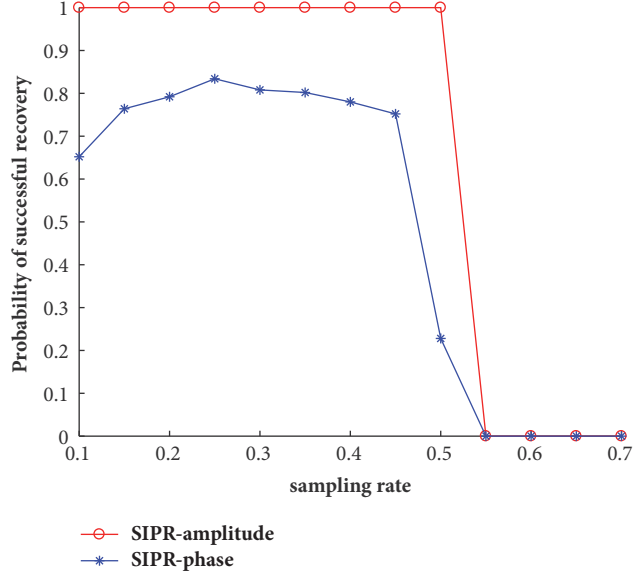


FIGURE 2: Probability of successful recovery of amplitude and phase versus sampling rate.

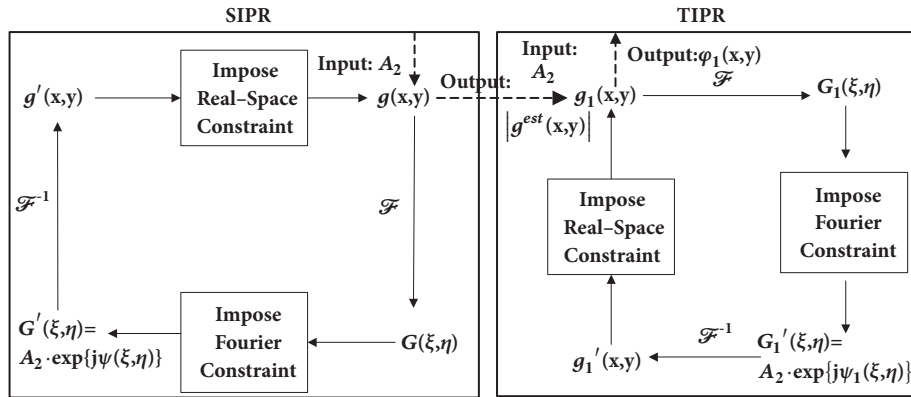


FIGURE 3: Flow diagram of the TSPR algorithm.

of the amplitude, but the probability of successful recovery of the phase is very low and unstable. Hence, our TSPR method is proposed to solve the phase retrieval problem from single-intensity measurement. Firstly, SIPR method is used to recover the amplitude in the spatial domain from the intensity in the Fourier domain and the support set in the spatial domain. Then, TIPR method using two intensity measurements (one of the two intensity measurements is recorded in the Fourier domain and the other is estimated in the spatial domain from the first step) is used to recover the phase in the spatial domain.

The flow chart of TSPR method is shown in Figure 3, which includes the following steps: (1) initialize the amplitude  $A_1$  and phase  $\varphi_0(x, y)$  in the spatial domain, i.e., use all-one amplitude and randomized phase. (2) Perform Fourier transform on the complex amplitudes and replace the amplitude after the Fourier transform in the Fourier domain with the recorded Fourier amplitudes  $A_2$ . (3) Perform the inverse Fourier transform on the synthesized complex amplitude in

the Fourier domain and multiply it with the support in the spatial domain. (4) Repeat steps (2)-(3) until the amplitude converges in the spatial domain. (5) The classical TIPR algorithm using the recorded Fourier amplitude  $A_2$  and the estimated amplitude  $|g^{est}(x, y)|$  from the first step is used to iteratively recover the phase in the spatial domain.

The complex amplitude of the initialization is as follows:

$$g(x, y) = A_1 \cdot \exp [\varphi_0(x, y)] \quad (3)$$

The optical setup of imaging process of the TSPR method is shown in Figure 4. The coded aperture and CCD are placed on the front and back focal planes of the lens, respectively.

Firstly, the complex optical field  $u(x, y)$  is filtered through the coded aperture  $M$  to obtain a complex optical field  $u_M(x, y)$  and then imaged by a Fourier lens; finally the intensity is recorded in the CCD plane. The intensity recorded at the CCD plane is expressed as follows:

$$I_{CCD} = |\mathcal{F}[u_M(x, y)]|^2 \quad (4)$$

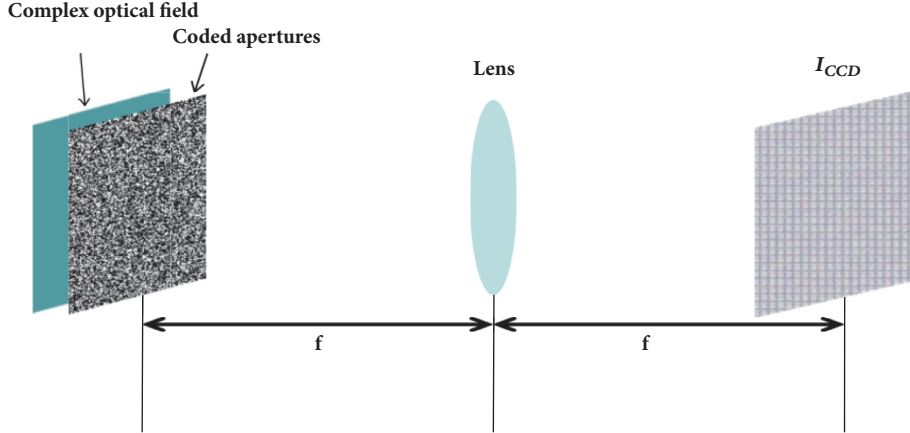


FIGURE 4: The optical setup of imaging process.

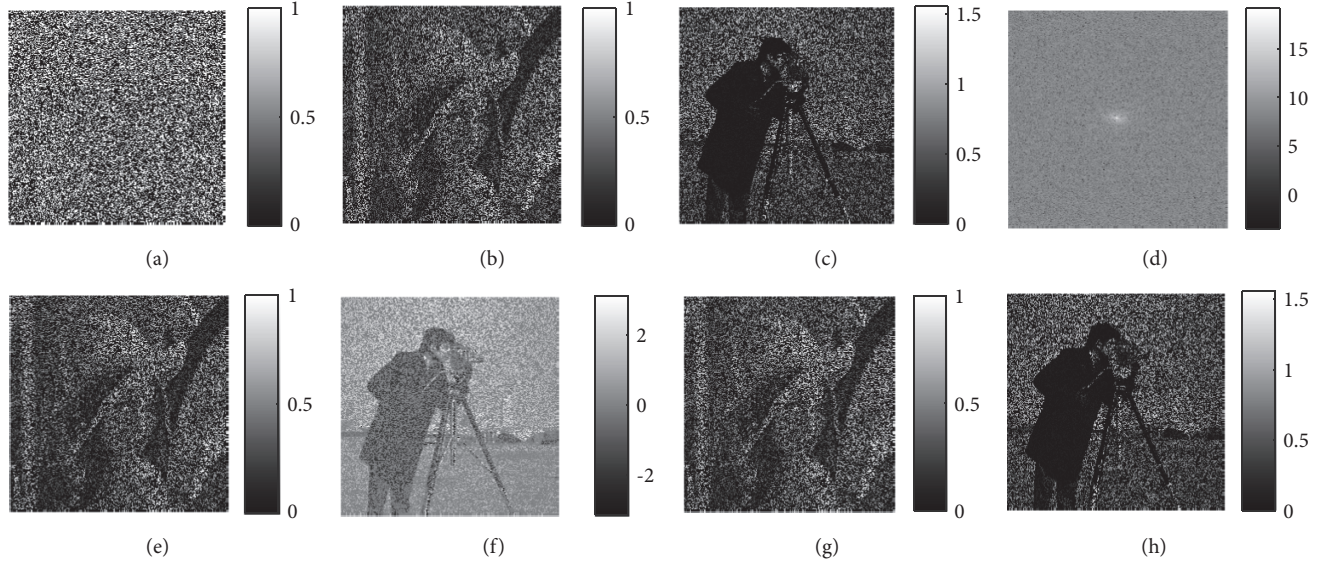


FIGURE 5: Comparison of SISR algorithm and TSPR algorithm. (a) A 0/1 randomly distributed coded aperture. (b) and (c) are the amplitude and phase of the complex optical field behind the coded aperture. (d) The intensity recorded in the Fourier domain. (e) and (f) are the amplitude and phase recovered using SISR algorithm. (g) and (h) are the amplitude and phase recovered using TSPR algorithm.

The main purpose of this paper is to recover the phase of the complex optical field  $u_M(x, y)$  from the recorded intensity measurement  $I_{CCD}$ .

#### 4. Numerical Experiments

In order to verify the effectiveness and superiority of our proposed method, three experiments are presented in this section. The first simulation experiment is the single reconstruction experiment. The second simulation experiment is to test the performance of TSPR algorithm under different coded apertures. The final simulation experiment is to compare the performance of the different phase retrieval algorithms.

**4.1. Experiment 1: Single Reconstruction Experiment.** The purpose of the experiment is to verify the feasibility of our proposed TSPR method. Two grayscale images ("Lena" and "Cameraman" with  $256 \times 256$  pixels) are chosen in the experiment. The two images are multiplied by the coded aperture ( $256 \times 256$  pixels) to obtain the amplitude and phase, respectively. Then the complex amplitude is synthesized by amplitude and phase. The coded aperture is 0/1 random distribution. The sampling rate in this experiment is 0.4, and the phase retrieval results are shown in Figure 5.

Figure 5(a) is the coded aperture with 0/1 randomly distributed, and the sampling rate is 0.4. Figures 5(b) and 5(c) are the amplitude and phase of the complex optical field behind

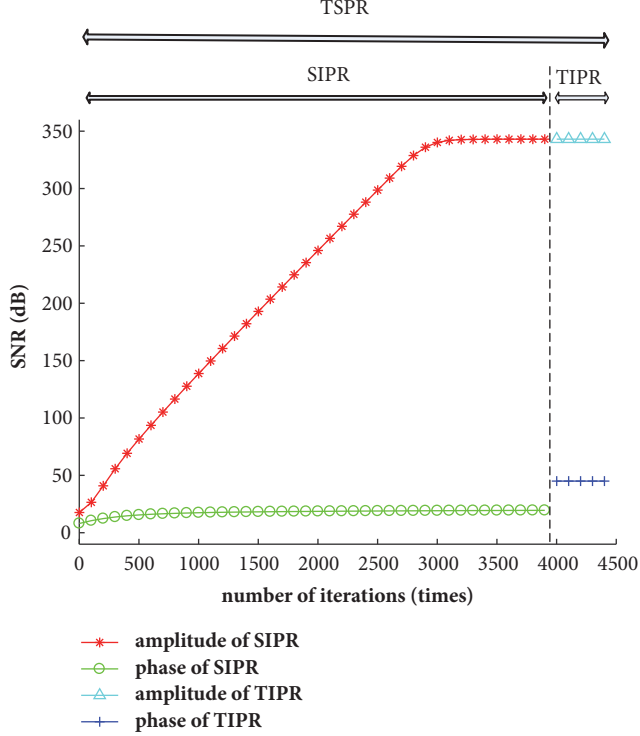


FIGURE 6: Amplitude and phase versus the number of iterations.

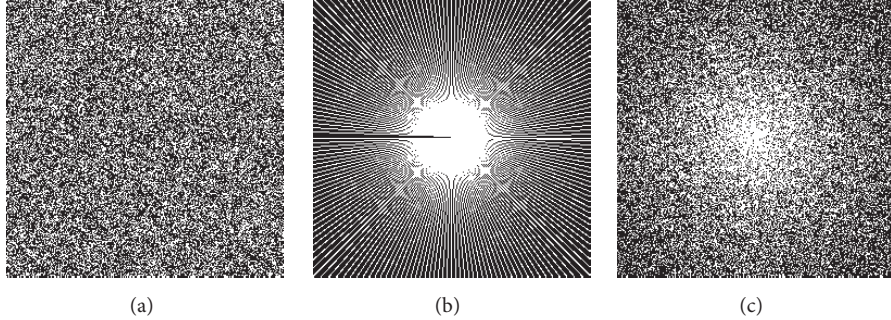


FIGURE 7: Three types of coded apertures with sampling rate of 0.3. (a) Uniform random sampling pattern. (b) Radial line sampling pattern. (c) Variable density sampling pattern.

the coded aperture to be retrieved. Figure 5(d) is the intensity recorded in the Fourier domain. Figures 5(e) and 5(f) are the amplitude and phase recovered using the SIPR algorithm, and the Signal-to-Noise Ratio (SNR) is 343.04 dB and 19.85 dB, respectively. Figures 5(g) and 5(h) are the amplitude and phase recovered using the TSPR algorithm, and their SNR is 343.04dB and 45.58dB, respectively. Comparing Figures 5(f)–5(h), it is easy to find that the quality of phase recovered is greatly improved by our TSPR method.

The trend of the amplitude and phase with the number of iterations in our TSPR method is shown in Figure 6. In the first step (i.e., SIPR) of TSPR, the amplitude can be well recovered, but the phase recovered is poor. As the number of iterations increases, the SNR of the phase recovered can only reach about 19dB. However, in the second step (i.e., TIPR) of

the TSPR, the SNR of the phase recovered increases as high as 45 dB. Compared with SIPR method, TSPR method can greatly improve the SNR of phase reconstructed.

**4.2. Experiment 2: Reconstruction Experiments under Different Coded Apertures.** The coded aperture in Experiment 1 is a uniform random sampling pattern. The purpose of Experiment 2 is to test the performance of the TSPR method under different coded apertures.

In Figure 7, three different types of the coded apertures are selected, such as Uniform Random (UR) sampling, Radial Line (RL) sampling, and Variable Density (VD) sampling. The sampling rate of the coded aperture is used as a variable parameter in the experiment, and the sampling rate is set from 0.1 to 0.7. Each set of experiments with the

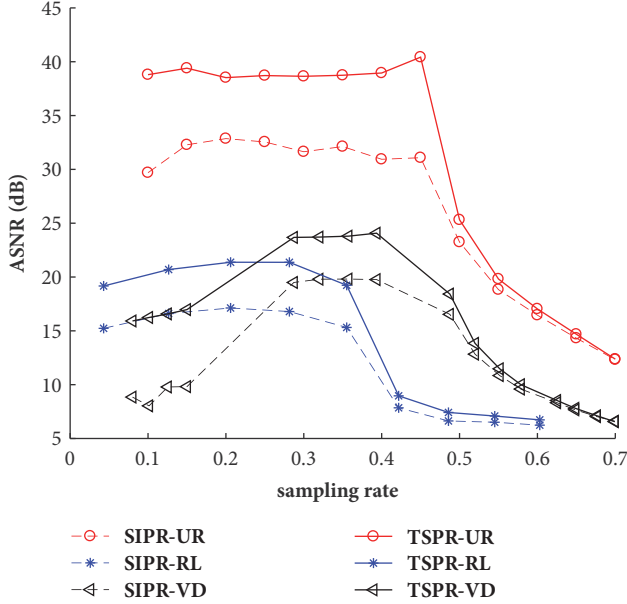


FIGURE 8: ASNR versus sampling rate.

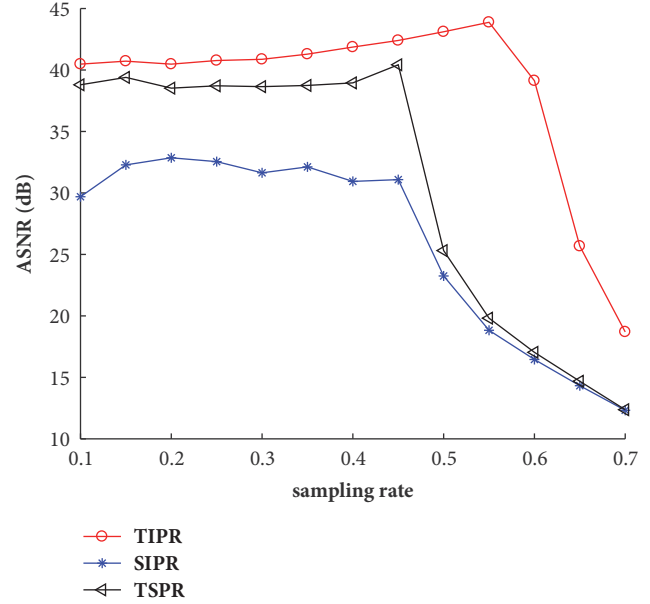


FIGURE 10: ASNR versus sampling rate.

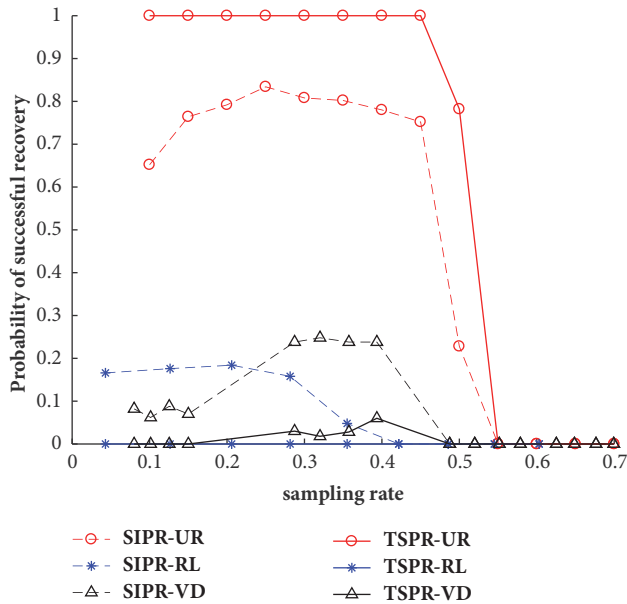


FIGURE 9: Probability of successful recovery versus sampling rate.

same parameters runs 500 times independently. Compute the recovered Average Signal-to-Noise Ratio (ASNR) and probability of successful recovery. The ASNR and probability of successful recovery versus sampling rate under different coded apertures are shown in Figures 8 and 9, respectively.

As shown in Figure 8, as the sampling rate increases, the TSPR algorithm achieves higher ASNR for phase recovered than the SIPR algorithm under three different coded apertures. In Figure 9, the best choice for coded aperture is uniform random sampling pattern, which achieve the optimal performance. The probability of successful recovery has also been significantly improved and has a good stability.

The reason is that the support set of the uniform random sampling pattern is relatively uniform distributed in the spatial domain, while the support set of the other two coded apertures is more concentrated to the center, so the phase cannot be retrieved well.

**4.3. Experiment 3: Reconstruction Experiment under Different Sampling Rates.** The purpose of Experiment 3 is to compare the performance of phase retrieval between our TSPR method and the other two algorithms (TIPR algorithm and SIPR algorithm) under different sampling rates. The coded aperture uses a uniform random sampling pattern with a sampling rate varies from 0.1 to 0.7 and the step size is 0.05. Under the same parameters, experiments runs 500 times independently. The ASNR and probability of successful recovery versus sampling rate for different algorithms are presented in Figures 10 and 11, respectively.

As shown in Figures 10 and 11, the TIPR method is the best, the TSPR method is the second, and the SIPR method is the worst. The reason is that TIPR method has the most known information, i.e., the two intensity measurements at two different planes. The difference between the TSPR method and the SIPR method is that the TSPR method draws on the idea of the TIPR method. Firstly, use the SIPR method to estimate the amplitude in the spatial domain, then use the TIPR method to recover the phase. In summary, the TSPR method is superior to the SIPR method.

## 5. Conclusion

This paper proposes an improved TSPR algorithm to solve the problem of poor quality and low success rate of SIPR method. TSPR algorithm is completed in two steps: firstly, SIPR algorithm is used to recover the amplitude in the spatial domain, then TIPR algorithm is used to recover the phase in

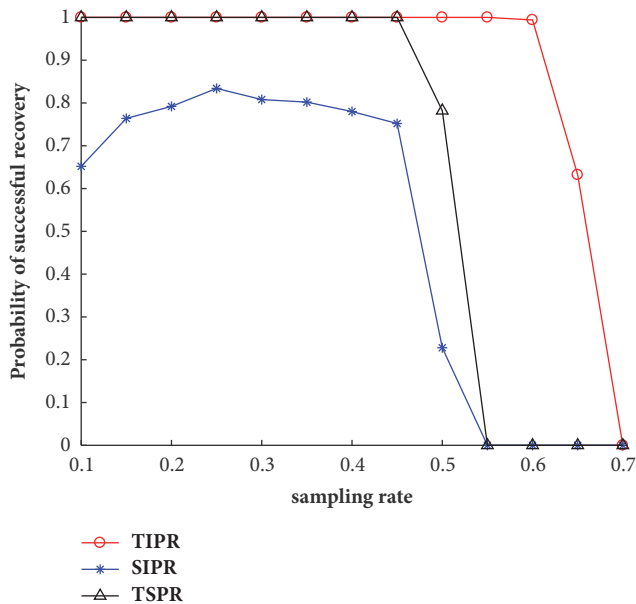


FIGURE 11: Probability of success versus sampling rate.

the spatial domain. Finally, the effectiveness and superiority of the TSPR method are verified. The experiment comparison results demonstrate that the proposed method can effectively improve the ASNR and probability of successful recovery under the same parameters. TSPR algorithm can recover the lost phase from known amplitude in the Fourier domain and support set in the spatial domain.

## Data Availability

The data in this paper has been signed into a commercial agreement, so it is confidential and cannot be made public.

## Conflicts of Interest

The authors declare that they have no conflicts of interest.

## Acknowledgments

This work was supported by the National Natural Science Foundation of China (Grant Numbers 61501001, 61605002, 61301296, and 61377006) and the Natural Science Foundation of Anhui Province (Grant Numbers 1508085MF121, 1608085QF161).

## References

- [1] Y. Shechtman, Y. C. Eldar, O. Cohen, H. N. Chapman, J. Miao, and M. Segev, "Phase retrieval with application to optical imaging: a contemporary overview," *IEEE Signal Processing Magazine*, vol. 32, no. 3, pp. 87–109, 2015.
- [2] R. W. Harrison, "Phase problem in crystallography," *Journal of the Optical Society of America A: Optics, Image Science & Vision*, vol. 10, no. 5, pp. 1046–1055, 1993.
- [3] R. P. Millane, "Phase retrieval in crystallography and optics," *Journal of the Optical Society of America A: Optics, Image Science & Vision*, vol. 7, no. 3, pp. 394–411, 1990.
- [4] J. A. Rodriguez, R. Xu, C.-C. Chen, Y. Zou, and J. Miao, "Oversampling smoothness: An effective algorithm for phase retrieval of noisy diffraction intensities," *Journal of Applied Crystallography*, vol. 46, no. 2, pp. 312–318, 2013.
- [5] A. Walther, "The question of phase retrieval in optics," *Journal of Modern Optics*, vol. 10, pp. 41–49, 1963.
- [6] M. C. Newton, "Compressed sensing for phase retrieval," *Physical Review E: Statistical, Nonlinear, and Soft Matter Physics*, vol. 85, no. 5, 2012.
- [7] J. Miao, P. Charalambous, J. Kirz, and D. Sayre, "Extending the methodology of X-ray crystallography to allow imaging of micrometre-sized non-crystalline specimens," *Nature*, vol. 400, no. 6742, pp. 342–344, 1999.
- [8] J. Hunt, J. Gollub, T. Driscoll et al., "Metamaterial microwave holographic imaging system," *Journal of the Optical Society of America A: Optics, Image Science & Vision*, vol. 31, no. 10, pp. 2109–2119, 2014.
- [9] C. Guo, S. Liu, and J. T. Sheridan, "Iterative phase retrieval algorithms. I: optimization," *Applied Optics*, vol. 54, no. 15, pp. 4698–4708, 2015.
- [10] C. Fienup and J. Dainty, "Phase retrieval and image reconstruction for astronomy," *Image Recovery: Theory and Application*, vol. 231, p. 275, 1987.
- [11] J. Miao, T. Ishikawa, Q. Shen, and T. Earnest, "Extending X-ray crystallography to allow the imaging of noncrystalline materials, cells, and single protein complexes," *Annual Review of Physical Chemistry*, vol. 59, pp. 387–410, 2008.
- [12] H. M. L. Faulkner and J. M. Rodenburg, "Movable aperture lensless transmission microscopy: A novel phase retrieval algorithm," *Physical Review Letters*, vol. 93, no. 2, Article ID 023903, 2004.
- [13] M. Dierolf, A. Menzel, P. Thibault et al., "Ptychographic X-ray computed tomography at the nanoscale," *Nature*, vol. 467, no. 7314, pp. 436–439, 2010.
- [14] G. Situ, J. P. Ryle, U. Gopinathan, and J. T. Sheridan, "Generalized in-line digital holographic technique based on intensity measurements at two different planes," *Applied Optics*, vol. 47, no. 5, pp. 711–717, 2008.
- [15] D. Deng, W. Qu, W. He, Y. Wu, X. Liu, and X. Peng, "Phase retrieval for digital holographic microscopy with defocused holograms," *IEEE Photonics Journal*, vol. 10, no. 1, 2018.
- [16] R. W. Gerchberg and W. O. Saxton, "A practical algorithm for the determination of the phase from image and diffraction plane pictures," *Optik - International Journal for Light and Electron Optics*, vol. 35, no. 2, pp. 237–250, 1972.
- [17] J. R. Fienup, "Reconstruction of an object from the modulus of its Fourier transform," *Optics Express*, vol. 3, no. 1, pp. 27–29, 1978.
- [18] J. R. Fienup, "Phase retrieval algorithms: a comparison," *Applied Optics*, vol. 21, no. 15, pp. 2758–2769, 1982.
- [19] G. Yang, B. Gu, and B. Dong, "Theory of the amplitude-phase retrieval in any linear transform system and its applications," *International Journal of Modern Physics B*, vol. 07, no. 18, pp. 3153–3224, 1993.
- [20] J. R. Fienup, "Phase retrieval algorithms: A personal tour," *Applied Optics*, vol. 52, no. 1, pp. 45–56, 2013.